Alberto Bollero Real

Isotropic Nanocrystalline (Nd,Pr)(Fe,Co)B Permanent Magnets

Isotropic Nanocrystalline (Nd,Pr)(Fe,Co)B Permanent Magnets

DISSERTATION

Zur Erlangung des akademischen Grades

Doctor rerum naturalium

(Dr. rer. nat.)

vorgelegt

der Fakultät Mathematik und Naturwissenschaften

der Technischen Universität Dresden

von

Dipl.-Phys. Alberto Bollero Real

geboren am 11.11.1973 in Madrid

Die vorliegende Dissertationsschrift wurde am
Institut für Metallische Werkstoffe des IFW Dresden (http://www.ifw-dresden.de)
unter der wissenschaftlichen Betreuungvon Prof. Dr.rer.nat. habil. L. Schultz angefertigt.

Gutachter: Prof. Dr. L. Schultz (IFW Dresden)
Prof. Dr. C. Laubschat (TU Dresden)
Prof. Dr. I.R. Harris (University of Birmingham)

Eingereicht am: 22.04.2003
Tag der Verteidigung: 17.11.2003

Synopsis

Nanocrystalline permanent magnets present unusual magnetic properties because of surface/interface effects different from those of bulk or microcrystalline materials. This is mainly due to the grain size and the presence or absence of intergranular phases. The first part of this work presents results of a systematic investigation of the relationship between microstructure and magnetic properties in isotropic nanocrystalline (Nd,Pr)(Fe,Co)B permanent magnets. Highly coercive (Nd,Pr)FeB-type magnets have been produced using high energy ball milling and melt-spinning techniques. The influence of small amounts of additives, Dy and Zr, and the substitution of Nd by Pr on the microstructural and magnetic properties are shown. An assessment of the hot deformation behaviour for these materials has been carried out. The lowest deformation stresses necessary for texturing were obtained for the as-milled Pr-containing alloys.

Intensive milling of an alloy with starting composition $Pr_9Nd_3Dy_1Fe_{72}Co_8B_{6.9}Zr_{0.1}$ yielded, after subsequent annealing treatment, nearly single-phase magnet powders with a maximum energy product $(BH)_{max}$ ~ 140 kJm^{-3}. Co is shown to have a beneficial effect on the intrinsic magnetic properties but also on the microstructure, with a mean grain size of 20 nm. Furthermore, intensive milling has shown to be a very versatile technique to produce high-performance nanocomposite magnets by blending this latter alloy with different fractions of soft magnetic α-Fe. Addition of 25wt.% α-Fe led to an optimum combination of magnetic properties with a very high $(BH)_{max}$ value of 178 kJm^{-3} due to an effective exchange-coupling between the hard and the soft magnetic phases.

Reversibility measurements of the demagnetisation curves give important information on the magnetisation processes in exchange-coupled magnets. The intergrain interactions between the crystallites of the nanocomposite structure have been analysed in the second part of this study.

Demagnetisation recoil loops of the nanocomposite magnets have shown relatively open minor loops due to the exchange-spring mechanism. Information about the intergrain interactions during demagnetisation can be obtained by plotting the deviation of the demagnetising remanence from the Wohlfarth-model ("δJ-plot"). Exchange-coupling phenomena have been studied by analysing the evolution of the corresponding δJ values

when varying (i) the α-Fe content, (ii) the annealing temperature, i.e. the grain size and (iii) the measurement temperature. Measurements of the reversible and irreversible changes in polarisation have provided valuable insight into the mechanisms responsible for exchange-coupling in these nanocomposite permanent magnets. Low temperature measurements did not reveal any sign of spin reorientation for these Pr-based nanocomposite magnets. The temperature dependence of the magnetic properties has been studied in the temperature range from -200ºC to 200ºC.

The work concludes showing the possibility of using a mechanically activated gas-solid reaction to obtain an effective grain refined microstructure starting from stoichiometric $Nd_2(Fe_{1-x}Co_x)_{14}B$ alloys (x = 0, 0.25, 0.5, 0.75 and 1). These compounds have been milled under enhanced hydrogen pressure and temperature leading to their disproportionation into $NdH_{2+\delta}$ and bcc-(Fe,Co) ($0 \leq x \leq 0.75$) or fcc-Co (x = 1). This reactive milling leads to the disproportionation of the thermodynamically very stable $Nd_2Co_{14}B$ alloy. This reaction is not possible via the conventional hydrogenation disproportionation desorption and recombination (HDDR) process. Grain sizes of recombined $Nd_2(Fe,Co)_{14}B$ materials were found to be 40-50 nm – approximately an order of magnitude smaller than those of conventional-HDDR processed alloys. The recombined $Nd_2Co_{14}B$ alloy shows on average slightly smaller grain sizes than the $Nd_2Fe_{14}B$ compound. A more effective exchange-coupling leading to enhanced remanences, possibly due to the slightly smaller grain size, has been observed for $Nd_2Co_{14}B$ powders recombined at 600-700 °C.

Zusammenfassung

Nanokristalline Permanentmagnete zeigen ungewöhnliche magnetische Eigenschaften aufgrund von Oberflächen- und Grenzflächeneffekten, die verschieden von denen massiver oder mikrokristalliner Materialien sind. Dies liegt hauptsächlich an der Korngröße und der An- bzw. Abwesenheit intergranularer Phasen. Der erste Teil dieser Arbeit zeigt Ergebnisse einer systematischen Untersuchung der Beziehung zwischen Mikrostruktur und magnetischen Eigenschaften von isotropen nanokristallinen (Nd,Pr)(Fe,Co)B-Permanentmagneten. Hochkoerzitive Magnete vom Typ (Nd,Pr)FeB wurden durch hochenergetisches Mahlen in der Kugelmühle oder Rascherstarrung hergestellt. Der Einfluss geringer Mengen von Zusätzen wie Dy und Zr und die Substitution von Nd durch Pr auf die magnetischen Eigenschaften wird dargestellt. Weiterhin wurde eine Einschätzung des Warmumformverhaltens dieser Materialien durchgeführt. Die niedrigsten Umformspannungen für eine optimale Texturierung wurden für die kugelgemahlenen Pulver auf Pr-Basis gefunden.

Hochenergetisches Kugelmahlen einer Legierung mit der Anfangszusammensetzung $Pr_9Nd_3Dy_1Fe_{72}Co_8B_{6.9}Zr_{0.1}$ führte, nach anschließender Glühbehandlung, zu fast einphasigem Magnetpulver mit einem maximalen Energieprodukt von $(BH)_{max} \sim 140\ kJm^{-3}$. Es wird gezeigt, dass Co einen positiven Einfluss auf die wesentlichen magnetischen Eigenschaften hat, was u.a. auf die Bildung einer verfeinerten Mikrostruktur mit einer mittleren Korngröße von 20 nm zurückzuführen ist. Das hochenergetische Kugelmahlen wurde zu einer sehr vielseitigen Technik zur Herstellung hochleistungsfähiger Nanokompositmagnete weiterentwickelt. Das Zulegieren unterschiedlicher Anteile von weichmagnetischem α-Fe ist damit sehr effektiv möglich. Der Zusatz von 25 Gew.-% α-Fe führt zu einer optimalen Kombination der magnetischen Eigenschaften und einem sehr hohen $(BH)_{max}$-Wert von 178 kJm^{-3}. Dies wird auf eine sehr effektive Austauschkopplung zwischen den hart- und weichmagnetischen Phasen zurückgeführt.

Die Austauschkopplung zwischen den Kristalliten der Nanokompositstruktur wird im zweiten Teil dieser Arbeit analysiert. Die Reversibilität der Entmagnetisierungskurven

liefert wichtige Informationen über die Magnetisierungsprozesse in austauschgekoppelten Magneten. Speziell sind offene innere Hystereseschleifen ein Indiz für eine effektive Kopplung in Nanokompositmagneten. Die Natur der intergranularen Wechselwirkungen kann durch die Wohlfarth´sche Remanenzanalyse („δJ-plot“) beschrieben werden. Im speziellen wurden δJ-Diagramme für verschiedene (i) α-Fe Gehalte, (ii) Korngrößen (erzielt durch Variation der Glühbehandlung) und (iii) Austauschlängen (durch Variation der Messtemperatur) erstellt. Messungen der reversiblen und irreversiblen Änderungen der Polarisation haben wertvolle Einsicht in die verantwortlichen Mechanismen für die Austauschkopplung in diesen Nanokompositmagneten geliefert. Weiterhin wurde die Temperaturabhängigkeit der magnetischen Eigenschaften im Temperaturbereich von –200°C bis 200°C untersucht. Es konnte gezeigt werden, dass in den Nanokompositmagneten auf Pr-Basis keine Spinumorientierung auftritt.

Abschließend zeigt die Arbeit die Möglichkeit der Nutzung einer mechanisch aktivierten Gas-Festkörper-Reaktion auf, mit der eine sehr feinkörnige Mikrostruktur erhalten wird. Die Untersuchungen wurden mit stöchiometrischen $Nd_2(Fe_{1-x}Co_x)_{14}B$-Legierungen begonnen (x = 0, 0.25, 0.5, 0.75 und 1). Die Verbindungen wurden unter höheren Wasserstoffdrücken und Temperaturen gemahlen, wodurch sie zu $NdH_{2+\delta}$ und krz-(Fe,Co) ($0 \leq x \leq 0.75$) oder kfz-Co (x = 1) entmischt wurden. Dieses reaktive Mahlen führt damit zu einer Entmischung der thermodynamisch sehr stabilen $Nd_2Co_{14}B$-Legierung. Die Reaktion ist mit einem konventionellen HDDR-Prozess (Hydrogenation Disproportionation Desorption and Recombination) nicht möglich. Die Korngrößen des rekombinierten $Nd_2(Co,Fe)_{14}B$-Materials liegen im Bereich von 40-50 nm und sind etwa um eine Größenordnung kleiner als die mit dem konventionellen HDDR-Prozess erhaltenen. Für die rekombinierte $Nd_2Co_{14}B$-Legierung werden im Durchschnitt etwas kleinere Korngrößen als für die $Nd_2Fe_{14}B$-Legierung beobachtet. Eine erhöhte Remanenz, die möglicherweise durch die effektivere Austauschkopplung der etwas kleineren Körner entsteht, ist für die $Nd_2Co_{14}B$-Pulver beobachtet worden, die bei 600-700 °C rekombiniert worden sind.

CONTENTS

Synopsis / Zusammenfassung i

Notation and quantities vii

1. Introduction 1

2. Magnetism of R-T intermetallic compounds 4
2.1. Hysteresis loop 4
2.2. Magnetic properties 6
2.2.1. Magnetic moments 6
2.2.2. Exchange interactions 8
2.2.3. Anisotropy 10
2.2.4. Magnetic domains 11
2.2.5. Origin of coercivity 13

3. The exchange-coupling mechanism 16
3.1. Models 17
3.1.1. Single-phase nanocrystalline magnets 17
3.1.2. Two-phase nanocomposite magnets 19
3.2. Wohlfarth's relation and Henkel plot 20
3.3. Magnetisation reversal processes in nanocomposite magnets 22
3.3.1. Recoil loops and "exchange-spring" magnet behaviour 22
3.3.2. Intergrain interactions: δJ-plot 23
3.3.3. Nucleation field 23
3.4. Development of exchange-coupled nanocrystalline magnets 24

4. Systems under investigation 28
4.1. NdFeB 28
4.2. NdCoB 30
4.3. PrFeB 31

5. Experimental details 34
5.1. Nanocrystalline powder processing 34
5.1.1. Melt-spinning 34
5.1.2. High energy ball milling 35
5.1.3. Reactive milling in hydrogen 36
5.1.4. Hot deformation 38
5.2. Structural characterisation 38
5.2.1. Differential scanning calorimetry 38
5.2.2. X-ray diffraction 39
5.2.3. Electron microscopy 41
5.3. Characterisation of magnetic properties 41
5.3.1. Vibrating sample magnetometer 41
5.3.2. Curie temperature measurements 42

6. Decoupled magnets: (Nd,Pr)-based magnets 43
6.1. Thermal characterisation 43
6.1.1. Starting alloys 43

6.1.2. Milled and melt-spun alloys 44
6.2. Microstructural characterisation 45
6.3. Characterisation of magnetic properties 47
6.3.1. Evolution of magnetic properties of milled alloys in dependence on the annealing temperature 47
6.3.2. Influence of additives and Pr-content on coercivity in alloys processed by milling and melt-spinning 50
6.4. Hot workability 53
6.5. Summary 55

7. Nanocomposite magnets: PrNdDyFeCoBZr + x wt.% α-Fe (x = 5 - 35) 57
7.1. Characterisation of the base alloy: $Pr_{11.25}Nd_{3.75}Dy_{1.0}Fe_{76.0}B_{8.1}Zr_{0.1}$ 57
7.1.1. DSC and thermomagnetic analysis of starting and milled material 57
7.1.2. Microstructural characterisation 59
7.1.3. Characterisation of magnetic properties 60
7.2. Characterisation of the base alloy blended with α-Fe: PrNdDyFeCoBZr + x wt.% α-Fe 61
7.2.1. Compositional analysis 61
7.2.2. Magnetic behaviour 62
(i) Hysteresis loop 62
(ii) Evolution of magnetic properties vs. α-Fe fraction 63
(iii) Thermomagnetic results 65
7.3. Summary 66

8. Initial magnetisation and reversal magnetisation processes in nanocrystalline magnets 67
8.1. Initial magnetisation processes 68
8.2. Recoil loops at room temperature 72
8.3. Analysis of exchange-coupling using δJ-plots 73
8.3.1. The effect of the α-Fe content 73
8.3.2. The effect of the annealing temperature (grain size) 80
8.3.3. The effect of the measurement temperature 87
8.4. Summary 93

9. Reactive milling in hydrogen 95
9.1. Reactive milling of a $Pr_{14.7}Fe_{77.3}B_{8.0}$ alloy 97
9.1.1. Structural changes throughout the different processing stages 97
9.1.2. Evolution of magnetic properties on desorption 99
9.2. Reactive milling of $Nd_2(Fe,Co)_{14}B$ alloys 100
9.2.1. Microstructural characterisation of starting alloys 100
9.2.2. Effect of Co-content on density and Curie temperature 103
9.2.3. Disproportionation by reactive milling 104
9.2.4. Desorption and recombination 105
9.2.5. Average grain size 107
9.2.6. Remanence enhancement of recombined Nd(Fe,Co)B powders 108
9.3. Summary 110

10. Conclusions and future work 112

References 119

Notation and quantities [units]

A	exchange stiffness [Jm^{-1}]
at.%	atomic per cent
α'	relative remanence
$(BH)_{max}$	maximum energy product [kJm^{-3}]
χ_{irr}	irreversible susceptibility [T^{-1}]
d	grain size
d_c	critical single-domain particle size [nm]
DSC	Differential Scanning Calorimetry
DU	die-upsetting
δ_w	domain wall width [nm]
E_a	anisotropy energy [Jm^{-3}]
EDX	Energy Dispersive X-ray Analysis
ε	degree of deformation after die upsetting
HDDR	Hydrogenation-Disproportionation-Desorption-Recombination
HRTEM	High resolution transmission electron microscopy
IM	Intensive milling
J	polarisation [T]
J_r	remanence [T]
$J_r^{(m/d)}$	remanent polarisation during magnetisation (m) or demagnetisation (d) [T]
J_{rev}	reversible change in polarisation [T]
J_s	saturation polarisation [T]
K	anisotropy constant [Jm^{-3}]
l_{ex}	exchange length [nm]
m	magnetic moment [JT^{-1}]
M	magnetisation [Am^{-1}]
MS	Melt-spinning
μ_0	permeability of vacuum [$\mu_0 = 4\pi \times 10^{-7}$ Tm/A]
$\mu_0 H_{appl}$	applied field [T]
$\mu_0 H_c$	coercivity [T]

$\mu_0 H_{no}$	nucleation field [T]
$\mu_0 H_r$	remanent coercivity [T]
R	rare-earth element
SEM	Scanning Electron Microscopy
σ	deformation stress [MPa]
T	transition-metal element
T_C	Curie temperature [^{o}C]
TEM	Transmission Electron Microscopy
TPA	Temperature Pressure Analysis
T_x	onset of crystallisation temperature [^{o}C]
VSM	Vibrating Sample Magnetometer
wt.%	weight per cent
XRD	X-ray diffraction

1 Introduction

A permanent magnet can be defined as a ferromagnetic material which is prepared in a metastable state where it retains some net magnetisation. In this way, a magnet can be considered as an energy-storage device which provides a magnetic field in a particular volume of space. From 1983, when high-performance $Nd_2Fe_{14}B$-type magnets were successfully prepared in Japan and the USA, the production of rare-earth (R) magnets, and $Nd_2Fe_{14}B$-type magnets in particular, has seen a spectacular growth. The wide range of applications for these magnets, from everyday appliances like loudspeakers to the high-tech applications of the aerospace industry, and new areas of application like magnetic resonance imaging (MRI), have fueled this increase in production. One promising area is the use of permanent magnets in automotive applications, particularly in control systems. The search for optimised compositions and improved processing techniques, which has lead to improved properties and low-cost NdFeB-type magnets, has been the challenge facing researchers over recent years.

An effective permanent magnet requires as a starting point adequate intrinsic magnetic properties, but this is not enough to guarantee a high-quality magnet. The interplay between the intrinsic properties and the microstructure will determine the magnetic behaviour of permanent magnets. Depending on the R-content three different prototypes of magnets can be defined (see Fig. 1.1): (a) R-rich magnets constituted by decoupled grains separated by a thin paramagnetic layer giving rise to high coercivities (type I); (b) magnets based on $R_2T_{14}B$ stoichiometric composition where the grains are exchange-coupled resulting in high remanence values J_r (type II) and (c) nanocomposite magnets constituted by two different magnetic phases, hard and soft, mutually exchange-coupled (type III). The latter type has attracted much attention in recent years due to the potentially very high $(BH)_{max}$ value despite of a relatively low content of hard magnetic phase based on the magnetically single-phase behaviour of these two-phase materials and a remanence enhancement due to the higher saturation polarisation J_s of the soft magnetic phase and the exchange-coupling effect between the hard and the soft magnetic grains. This effect results in larger remanences than those predicted for systems of isotropically oriented, magnetically uniaxial, non-interacting single-domain particles where the limit $J_r /$

J_s = 0.5 can not be exceeded. A phenomenological description of the exchange-coupling effect and a short overview of the technical development of exchange-coupled nanocomposite magnets are presented in Chapter 3.

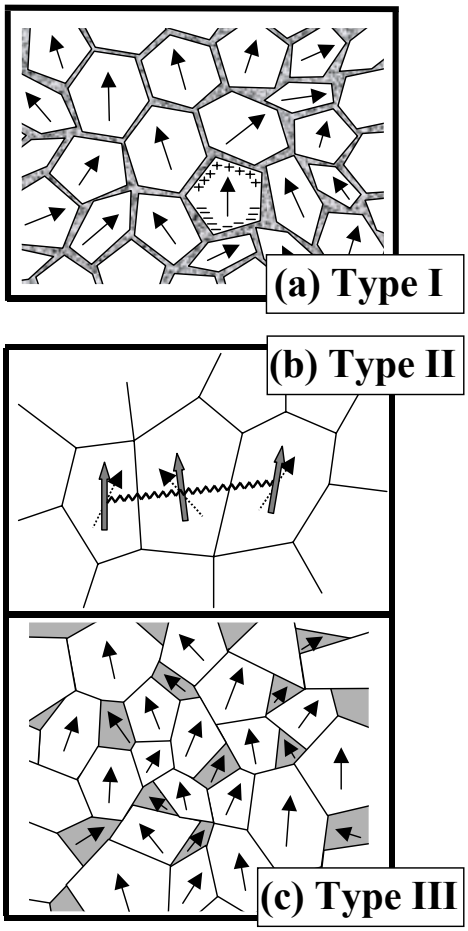

Fig. 1.1: Prototypes of rare earth permanent magnets with idealised microstructures: (a) Type I: decoupled magnet (shaded area: thin paramagnetic layer); (b) Type II: exchange-coupled single-phase magnet; (c) Type III: exchange-coupled nanocomposite magnet (white regions: hard magnetic grains; dark regions: soft magnetic phase). Arrows indicate the corresponding local easy axis for every grain. The micromagnetic structure originated from the parallel alignment of the magnetic moments in the vicinity of the grain boundaries (exchange-coupling between the grains) is illustrated in (b).

At present $Nd_2Fe_{14}B$-based magnets constitute the most suitable choice for applications at room temperature where highest energy density values are required whereas the more expensive SmCo-based magnets are the material of choice for elevated temperature applications. Chapter 4 begins by describing the main characteristics of the

$Nd_2Fe_{14}B$ system and, afterwards, two similar systems are considered: $Nd_2Co_{14}B$ and $Pr_2Fe_{14}B$. The main limitation of $Nd_2Fe_{14}B$ is its relatively low Curie temperature which disables high temperature applications because of the rapid decrease of its hard magnetic properties. Substitution of Co for Fe significantly enhances the Curie temperature. At low temperatures, the $Nd_2Fe_{14}B$ phase exhibits another disadvantage: a spin reorientation takes place at temperatures lower than 135 K. Contrary to this $Pr_2Fe_{14}B$ is a very good candidate for low temperature applications since no spin reorientation takes place. Furthermore, the final magnet performance at room temperature for the $Pr_2Fe_{14}B$ system is comparable to that of NdFeB-based magnets.

Melt-spinning, mechanical alloying and the hydrogenation-disproportionation-desorption-recombination (HDDR) process are three different methods of processing nanocrystalline NdFeB alloys (Chapter 5). The two former methods are used in a first stage of this work to produce highly coercive powders (Chapters 6). Second, it is shown that intensive milling is a very versatile technique to obtain high-quality isotropic nanocomposite powders by blending a Pr-based starting alloy with elementary powders of a soft magnetic α-Fe phase (Chapter 7). The evolution of the magnetic properties in dependence on the different Fe fractions is studied, and the achieved energy density and Curie temperature of the optimally processed composition make it an excellent candidate for bonded magnets with the additional advantage of a reduced R-content, i.e. lower cost and improved corrosion resistance. An analysis of magnetisation reversal in these Pr-based nanocomposite magnets has been carried out in order to obtain a better understanding of the intergranular interactions present. These results are compared with those of decoupled magnets (Chapter 8).

The last part of this work (Chapter 9) shows the possibility of producing nanocrystalline isotropic magnets of $Nd_2Fe_{14}B$ and $Nd_2Co_{14}B$ with an enhanced remanence by a mechanically activated gas-solid reaction. This is achieved by using the reactive milling technique which consists of ball milling in enhanced hydrogen pressures and temperatures. The main problem is the high thermodynamical stability of the $Nd_2Co_{14}B$ parent compound. In the present work the reactive milling technique has been applied to $Nd_2Fe_{14}B$ and $Nd_2Co_{14}B$ alloys.

2 Magnetism of R-T intermetallic compounds

A brief introduction of some important concepts of magnetism is given in the following with the focus on rare-earth (R) transition-metal (T) intermetallic compounds. For more details, the books of Chikazumi (1997) [1] and Cullity (1972) [2] are very useful for a general introduction to magnetism, and the book edited by Coey (1996) [3] presents a complete overview on rare earth-iron permanent magnets. Herbst and Croat (1991) [4] describe the properties of hard magnets with particular reference to NdFeB magnets. A general review on R-T compounds and processing routes is given by Gutfleisch [5].

2.1 Hysteresis loop

The response of a ferromagnetic material to a magnetic field H is represented by its hysteresis loop. This loop is broad for a good permanent magnet which has to resist demagnetisation by external fields and the field created by its own magnetisation. Ideal and typical hysteresis loops for permanent magnets are shown in Fig. 2.1. Significant parameters associated with the loop are the remanence J_r (value of the polarisation when $H = 0$), and the coercivity H_c (reverse field required to reduce the net polarisation to zero – that is, to demagnetise the material). H_c has to be distinguished from the coercivity ${}_BH_c$ (value of field at which $B = 0$). The J_r value is limited by the saturation polarisation, J_s , which can be defined as the maximum polarisation value when the material is magnetised by applying an external magnetic field.

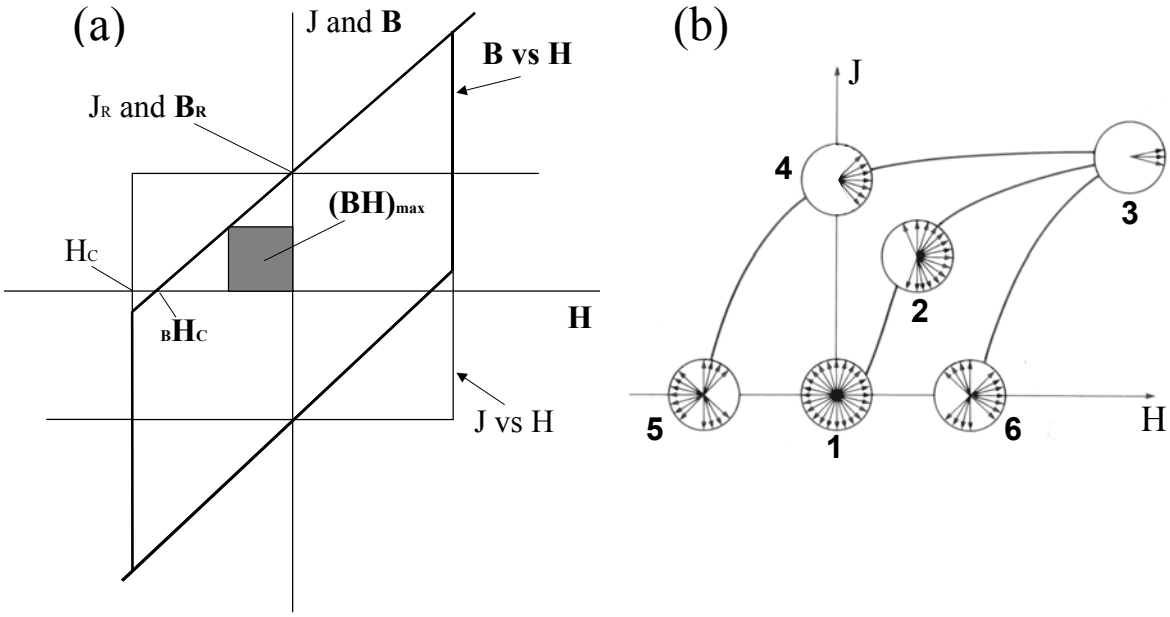

Fig. 2.1: (a) Hysteresis loop for an ideal permanent magnet: B (induction) vs. H; J (polarisation) vs. H. (b) 1st and 2nd quadrants of a typical hysteresis loop, J vs. H, for a permanent magnet. Numbered circles are schematic representations of magnetic states: 1. isotropic distribution of magnetic moments in the thermally demagnetised state; 2. intermediate state during magnetising; 3. nearly saturated state; 4. remanent polarisation after removing the applied field; 5. and 6. null net polarisation (adapted from Chikazumi [1]. It must be noted that the magnetic state numbered with 3 should be situated at a higher position to be consistent with the representation).

The so called maximum energy product $(BH)_{max}$ provides a measure of the magnetic energy density that can be stored in the considered material. It is the maximum value of $B \times H$ on the second quadrant of the B-H loop (shaded area in Fig. 2.1a) and it can be considered the most important figure of merit to describe the quality of a permanent magnet.

Ideal permanent magnets exhibit a magnetisation curve which is a square loop where the remanence has the largest possible value, $J_r = J_s$, and the magnetisation remains independent of reverse field up to H_c. If $\mu_0 H_c$ is larger than $J_r/2$ the maximum energy product would be $J_s^2/4\mu_0$ (the magnetic induction is $B=\mu_0 H+J=\mu_0(H+M)$, with $\mu_0 = 4\pi \times 10^{-7}$ Tm/A, thus giving B and the polarisation J in T, and the magnetic field H and the magnetisation M in A/m, but $\mu_0 H$ also in T). In practice J_r is lower than J_s because of incomplete particle alignment, the presence of magnetic domains, the density being less than the ideal density of the main magnetic phase and secondary phases.

2.2 Magnetic properties

Generally, the magnetic properties of a magnetic material can be grouped as follows:

a) Intrinsic magnetic properties: saturation polarisation, Curie temperature and anisotropy constants as well as quantities derived from them as the anisotropy field. They are determined by magnetic moments and interactions on the atomic scale.

b) Extrinsic magnetic properties: remanence, coercivity and energy product. These are related to the hysteresis loop arising from the actual microstructure.

The electronic structure of the material has to be taken into account to understand these properties and their evolution. In the case of magnetism resulting from localised electrons the atomic magnetic moments and their mutual exchange interaction and their interaction with the atomic lattice must be considered.

2.2.1 Magnetic moments

The field created by a permanent magnet is associated with the motions and interactions of its electrons. These present two different contributions, orbital momentum and spin momentum, and each has a magnetic moment associated with it. Nuclear magnetism is negligible by comparison. The maximum magnetic moment, m, of a single atom in a particular direction is given by

$$m = g\mathcal{J}\mu_B \tag{2.1}$$

where g is the Landé factor (ratio of the magnetic moment to the angular moment), μ_B is the Bohr magneton ($1\mu_B = 9.274\times10^{-24}$ JT^{-1}) and $\mathcal{J}$ is the total angular momentum of the atom. $\mathcal{J}$ is defined as $\mathcal{J} = L \pm S$ where L is the orbital angular momentum and S is the spin angular momentum. The sign is determined by Hund's rules.

If the elementary atomic contributions are summed up in a volume that is large on the atomic scale, a local magnetisation vector can be defined in a mesoscopic description which is not uniform throughout the macroscopic sample. In equilibrium, a ferromagnetic sample would normally not have a net magnetisation because the magnetostatic energy will favour magnetic domains. However, if it is possible to put it into a metastable state where it retains some net magnetisation approximately independent of external magnetic fields, we will have a permanent magnet.

(i) The rare-earth (R) series

The rare-earth series presents an incomplete filling of the 4f shell. The number of electrons in the inner 4f shell varies from 0 to 14 through the series La (atomic number in the periodic table: $Z = 57$) to Lu ($Z = 71$). The total magnetic moment of an R-atom has both orbital and spin components. However the 4f shell is not the outermost shell of the atom. Figure 2.2 illustrates the position of the 4f shell for Nd ($Z = 60$) where the 3 electrons with unpaired spin are localised. The R-R exchange-coupling between two R atoms in a solid is indirect because the direct overlap between the 4f shells of adjacent rare-earth atoms is negligible. The resulting weak magnetic interaction with the 4f electrons of neighbouring atoms, results in low Curie temperatures of the ferromagnetic rare-earth metals; in fact, all of them have a T_C below room temperature (only Gd has a Curie temperature as high as ambient temperature, $T_C = 20°C$).

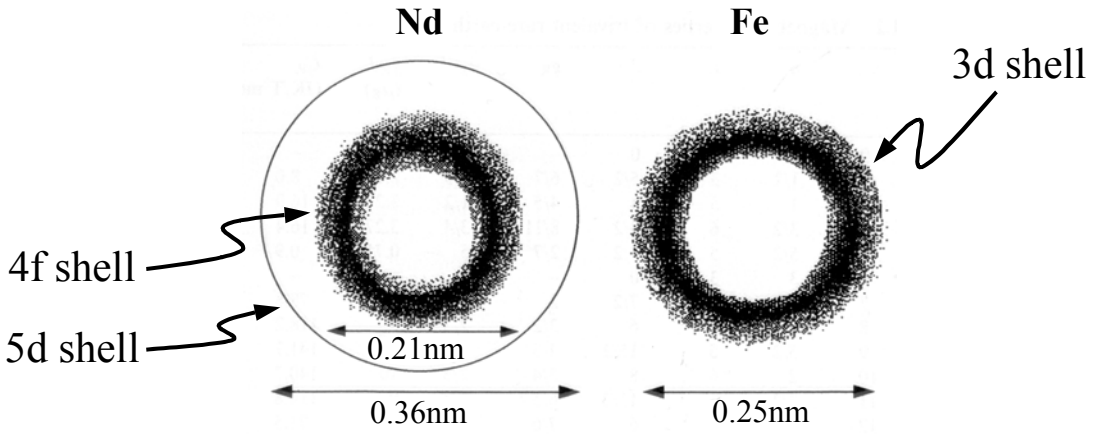

Fig. 2.2: Positions of the unpaired electron shells in Nd and Fe atoms (from Coey [3]).

(ii) The transition-metal (T) elements: Fe, Co and Ni

There are three ferromagnetic transition elements: Fe, Co and Ni. The 3d electrons of these atoms are localised in the outer shell (see Fig. 2.2). Hence in solids the 3d electrons are considerably less localized than the 4f electrons of the rare earths. Therefore the orbital momentum of T atoms or ions is nearly completely removed ("quenched") by the interaction in the solid which, of course, is not rotationally invariant and does not allow the orbital momentum to be a good quantum number. Usually the (spin) magnetism of the T elements in metals and intermetallic compounds is described by delocalised electrons. Fe is

classified as a *weak* ferromagnet (despite its relatively large moment) because the majority-spin 3d↑ levels are not completely occupied, whereas the other two are *strong* ferromagnets because there are no 3d↑ holes. Fe is the 3d element with largest spin moment per atom (2.22 μ_B) followed by Co (1.72 μ_B). In a description of 3d magnetism by localised moments the strong overlap of the 3d wave functions results in a strong direct exchange interaction between these moments and, consequently, they exhibit high Curie temperatures: T_C (Fe) = 770°C, T_C (Co) = 1127°C and T_C (Ni) = 362°C. The 3d spin moment is very sensitive to the chemical environment. It can change substantially in metallic alloys; for example, the moment of Fe, which is approximately dense-packed in the rare-earth intermetallics, is especially sensitive to interatomic spacing and lattice volume in such compounds. However, if an R element is alloyed with another element, there will be a modification of the magnetic anisotropy, but usually the 4f atoms will retain their magnetic moment.

(iii) Rare-earth / transition-metal intermetallics

By combining rare-earth elements with one of the ferromagnetic 3d elements, it is possible to marry the best features of 4f and 3d magnetism. R-R interactions in the rare-earth transition-metal intermetallic compounds are generally quite small by comparison with R-T and T-T interactions, and are often neglected. The R-T interaction is indirect because there is almost no overlap between 4f shells of R atoms and 3d shells of T atoms. The 5d electrons are involved as the intermediary. Then, the coupling between the transition-metal spin and the rare-earth spin, will be different depending on the rare-earth element involved. The 4f-5d interaction is invariably ferromagnetic, but the 5d-3d interaction will be antiferromagnetic when the 5d band is less than half full and the 3d band is more than half full. In this way, the magnetisations of rare-earth and transition-metal sublattices couple parallel for the light rare-earths ($J = L - S$) and antiparallel for the heavy rare-earths ($J = L + S$).

2.2.2 Exchange interactions

The orientation of adjacent local magnetic moments is determined by the exchange interaction between them, which can be expressed in terms of a Heisenberg Hamiltonian

$$H_{ex} = -2J_{ex}\boldsymbol{S_i}\cdot\boldsymbol{S_j} \tag{2.2}$$

where J_{ex} is the exchange integral and S_i and S_j are the spins of the two ions i and j. J_{ex} is positive for a ferromagnetic interaction (spins coupled parallel) and negative (antiparallel) for an antiferromagnetic interaction between the two ions, and it falls off rapidly with increasing distance between them.

The T-T interaction dominates in an R-T alloy, due to direct overlap of the 3d shells on neighbouring sites. This interaction is described by a Hamiltonian as in (2.2) but now substituting S_T for S, where S_T is an effective spin defined for the transition element from its atomic moment in the solid, m:

$$m = gS_T\mu_B \tag{2.3}$$

with $g = 2$. This is important because the 3d atoms are not ions with an integral number of electrons (the division of the corresponding integral number of (3d + 4s) electrons between the two bands leads to a nonintegral number of electrons in the 3d band, as follows from the electron theory).

In the corresponding Hamiltonian for R-R interaction the contributions from spin and orbit must be considered, so $\boldsymbol{J}$ will be the quantum number to be used.

It is possible to establish an approximate relation between the exchange integral, J_{ex}, and the Curie temperature, T_C, using the mean field approximation in combination with Eq. (2.2). In the mean field approximation the exchange interaction, which must be summed up over all pairs of two atoms, is replaced by a molecular field which acts on a single moment and which is generated by all the other moments in the crystal; the spontaneous magnetisation of ferromagnets can be approximated by the Brillouin function. Considering one atom with z nearest neighbours connected by the interaction J_{ex}, this gives in combination with (2.1) [3]:

$$T_C = \frac{2zJ_{ex}S(S+1)}{3k_B} \tag{2.4}$$

where k_B is the Boltzmann constant. This expression is adapted for 3d metals replacing S by S_T.

It must be taken into account that a complete description of the magnetisation and the Curie temperature of a R-T intermetallic compound should consider, besides the dominant T-T interaction, the R-T and R-R interactions. This is usually done via the molecular field theory using Brillouin functions to describe the magnetisation of each sublattice ("two

sublattice model"); the molecular field acting at a T-site or an R-site will be the superposition of contributions from the T and R sublattices. However, equation (2.4) provides a correct T_C value in good approximation, considering only the main T-T interaction.

2.2.3 Anisotropy

In ferromagnetic crystals, certain directions are preferred (easy) directions of magnetisation. For Fe, which has a body-centered cubic structure (bcc), the easy direction of magnetisation is of the type $\langle 100 \rangle$. Co with a hexagonal close-packed structure can be easily magnetised along the c axis ([0001]).

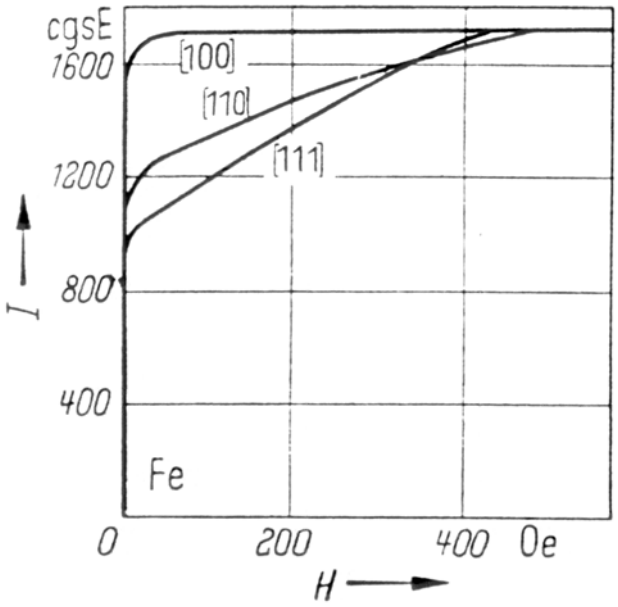

Fig. 2.3: Saturation of bcc-Fe under application of a magnetic field in different crystallographic directions. Saturation can be achieved in lower fields in the [100] direction ("easy direction" of magnetisation); (from Chikazumi [1]).

The interaction between localised electrons and crystalline electric fields (or crystal fields), which tend to align the spontaneous magnetisation along certain preferred directions in a crystal, is called magnetocrystalline anisotropy. For a field applied along a non-easy direction, a substantial field will be necessary to rotate all the atomic moments out of the easy axis and into the direction of the field, that is, to saturate the magnetisation. This is because the applied field must act against the force of crystal anisotropy, which is

often fairly strong. Then, a crystal anisotropy energy is stored in a crystal when J_s points into a non-easy direction. The crystal anisotropy is not only based on crystal fields but also on the spin-orbit coupling because the magnetisation is dominated by the spin (of 3d and 4f electrons) and the crystal fields act on the orbital part of the wave functions, only. The anisotropy energy can be defined as the energy required to rotate the magnetisation away from the easy direction. In a material with uniaxial symmetry (e.g., hexagonal cobalt) it may be described by:

$$E_a = K_1 sin^2\theta + K_2 sin^4\theta + \sigma(\theta^6) \tag{2.5}$$

where K_1 and K_2 are the anisotropy constants (in first approximation, they can be associated with the work necessary to rotate the direction of magnetisation from the easy direction to that perpendicular to it); θ is the angle formed by the magnetisation and the easy direction; $\sigma(\theta^6)$ includes all the terms in θ with power ≥ 6. The anisotropy energy can be represented by a ficticious magnetic field H_a (anisotropy field), which is parallel to the easy direction and reproduces the energy increase due to small deviations from the easy axis [1]:

$$H_a = \frac{2K_1 + 4K_2}{J_s} \tag{2.6}$$

In structures with one preferred crystallographic direction (*c* direction), i.e. hexagonal, rhombohedral or tetragonal, K_1 usually dominates over the other anisotropy constants. If K_2 is neglected in (2.6), $K_1 > 0$ means that *c* is the magnetically easy direction. This type of anisotropy is called easy-axis or uniaxial anisotropy. In the case of $K_1 < 0$ the anisotropy is said to be of easy-plane type. The anisotropy constants differ for different materials and almost always decrease as the temperature increases and become essentially zero even before the Curie temperature is reached. In R-T intermetallics the contribution of the R sublattice to K_1 usually is an order of magnitude larger than that of the T sublattice. Only at high temperatures the T sublattice is dominant because of the rapid decrease of the R sublattice anisotropy with increasing temperature.

2.2.4 Magnetic domains

In thermal equilibrium, a ferromagnetic material consists of magnetic domains [6], and these find their origin in the lower magnetostatic energy, in comparison to a state

where the material has a net magnetisation. In a material with sufficiently large grains, the number and the size of domains in the sample is the result of a balance between the domain wall energy produced by the splitting into domains and the lowering of the magnetostatic exchange energy. The change of the spontaneous magnetisation from a domain to its neighbour, occurs at the domain wall. The spins within the wall ("Bloch wall") are pointing in non-easy directions, so that the anisotropy energy within the wall is higher than in its adjacent domains. The exchange energy, γ_{ex}, tries to make the wall as wide as possible. In order to make the angle between adjacent spins as small as possible, the anisotropy energy, γ_a, tries to make the wall thin, i.e. reducing the number of spins pointing in non-easy directions. The result of this competition will be a certain finite width resulting from minimizing the total energy:

$$\gamma = \gamma_{ex} + \gamma_a \tag{2.7}$$

Figure 2.4 shows, as an example, the particular case of two magnetic domains with antiparallel magnetisations ("180° Bloch wall"). The wall width δ_w is proportional to the exchange length $l_{ex} = (A/K_1)^{1/2}$ with A being the exchange stiffness ($A \sim 10^{-11}$ Jm^{-1} at room temperature). Another characteristic length is the critical single-domain particle size given by the proportionality: $d_c \sim \mu_0(A/K_1)^{1/2}/J_s^2$ which describes the size of the largest possible isolated spherical crystallite in which the energy cost for the formation of a domain wall is higher than the gain in magnetostatic energy. Typically, Fe-based R–T permanent magnets

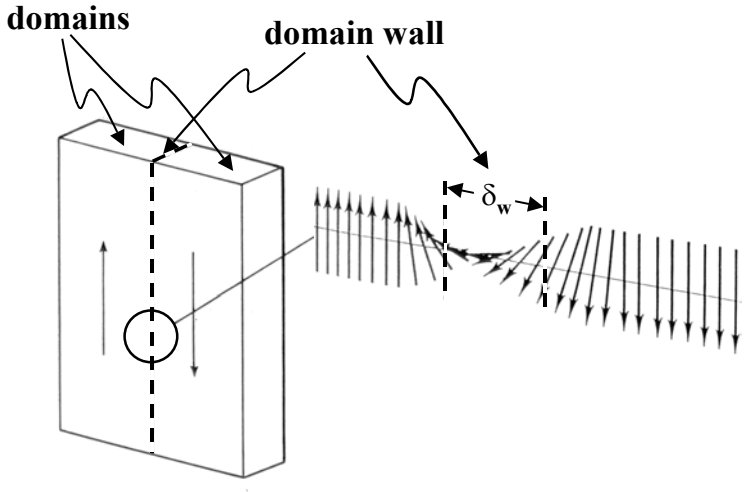

Fig. 2.4: Schematic representation of two magnetic domains antiparallelly magnetised. Dashed line represents the domain wall showing a detail in right hand side (δ_w: domain wall width); (adapted from Coey [3]).

have a critical single-domain particle size of d_c = 200-300 nm [7].

Because in R-T intermetallic compounds the T-T interactions dominate over R-T and R-R interactions, the balance between exchange energy and anisotropy energy, at any position in the wall, may thus be considered by taking the T moments as a reference (corresponding angle from the easy axis). The anisotropy energy for these alloys must include the R anisotropy and exchange interactions in addition to the T anisotropy.

In fine-grained polycrystalline materials with grain sizes sufficiently less than d_c the grains will be single domain and Bloch walls cannot develop. However, due to the magnetic interaction (exchange as well as magnetostatic) across the grain boundaries, competitive magnetic phenomena called interaction domains will occur [6,8-11]. The contrast and the visibility of the interaction domains is increased if the polycrystalline material is well textured [3,12,13]. Figure 2.5 shows, as an example, the Kerr image corresponding to a die-upset melt-spun NdFeB sample.

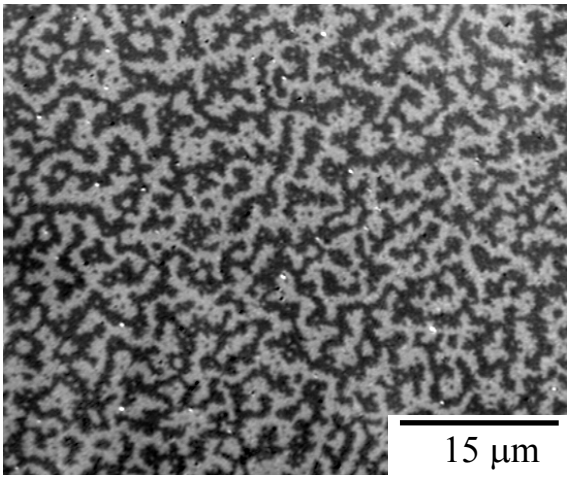

Fig. 2.5: Kerr image showing the domains on a die-upset melt-spun NdFeB sample (MQU-F), with the c-axis perpendicular to the imaging plane (courtesy O. Gutfleisch).

2.2.5 Origin of coercivity

Once the magnetic domains are aligned along the direction of an applied magnetic field, the formation of reversed domains is necessary in order to demagnetise the material. An upper limit of the coercivity is the anisotropy field H_a (Eq. (2.6)). However, the coercivity values of real materials are much less than the corresponding theoretical maximum values (Brown's paradox). This is because the formation of reverse domains is a

highly structure-sensitive process affected by the inhomogeneous structure of all real magnets. A plausible description of the coercivity is given by a linear combination of the anisotropy field H_a (2.6) and the saturation polarisation J_s:

$$H_C = \alpha \frac{2K_1 + 4K_2}{J_s} - \frac{N_{eff}}{\mu_0} J_s \tag{2.7}$$

where α is a temperature dependent microstructural parameter, less than unity, describing the reduction of the crystal field by defects as well as by misaligned grains; N_{eff} takes into account demagnetising fields [14-17]. Nucleation of reverse domains, originating at imperfections or at irregularities at the grain boundaries, is one of the main factors that reduces the coercivity.

Easy-axis anisotropy is indispensable for maintaining the metastable domain configuration required for a permanent magnet. Modern high performance magnets are, therefore, based on compounds of a magnetic light rare earth (Pr, Nd, Sm) for anisotropy and a 3d element (Fe, Co) for magnetisation and high Curie temperature. The particular rare earth needed for uniaxial anisotropy is determined by the symmetry of the site it occupies in the crystal structure.

As alternatives to the nucleation of reverse domains, the coercivity can also be controlled by the growth of small residual (or nucleated) reverse domains [18] or by pinning of domain walls by inhomogeneities. Formula (2.7) can be used as a rough description of all these coercivity mechanisms. Initial magnetisation curves are very different for nucleation-controlled magnets and pinning-controlled magnets (see Fig. 2.6). Saturation can be achieved at very low applied fields in the former ones due to very mobile domain walls whereas their motion is impeded by the pinning centers for the latter ones. Necessary conditions for having a nucleation-controlled coercivity are a defect-free microstructure and smooth grain boundaries. High coercivity is obtained in this type of magnets because it is difficult to nucleate reverse domains. This can be easily understood considering that the typical grain size of these magnets is much larger than the critical single domain size, so that once a domain wall is created, it will easily run across the grain. Examples of nucleation-controlled permanent magnets are sintered $Nd_2Fe_{14}B$ and bonded $SmCo_5$, $Nd_2Fe_{14}B$ and $Sm_2Fe_{17}N_3$ magnets [20-26]. Nucleation of reverse domains can also govern the coercivity in fine-grained materials with a grain size less than the critical

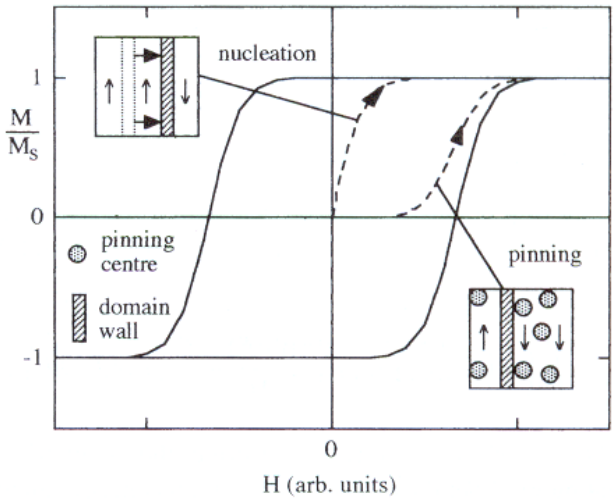

Fig. 2.6: Hysteresis loop for a permanent magnet material indicating by dashed lines the characteristic initial magnetisation curve for the case of pinning and nucleation mechanisms (from Skomski and Coey [19]).

single domain size diameter [11,27]. The detailed demagnetisation behaviour of such materials will depend on the type and the strength of the magnetic interaction between the small grains. The magnetisation process of a certain class of fine-grained magnets will be discussed in Section 3.3 and Chapter 8.

The pinning mechanism is typical of materials with pronounced nanoscale inhomogeneities. The effectiveness of the pinning will depend on the geometry and spatial distribution of the pinning centers, being necessary a sufficiently high density of such centers not uniformly distributed [28]. The pinning will be most pronounced when the size of the pinning centers is comparable to the domain wall width. In addition sharp boundaries may be very effective pinning centers. Sm_2Co_{17}-based magnets constitute a good example of this type of magnets where the pinning of the domain walls takes place in the $SmCo_5$ boundary phase [28,29].

3 The exchange-coupling mechanism

A high remanence, together with preserving a high coercivity, is a requirement to achieve maximised energy densities. Highest remanences are usually realised in textured microcrystalline sintered magnets, textured nanocrystalline hot-deformed magnets or textured HDDR powders. In these cases, J_r ideally approaches J_s. The remanence limit for isotropic magnets is given by $J_r / J_s \leq 0.5$, considering non-interacting uniaxial single domain particles [30]. An effective way of overcoming this limit is by means of exchange-coupling between neighbouring grains. The effectiveness of the exchange-coupling, i.e. degree of remanence enhancement, depends on the intrinsic magnetic properties including the micromagnetic parameters and the actual microstructure. A simple increase in the remanence, however, does not automatically lead to high energy densities since $\mu_0 H_c \geq J_r / 2$ has to be fulfilled additionally and the shape of the demagnetisation curve must not differ too much from the ideal one discussed in Section 2.1. Remanence enhancement is generally attributed to intergrain exchange interactions between neighbouring grains which causes the spontaneous magnetic polarisation of each individual grain to deviate from its particular easy axis towards the direction of the polarisation of the nearest ones. A schematic representation is shown in Fig. 3.1.

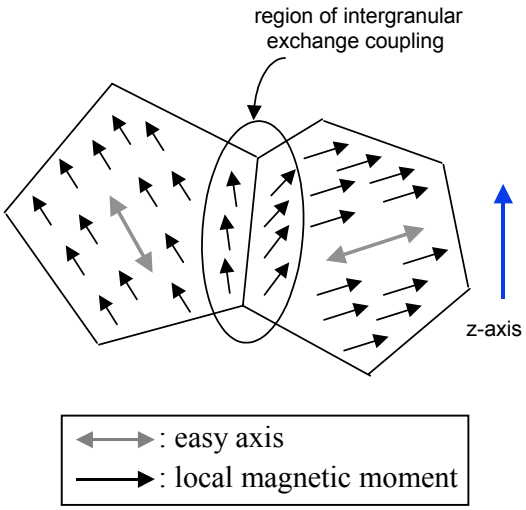

Fig. 3.1: Exchange-coupling mechanism.

3.1 Models

Different numerical models to describe the exchange-coupling effect in different systems can be found in the literature [31-36]. The corresponding results help to understand the effects of microstructural features on remanence and coercivity. In the following we focus mainly on the conclusions derived from the theoretical treatment presented by Kneller and Hawig [31] and the numerical model from Schrefl *et al* [33] to describe and predict the magnetic properties of nanocrystalline isotropic NdFeB magnets. The former model focuses on the theoretical treatment of two-phase nanocomposite magnets assuming a one-dimensional model of the microstructure and using the micromagnetic structure as a basis for the calculation of the critical dimensions of the phase regions. The latter model considers (a) a two-dimensional microstructure (with a quantitative treatment of size and shape of the grains), (b) short-range exchange and long-range magnetostatic interactions between the particles and (c) magnetic moments which might be inhomogeneously arranged within a grain (calculation of their distribution at the grain boundary being possible).

3.1.1 Single-phase nanocrystalline magnets

It was in 1983 when Sumitomo [20] and General Motors (GM) [37] announced new permanent magnets based on $Nd_2Fe_{14}B$. The Sumitomo magnets were made by sintering of magnetically aligned powder whereas GM used rapid solidification by melt-spinning. Three years after the announcement of NdFeB, Keem and co-workers [38] added small amounts of silicon or aluminium to a NdFeB alloy and reported a significant enhancement in J_r, substantially above the Stoner-Wohlfarth limit, despite the isotropic structure of the melt-spun alloy. This effect was ascribed to a refinement of the mean grain size to a value of about 20 nm. Clemente *et al* [39] used the melt-spinning technique to fabricate flakes composed of isotropically oriented microcrystallites of the $Nd_2Fe_{14}B$-type phase, which exhibited enhanced remanences. They proposed that this phenomenon arises from an intergranular magnetic exchange interaction. Manaf *et al* [40,41] demonstrated that, as the mean grain size is refined below ~35 nm, the remanence is progressively enhanced and the coercivity is reduced. They also demonstrated that similar degrees of remanence

enhancement to those obtained by Si or Al additions could be achieved in ternary NdFeB by controlling the quenching parameters.

The first important result, in good agreement with experimental data, is that the remanence of randomly oriented nanocrystalline particles which are strongly coupled by exchange interactions increases with decreasing grain size. However, exchange-coupling of neighbouring grains favors the nucleation of reversed domains leading to a reduction in coercivity.

The deviation of the magnetic moments from the local easy axis near grain boundaries determines remanence and coercivity of nanocrystalline permanent magnets. A smooth transition of the local J_s from one easy axis direction to the other takes place over a characteristic length resulting from a compensation between the magnetocrystalline anisotropy and the exchange interaction (see Section 2.2.3). In the ideal case of "clean" grain boundaries (without any additional phase), the width of these regions where the spins deviate from the easy axis can be compared with the domain wall width which can be written in first approximation as $\delta_w \approx \pi(A/K_1)^{1/2}$, where A is the exchange stiffness constant and K_1 is the first magnetocrystalline anisotropy constant. A significant number of

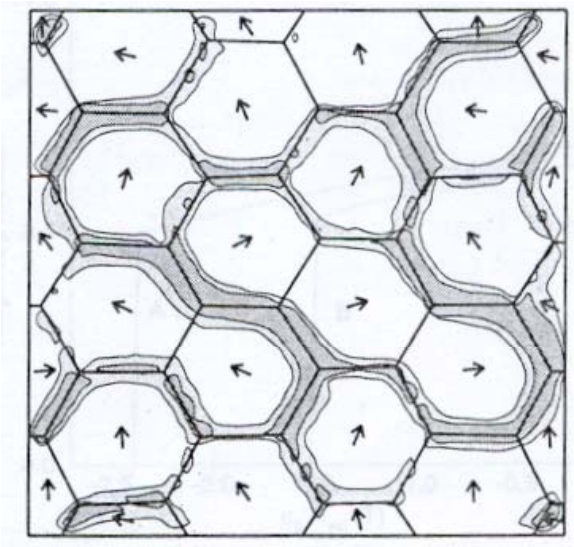

Fig. 3.2: Exchange-coupling effect between neighbouring grains in the remanent state. The arrows indicate the directions of the easy axes and the shaded areas the deviations of the magnetic moments from those ones by more than 20^o (darkest region) and 10^o; (from Schrefl et al [33]).

magnetic moments deviating from the easy axis is necessary to have a high degree of remanence enhancement. This situation is schematically illustrated in Fig. 3.2 where the remanent state of an ideal nanostructure with grain sizes of 20 nm can be observed. The shaded areas represent the regions where the magnetic moments deviate from the local easy axis by more than 20^o (darkest regions) and 10^o, respectively. Smaller grains will result in a more effective exchange-coupling, i.e. enlarged remanence by comparison with that of non-interacting particles.

A mean grain size < 20 nm and a homogeneous microstructure, with a very small range in grain size, were established as requirements to obtain an enhanced remanence preserving a high coercivity in NdFeB based magnets [33,42].

3.1.2 Two-phase nanocomposite magnets

In 1988, Coehoorn *et al* [43] reported for the first time that two-phase nanocomposite magnets, containing 85% soft magnetic phases (73% Fe_3B and 12% bcc-Fe) and 15% hard phase ($Nd_2Fe_{14}B$), could be prepared by crystallisation of amorphous melt-spun alloys with approximate compositions of $Nd_4Fe_{78}B_{18}$ having remarkable permanent magnet properties ($\mu_0 H_c \approx 0.4$ T, $(BH)_{max} = 95$ kJm^{-3}). Eckert *et al* [44] showed that it is the interaction between the soft and the hard magnetic phases which results in the specific hysteresis loop and the very steep recoil loops [45]. These permanent magnets consist of two different ferromagnetic and mutually exchange-coupled phases, one of which is hard magnetic to provide a high coercive field, while the other is soft magnetic providing a high saturation polarisation.

One of the main results derived from the models is that a small enough grain size improves both remanence and coercivity of isotropic two-phase magnets. Too large grains will result in a non-effective exchange-coupling of the soft magnetic phase due to a short range of the exchange interactions unable of aligning completely the magnetic moments of the grains of the soft phase. However, too small grains could result in a drop in coercivity due to exchange interactions between hard magnetic grains. Thus, the aim is to develop a nanostructure consisting of small enough grains to increase the remanence while preserving a high coercive field, which will result in remarkable high-energy products. Numerical calculations show an effective exchange hardening of the soft magnetic phase when the corresponding grains are about twice the domain wall width of the hard phase.

This can be easily understood when considering the schematic one-dimensional model proposed by Kneller and Hawig [31] (Fig. 3.3): the initial state represents the saturation remanence where all the magnetic moments are considered to remain aligned along one direction after removal of the applied magnetic field necessary to achieve the saturated state, and the following equilibrium states correspond to the demagnetisation of the sample in an increasing reverse field *H*. An optimum grain size of the soft phase of about $2\delta_w$ of the hard phase will yield that the exchange fields from nearest neighbouring hard grains situated at both sides fully cover the soft grain resulting in an effective exchange hardening (alignment of the magnetic moments) in the soft grain.

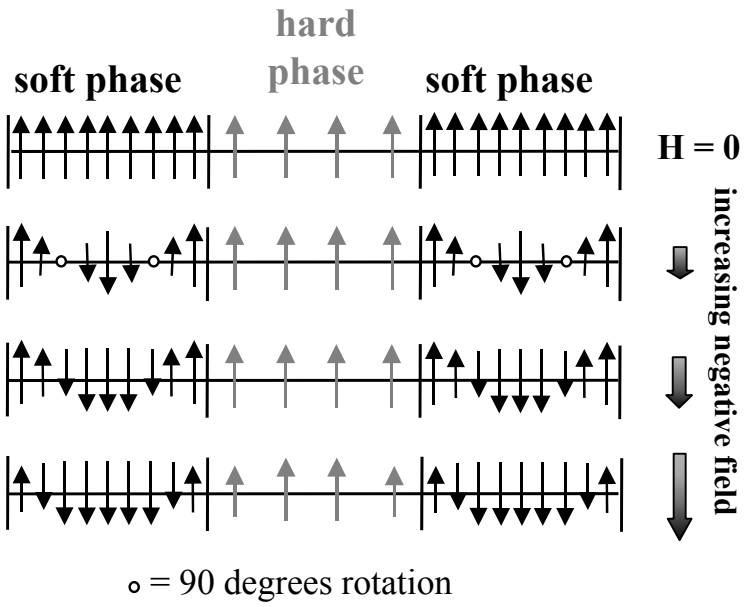

Fig. 3.3: Schematic one-dimensional model of the micromagnetic structure of an exchange-coupled nanocomposite material (adapted from Kneller and Hawig [31]).

According to numerical calculations, two-phase α-Fe/$Nd_2Fe_{14}B$ magnets with a grain size of 20 nm would exhibit a maximum energy product of about 350 kJm^{-3} for a volume fraction of the soft magnetic phase of 40% [33].

3.2 Wohlfarth's relation and Henkel-plot

An analysis of the remanence relationship of Wohlfarth [46]

$$J_r^d(H_m) = J_r - 2J_r^m(H_m) \tag{3.1}$$

can help to clarify the nature of the magnetisation processes. $J_r^d(H_m)$ is the remanence after application of a reverse field, $-H_m$, to the saturated sample; J_r is the remanence of the material, measured after saturation ($H_m \rightarrow \infty$); $J_r^m(H_m)$ is the remanence after application and removal of the maximum field H_m to a thermally demagnetised sample. Measurements of these quantities are shown in Fig. 3.4 for a typical exchange-coupled two-phase nanocomposite magnet.

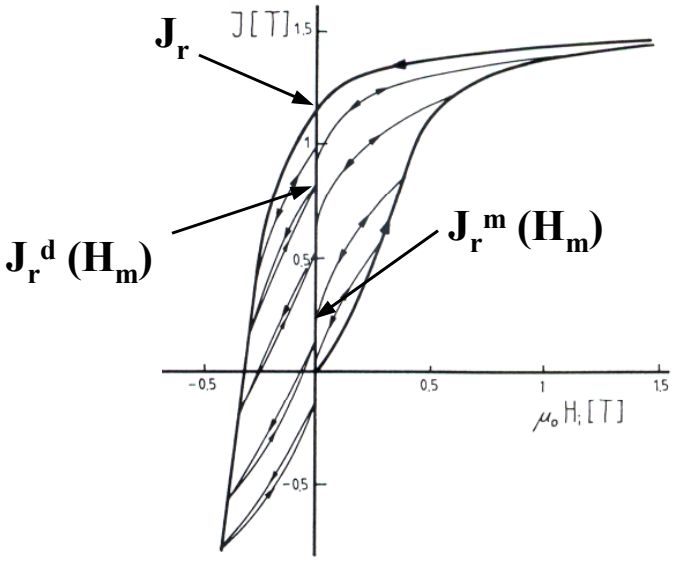

Fig. 3.4: First magnetisation and demagnetisation curves for an exchange-coupled two-phase composite magnet (Fe_3B / $Nd_2Fe_{14}B$); (adapted from Schneider et al [45]).

However, some important requirements must be considered for the validity of Wohlfarth's relation: the system must consist of an assembly of non-interacting magnetically uniaxial single-domain particles and the sample must be initially in the thermally demagnetised state. Thus, a plot of $J_r^m(H_m)/J_r$ vs. $J_r^d(H_m)/J_r$ would result in a straight line as that shown in Fig. 3.5 for a system where the validity requirements are verified. This is the so-called "Henkel-plot" [47] which is a simple and elegant way of presenting Wohlfarth's relation independent of the applied magnetic field. However, exchange-coupling implies interactions between particles and, as a consequence, a deviation from that linear behaviour as it can be seen in Fig. 3.5.

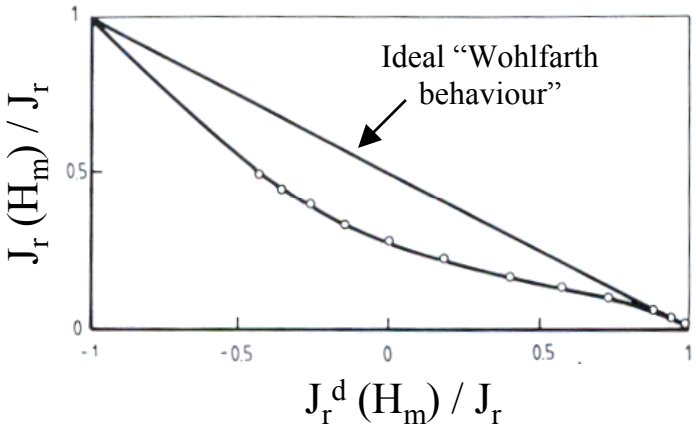

Fig. 3.5: Henkel plot: Graphical representation of Wohlfarth's relation for an assembly of non-interacting magnetically uniaxial single domain particles (straight line) and deviations from that relation for the case of an exchange-coupled two-phase composite magnet (Fe_3B / $Nd_2Fe_{14}B$); (adapted from Schneider et al [45]).

3.3 Magnetisation reversal processes in nanocomposite magnets

The generally accepted mechanism of magnetisation reversal in fine grained two-phase magnets [31] can be summarised as follows: under the action of a reverse field the magnetisation vector of the soft magnetic phase rotates towards the field until it becomes energetically unfavourable to support the non-uniform magnetisation at the interface. At this point the magnetisation of the hard magnetic phase undergoes an irreversible change. The critical field for reversal of the hard phase is significantly higher than the coercivity of the uncoupled soft phase, but less than that of the hard phase and exhibits a strong dependence on the scale of the microstructure.

3.3.1 Recoil loops and "exchange-spring" magnet behaviour

In this work decoupled, exchange-coupled nearly single-phase and exchange-coupled nanocomposite magnets will be studied. An analysis of the inner loops recorded during the demagnetisation process by the application of reverse fields $-H_m$ (recoil loops) can give information about the processes involved. Decoupled magnets and single-phase exchange-coupled magnets exhibit completely closed recoil loops whereas those of composite magnets are relatively open (see Fig. 3.4). The explanation can be found by looking at one of the intermediate micromagnetic states shown in Fig. 3.3: for an optimum size of the soft

magnetic grains, the application and removal of a certain applied reversed field smaller than the critical field described above will bring the system back to the state where all the magnetic moments are aligned due to the exchange-coupling effect between the soft and the hard grains. This reversible rotation of the exchange coupled soft phase for fields not large enough to reverse the magnetisation of the hard magnetic phase was discovered by Schneider *et al* [45] and termed "exchange-spring" mechanism by Kneller and Hawig [31]. General criteria for the presence of the "exchange-spring" mechanism are:

(a) although there are two different magnetic phases, the major demagnetisation curve shows a magnetically single-phase behaviour;

(b) the ratio of remanence to saturation polarisation is higher than 0.5;

(c) the recoil curves show a relatively high degree of reversibility in fields below coercivity ("high recoil permeability").

3.3.2 Intergrain interactions: δJ-plot

The interactions between the grains can also be studied by plotting the quantity δJ defined as: $\delta J = (J_r^d(H_m) - (J_r - 2J_r(H_m))) / J_r$ (also known as δJ- or δM-plot which is a graphical presentation of Wohlfarth's relation (3.1) in dependence on the applied magnetic field). This relationship gives the deviations from the theoretical value for $J_d(H_m)$ given by Wohlfarth's relation [46]. Two kinds of interactions can be responsible for the deviation from this latter relationship: magnetostatic and exchange interactions. However, different interpretations can be found in the literature concerning the sign of δJ [24,45,48-54]. In this study the working hypothesis of Ding *et al* [52], that positive values of δJ are indicative of predominant magnetostatic interactions whereas negative ones indicate the main role played by the exchange interactions in two-phase nanocomposite magnets, could be supported by analysing numerous experimental data.

3.3.3 Nucleation field

In permanent magnets based on rare-earth transition-metal compounds, the value of the coercive field deviates considerably from the predictions of the conventional Stoner/ Wohlfarth theory. This discrepancy is normally ascribed as Brown's paradox and attributed to microstructural effects. For an ideal microstructure, where nucleation of reverse

domains does not take place, coercivity equals the nucleation field, H_{no}. Thus, the nucleation field can be defined, considering as initial state that of initial saturation remanence [31], as the reversal field required to make the domain wall invade the hard phase. In other words, an applied field $H \geq H_{no}$ will lead to irreversible polarisation reversal. Reversible polarisation values, J_{rev}, can be obtained from the recoil loops. This quantity is defined as the difference in polarisation obtained when traversing the recoil curve, starting from a point on the demagnetisation curve for a given field and terminating on the recoil curve at zero field. The irreversible polarisation is defined as $J_{irr} = [J_r - J_r^d(H_m)] / 2$. According to the model of Kneller and Hawig [31], the maximum of the derivative dm_{irr} / dH (where $m_{irr} = J_{irr} / J_r$) would correspond to the nucleation field, H_{no}, for irreversible polarisation. This derivative will be termed for abbreviation irreversible susceptibility, $\chi_{irr}(H)$, (although it has unit of T^{-1}) following the notation used by McCormick *et al* [55]. Non-simultaneous switching of the hard and the soft magnetic phases leads to differences between the coercivity and the nucleation field.

3.4 Development of exchange-coupled nanocrystalline magnets

In the last decade a lot of studies have been focused on the development of two-phase or multiphase magnetic materials. These materials present two clear advantages compared to common isotropic (i.e. non-textured) hard magnetic materials: a higher saturation polarisation and a lower rare-earth content which decreases the cost of the magnet. The presence of the soft magnetic phase decreases the coercive field but enhances the remanence with respect to the single hard magnetic phase. Thus, it is expected that, by optimising the contents of the two phases as well as the microstructure, improved values of the energy product can be achieved.

Coehoorn *et al* [43] reported a considerably increased remanence of melt-spun permanent magnets of nominal composition containing a substantial fraction of Fe_3B grains.

The use of specific additives to improve the magnetic properties has been the aim of several studies. Keem and co-workers [38] observed substantial remanence enhancement in the stoichiometric $Nd_2Fe_{14}B$ by adding Si, due to a more refined microstructure.

Hirosawa *et al* [56] obtained the critical dimension of about 10 nm for a mutually coupled $Fe_3B/Nd_2Fe_{14}B$ mixture with melt-spun $(Nd,Dy)_xFe_{80.5-x-y}Co_yB_{18.5}M_1$ ($3 \le x \le 5$ and $0 \le y \le 5$) alloys where M represents additives (Al, Si, Cu, Ga, Ag, Au) used to reduce the grain size. In this way, a coercivity of 0.6 T and a remanence of 0.98 T were obtained in $Nd_3Dy_2Fe_{70.5}Co_5Ga_1B_{18.5}$. Ping *et al* [57] argumented that Co and Ga atoms control the grain growth of Fe_3B precipitates and contribute to the formation of the $Fe_3B/Nd_2Fe_{14}B$ nanocomposite with ultrafine grains, which leads to a high coercivity and an improved maximum energy product.

Uehara *et al* [58] explained how the addition of Cr contributes to the magnetic properties of these nanocomposite magnets produced by melt-spinning, providing a high coercivity. This is in good agreement with a previous study performed by Hirosawa and Kanekiyo [59] on $Fe/Nd_2Fe_{14}B$ nanocomposite magnets produced from melt-spun Nd-Fe-B-Co-Cr alloys with low-Nd and high-B concentration; they obtained magnetic properties between $(J_r,\mu_0 H_c)$ = (1.20 T, 0.43 T) and (0.86 T, 0.77 T), the large coercivity being due to a refinement of microstructure and an increase in the volume fraction of the hard magnetic $Nd_2(Fe,Cr)_{14}B$ phase produced by the partial replacement of Fe by Cr. Bauer *et al* [60] studied the relationship between the magnetic properties and the $Fe/Nd_2Fe_{14}B$ volume ratio, finding that a composite magnet containing 30 vol% bcc-Fe exhibits a maximum remanence of J_r = 1.25 T and an energy product of $(BH)_{max}$ = 185 kJm^{-3}. Melsheimer *et al* [61] compared the magnetic properties of three different Nd-Fe-Co-B magnets produced also by the melt-spinning procedure: a nanocrystalline exchange-coupled $Nd_2(Fe_{1-x}Co_x)_{14}B$ single-phase magnet, $Nd_2(Fe_{1-x}Co_x)_{14}B$ + $(Fe_{1-x}Co_x)$ composite magnets and a decoupled $Nd_2(Fe_{1-x}Co_x)_{14}B$ magnet with an overstoichiometric Nd content. As it was expected, they observed an enhanced remanence and a decrease in coercivity for both exchange-coupled magnets in comparison to the decoupled material. They obtained a uniform grain size (22-25 nm) for the single phase magnet, and a mixture of very small grains of a soft magnetic phase (< 20 nm) and small hard magnetic grains ($\approx$ 35 nm) for the composite magnet. The single-phase and the composite magnets exhibited maximum energy products of up to 175 kJm^{-3}, at T = 300 K, whereas only 93 kJm^{-3} was obtained for the decoupled magnet. In Fig. 3.6, hysteresis loops of a decoupled and an exchange-coupled magnet with compositions $Nd_{15}(Fe_{57.5}Co_{18.5})B_9$ and $Nd_{12}(Fe_{62}Co_{20})B_6$, respectively, are reproduced from that work.

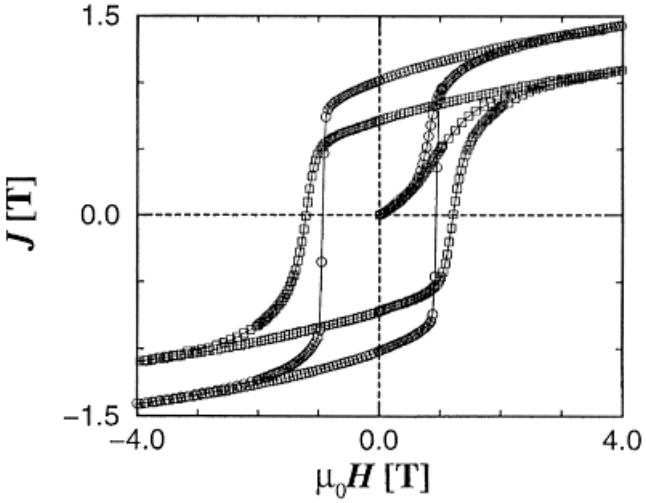

Fig. 3.6: Hysteresis loops of a decoupled (squares) and an exchange-coupled (circles) magnet (from Melsheimer et al [61]).

In a study about nanocomposites of Fe/$Nd_2Fe_{14}B$ produced by mechanical alloying, Crespo *et al* [62] reported values of $\mu_0 H_c \approx 0.37$ T and $(BH)_{max} \approx 92$ kJm^{-3} for $Nd_8Fe_{88}B_4$-based samples after optimum heat treatment, exhibiting average grain sizes of 33 nm and 28 nm for $Nd_2Fe_{14}B$ and bcc-Fe, respectively, whereas the addition of Zr (or Si) results in a refinement of the microstructure with average grain sizes of 20 nm (21 nm) and 19 nm (21 nm) for $Nd_2Fe_{14}B$ and bcc-Fe, respectively. This leads to improved magnetic properties: $\mu_0 H_c \approx 0.44$ T and $J_r \approx 1.03$ T with Zr addition, and $\mu_0 H_c \approx 0.40$ T and $J_r \approx 1.06$ T with Si addition (both of them after heat treatment at $T = 650$°C). Neu *et al* [63] performed a study about nanocrystalline single-phase Nd-Fe-B powders produced by intensive milling and heat treatment, obtaining a remanence of $J_r = 0.92$ T and a maximum energy product of $(BH)_{max} = 132$ kJm^{-3} for a microstructure with an average grain size of about 30 nm. Further Co addition improved the remanence to $J_r = 0.95$ T, and the energy density to $(BH)_{max} = 140$ kJm^{-3}, due to a smaller grain size of 21 nm.

Recently, several experimental studies have focused on optimising the mean grain size of the soft magnetic phase in order to achieve full exchange-coupling by the hard phase [16,64-66]. Goll *et al* [16] obtained a remanence of $J_r = 1.17$ T and a maximum energy product of $(BH)_{max} = 180$ kJm^{-3} in a nanocomposite $Pr_2Fe_{14}B$-based magnet containing 30 vol% α-Fe produced by melt-spinning. The average grain sizes of the hard and the soft magnetic grains were about 20-30 nm and 15 nm, respectively.

Nanocrystalline SmCo-based magnets have been widely studied since both $SmCo_5$ and Sm_2Co_{17} have higher Curie temperatures than other rare-earth transition-metal compounds used for permanent magnets and have many potential high-temperature applications [67-70]. Yan *et al* [71,72] have performed a systematic study of exchange-coupled nanocomposite $SmCo_5$ / Sm_2Co_{17} powders synthesised by intensive milling and subsequent annealing of as-cast alloy. A high coercivity of 2.40 T and a relative remanence J_r / J_s = 0.73 were obtained for a sample containing 40% $SmCo_5$ / 60% $Sm_2(Co_{0.74}Fe_{0.1}Cu_{0.12}Zr_{0.04})_{17}$ [72].

4 Systems under investigation

4.1 NdFeB

The stoichiometric composition of the magnetically highly anisotropic $Nd_2Fe_{14}B$ compound is $Nd_{11.8}Fe_{82.3}B_{5.9}$. The lattice symmetry is tetragonal (space group $P4_2/mnm$) with 68 atoms per unit cell. There are six crystallographically distinct transition metal sites, two different rare-earth positions, and one boron position (Fig. 4.1). Magnetisation curves measured at 300 K along different crystallographic directions show that the easy magnetisation direction is the *c* axis (right hand side in Fig. 4.1).

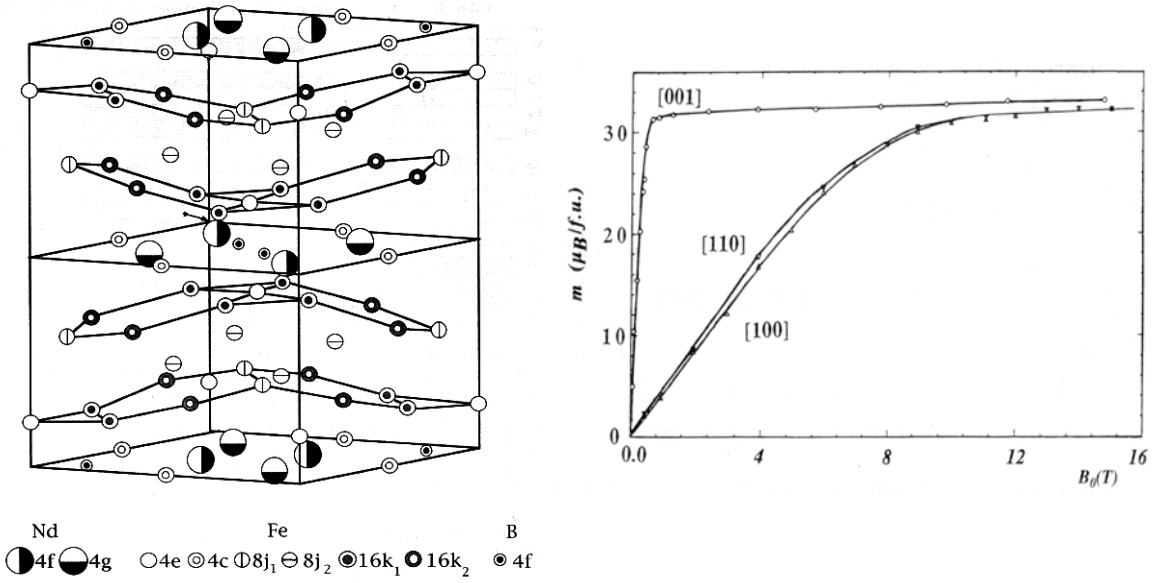

Fig. 4.1: (Left) tetragonal unit cell of the $Nd_2Fe_{14}B$ structure (from Herbst et al [73]); (right) magnetisation curves for single-crystal $Nd_2Fe_{14}B$ at T = 300 K (from Chikazumi [1]).

The intrinsic magnetic properties of $Nd_2Fe_{14}B$ are: $\mu_0 H_a$ = 6.7 T, J_s = 1.60 T and T_C = 312°C [37,74]. Thus, the upper limit of $(BH)_{max}$ is 516 kJm^{-3}.

Figure 4.2 shows the liquidus projection of the ternary Nd-Fe-B system. There are three stable ternary phases: $Nd_2Fe_{14}B$ (ϕ), $Nd_{1+\varepsilon}Fe_4B_4$ (η) and $Nd_5Fe_2B_6$ (ρ). The peritectic formation of the ϕ phase takes place at 1180°C but it will not be complete in a standard casting process because here γ-Fe is the primary solidification product.

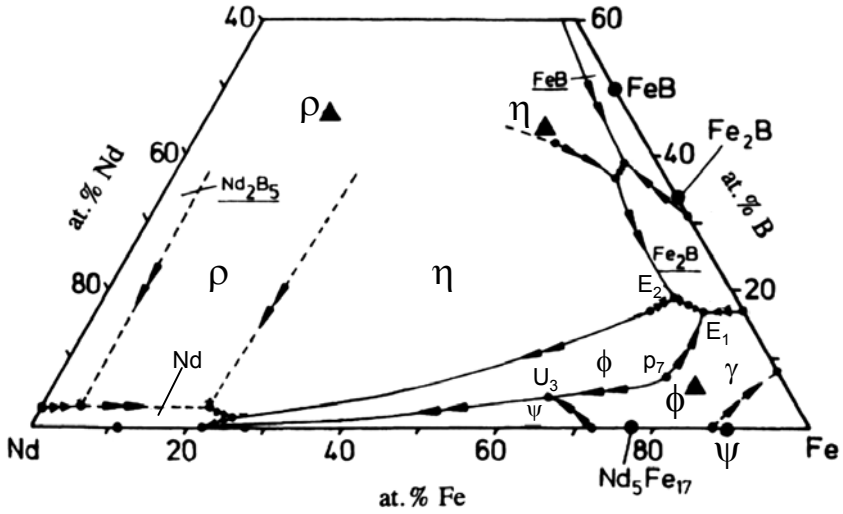

Fig. 4.2: Liquidus projection of the Nd-Fe-B system. Important reactions are p_7 (1180°C: $L + \gamma\text{-}Fe \rightarrow \phi$), U_3 (1130°C: $L + \gamma\text{-}Fe \rightarrow \phi + \psi(Nd_2Fe_{17})$), e_4 (1115°C: $L \rightarrow \eta + \phi$), E_1 (1105°C: $L \rightarrow \phi + \gamma\text{-}Fe + Fe_2B$) and E_2 (1095°C: $L \rightarrow \eta + \phi + Fe_2B$); (from Knoch et al [74] and Gutfleisch [7]).

The operation temperature for Nd-Fe-B-based magnets is limited by the relatively low Curie temperature, but in addition another limit is found at low temperatures: below 135 K a spin reorientation transition takes place, which basically consists in the development of a magnetisation component perpendicular to the local axis in the $Nd_2Fe_{14}B$ grains [75-77]. This results in a dip in the demagnetisation curve deteriorating significantly the magnetic properties. Figure 4.3 shows this effect for an isotropic sintered NdFeB-based magnet.

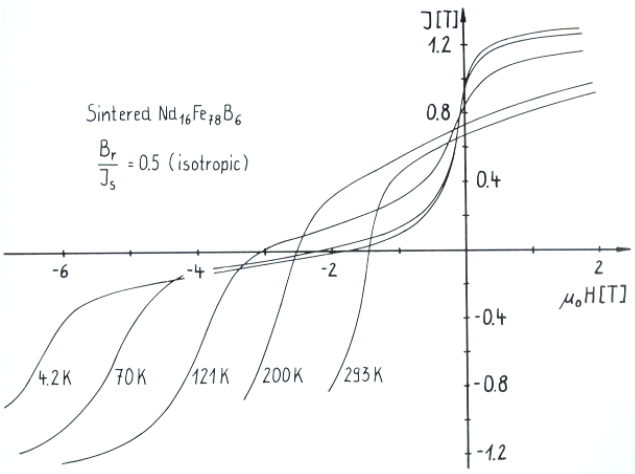

Fig. 4.3: Demagnetisation curves of isotropic sintered $Nd_{16}Fe_{78}B_6$ magnet for different values of temperature (from Handstein et al [77]).

4.2 NdCoB

The tetragonal structure of $Nd_2Fe_{14}B$ exists over the whole range of the $Nd_2(Fe_{1-x}Co_x)_{14}B$ composition ($0 \leq x \leq 1$), but there is a decrease in the lattice constants with increasing Co content [78-80]. The decrease in *c* is relatively large compared to that of *a*.

The substitution of Co by Fe in $Nd_2Fe_{14}B$, solves the main limitation of this compound: its relatively low Curie temperature. T_C increases with x because the Co-Co exchange interaction is stronger than the Co-Fe or the Fe-Fe interactions and reaches $T_C \approx$ 720°C for $Nd_2Co_{14}B$. The detailed variation of the Curie temperature with Co concentration depends on the distribution of the Co ions in the lattice. This substitution results in a decrease of the spontaneous magnetisation due to the lower value of the Co moment. However, a slight increase in the saturation polarisation has been observed for small amounts of Co replacing Fe (up to $x \approx 0.2$ in $Nd_2(Fe_{1-x}Co_x)_{14}B$) [81]. This can be ascribed to the sites occupied by Co ions in the lattice. The results corresponding to the total magnetic moments at T = 77 and 295 K determined by Fuerst *et al* [81] are reproduced in Table 4.1.

x: Co-cont.	0	0.1	0.3	0.5	0.7	0.9	1
m_{sat} (77K)	35.8	37.9	36.6	34.4	31.4	27.9	26.6
m_{sat} (295K)	32.1	34.4	33.5	30.8	28.7	25.3	23.6

Table 4.1: Saturation moments m_{sat} (μ_B / f.u.) at T=77 and 295 K for $Nd_2(Fe_{1-x}Co_x)_{14}B$ alloys (from Fuerst et al [81]).

A detailed study of the site occupancy preferences in $Nd_2(Fe_{1-x}Co_x)_{14}B$ was performed by Herbst and Yelon [73]. They observed that the moment on the site j_2 is the largest for each material, with the exception of $Nd_2Co_{14}B$. They determined that k_1, k_2, j_1 and *c* sites are populated nearly randomly while the j_2 site has a strong preference for occupation by Fe and the e site favors Co occupation although not as strongly as in the case of the j_2 site and Fe. However, Girgis *et al* [80] observed that Co atoms are more probably statistically distributed on the iron positions for low Co concentrations. This

would explain the higher saturation moment exhibited for low Co contents, in comparison with $Nd_2Fe_{14}B$.

The substitution of Fe by Co has a small effect on the magnetocrystalline anisotropy because the main contribution is from the rare-earth sublattice, but it is a negative effect having a decrease of H_a with Co addition. This effect was expected from the shrinkage of the lattice mentioned previously, i.e. of the decrease of the easy *c* axis. Figure 4.3 shows the decrease of the anisotropy field with increasing temperature of $Nd_2Fe_{14}B$ and $Nd_2Co_{14}B$. It can be seen that the decrease of the latter is faster, reflecting the weaker R-Co interactions.

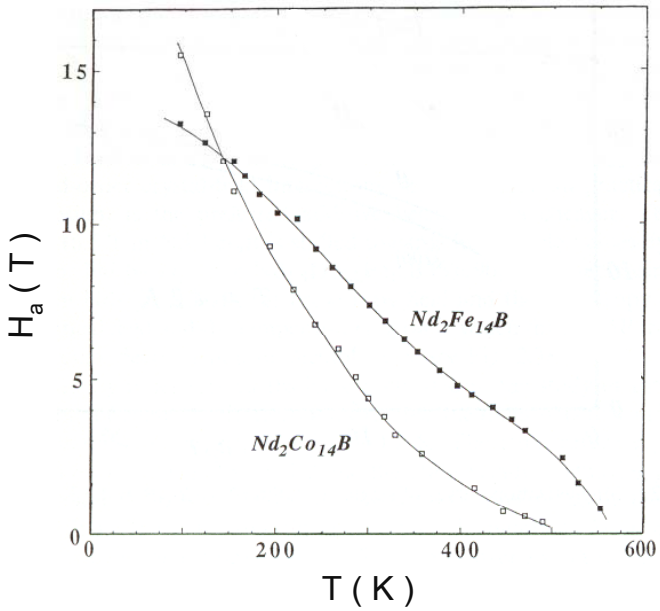

Fig. 4.3: The temperature dependence of the anisotropy field in $Nd_2Fe_{14}B$ and $Nd_2Co_{14}B$ (adapted from Coey [3]).

In conclusion, addition of Co constitutes an effective way of improving T_C, but a too high Co-content leads to a detriment of the magnetic properties besides an increase in the final cost of the magnet due to the higher Co price.

4.3 PrFeB

The $Pr_2Fe_{14}B$ compound also exhibits a tetragonal structure. The Pr-Fe-B phase diagram is very similar to that of Nd-Fe-B as it can be observed in Fig. 4.4. In terms of intrinsic magnetic properties, $Pr_2Fe_{14}B$ has a slightly lower saturation polarisation value (J_s = 1.56 T) and a lower Curie temperature (T_C = 297°C) than $Nd_2Fe_{14}B$ [83]. However,

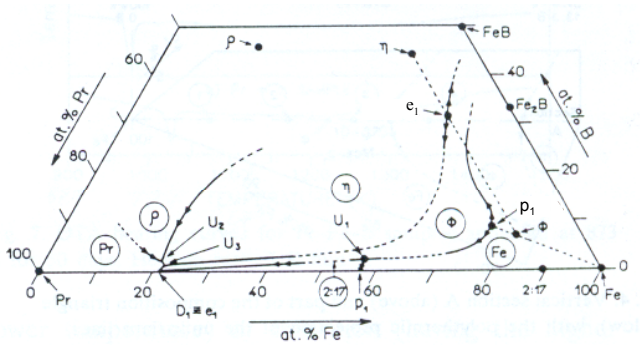

Fig. 4.4: Liquidus projection of the Pr-Fe-B system. Important reactions are p_1 (1125°C: L + γ-Fe → ϕ), U_1 (1355°C: L + γ-Fe → ϕ + ψ(Pr_2Fe_{17})) and e_1 (1090°C: L → η + ϕ); (from Neiva et al [82]).

the Pr-compound presents two important advantages: the higher anisotropy field ($\mu_0 H_a$ = 8.7 T) and no spin reorientation at low temperatures. The first advantage can be very useful to enhance the coercivity at the expense of the remanence, and the second one makes PrFeB-based magnets very attractive for low temperature applications, e.g. in conjunction with superconductors, where a high performance is required. Figure 4.5 shows the demagnetisation curves for a PrFeB-based magnet at low temperatures.

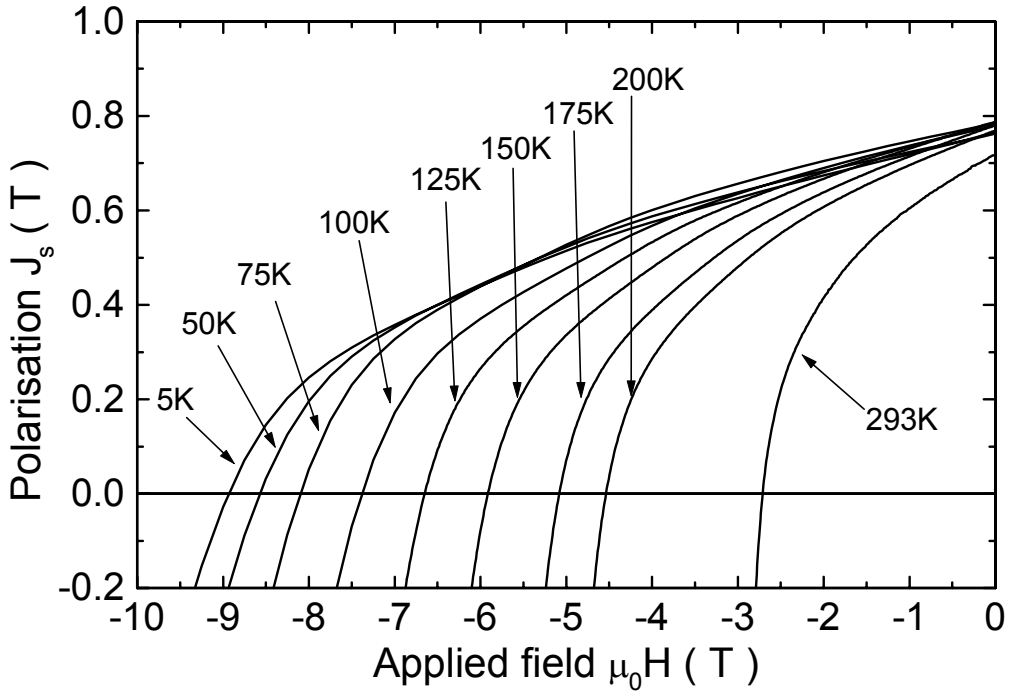

Fig. 4.5: Room temperature and low temperature demagnetisation curves for a PrFeB-based magnet processed by the intensive milling technique.

In addition to the mentioned advantages, at present, Pr is cheaper than Nd (about 2/3 of the price) resulting in lower costs of the final magnet.

Table 4.2 summarises the intrinsic magnetic properties and important microstructural parameters of $Nd_2Fe_{14}B$ and $Pr_2Fe_{14}B$ and, for comparison, α-Fe. Figure 4.6 shows the evolution of the domain wall width, δ_w, with temperature.

Compound	T_C (K)	$\mu_0 H_a$ (T)	K_1 (MJm^{-3})	J_s (T)	δ_w (nm)	d_c (μm)	reference
$Nd_2Fe_{14}B$	585	6.7	5	1.60	4.2	0.3	[20,37]
$Pr_2Fe_{14}B$	565	8.7	5	1.56	~4	~0.3	[16,83]
α-Fe	1043	-	-	2.16	30	-	[84]

Table 4.2: Intrinsic magnetic properties (Curie temperature T_C, anisotropy field $H_a = (2K_1 + 4K_2)/J_s$, anisotropy constant K_1, saturation polarisation J_s), domain wall width δ_w and critical single-domain particle size for magnetically uniaxial materials $d_c = 72\mu_0(AK_1)^{1/2} / J_s^2$ of $Nd_2Fe_{14}B$ and $Pr_2Fe_{14}B$. α-Fe has been added for comparison.

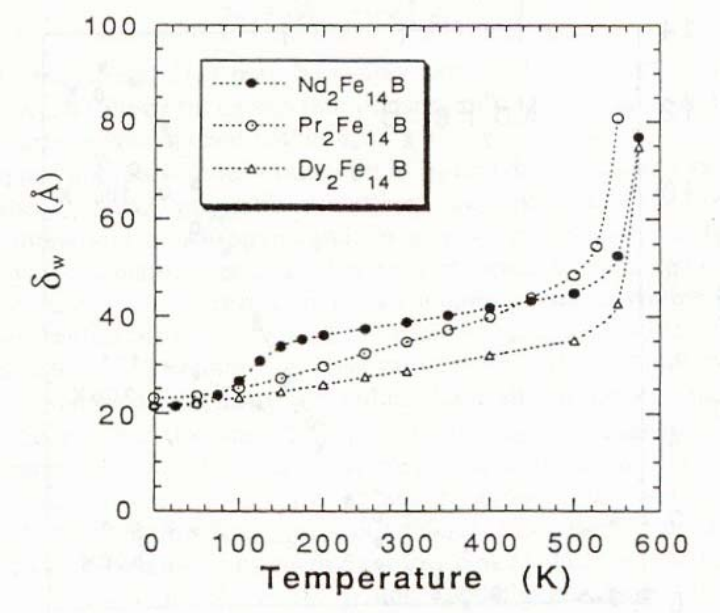

Fig. 4.6: Calculated domain wall width δ_w in $Nd_2Fe_{14}B$, $Pr_2Fe_{14}B$ and $Dy_2Fe_{14}B$ (from Givord and Rossignol [18]).

5 Experimental details

The different techniques used in the present work will be shortly explained in this Section. Additionally, specific experimental details will be given. The first part will focus on three different powder processing techniques: melt-spinning, high energy ball milling and reactive milling in hydrogen. The resulting magnets will be isotropic due to a randomly oriented grain structure. The hot deformation process will be shown as a way of producing highly dense anisotropic magnets. Characterisation of the materials after the different processing steps is fundamental in order to evaluate the efficiency of the chosen parameters during the experiment and, at the end, the quality of the resulting magnet. The employed techniques have been grouped into, first, those related to structural characterisation and, second, those ones necessary for characterisation of magnetic properties.

5.1 Nanocrystalline powder processing

In the following a brief summary of the different methods of processing alloys into particles with submicron or smaller grains is given. The aim of these processes is to create, at the end, a microstructure consisting of crystallites which are in size equal to or even significantly smaller than the corresponding single-domain size and, therefore, can resist effectively the formation and propagation of domain walls on reversal magnetisation and/or can show an effective exchange-coupling. “Nanocrystalline” is usually defined by grain sizes ≤ 50 nm. In the following this term will be used for a broader range in grain sizes (< 500 μm).

5.1.1 Melt-spinning

Melt-spinning is one of the principal fabrication routes for magnetic materials [37]. It involves ejection of a molten starting alloy through a crucible orifice onto the surface of a rapidly rotating copper wheel, to form a fine ribbon. The ribbon is either amorphous (over-quenching) or is composed of many randomly oriented nanocrystallites (direct-quenching) [85-88]. The process is carried out in an inert atmosphere (usually argon) because the rare-

earths are chemically very reactive. The high thermal conductivity of copper and the high surface velocity of the wheel, v_s, are responsible for the high cooling or quench rate (about 10^6 K/s) attainable by this technique, and it can be varied by changing v_s which, in a first approximation, is directly proportional to the cooling rate. There is a strong dependence of the coercivity on the wheel speed. The melt-spun ribbon is magnetically isotropic and forms the basis of a range of commercial magnets (so-called "MQ-powder: MQ1"). There are various production routes as, for example, hot-pressing (dense isotropic magnets: MQ2) with subsequent die-upsetting or backward extrusion (dense anisotropic magnets: MQ3) and polymer resin bonding techniques [89-93]. A more detailed explanation about the hot deformation process will be given in Section 5.1.4.

Ribbon flakes in this study were prepared changing the parameters (v_s = 30 - 40 ms^{-1}) according to the composition to obtain a partly amorphous structure. Heat treatment of the flakes was carried out at temperatures between 600 and 800 °C for 15 min under vacuum at pressures lower than 10^{-4} mbar.

5.1.2 High energy ball milling

Mechanical alloying was developed in the 1970s as a technique for dispersing nanosized oxide inclusions into nickel based alloy powders [94]. Yeh *et al* [95] were the first demonstrating an amorphisation by solid-state reaction using diffusion for the reaction of hydrogen with crystalline Zr_3Rh. Schwarz and Johnson [96] established the possibility of applying this method to metallic systems. Schultz *et al* [97] demonstrated for the first time that Nd-Fe-B magnets could also be produced by mechanically alloying Nd, Fe and B and annealing the amorphous phase. During the last twenty years mechanical alloying has been widely used in laboratories to prepare a variety of alloy powders because of its versatility. It is performed in a high-energy ball mill, under argon, starting with powders of the constituent elements. When the balls collide, the powder particles are trapped, being heavily deformed and welded. In the beginning, powder with a layered microstructure is produced with non-deformable powder particles embedded in the welded interfaces. In the case of Nd-Fe-B powder, the layered microstructure will be formed of Fe and Nd with the submicron undeformed B particles embedded in the Fe/Nd interfaces [98]. It is necessary

to apply a subsequent heat treatment to form the hard magnetic phase. The reaction begins at relatively low temperatures and takes place with short reaction times at higher temperatures (typically 15-30 min at 700°C), because of the extremely fine distribution of the reactants in the milled material. The magnetically isotropic particles have a very fine microstructure comparable to those obtained by melt-spinning. Mechanically alloyed powders can also be used for hot pressing and subsequent die upsetting (see Section 5.1.4 for more details) [91,99,100].

There is a significant difference between this method and the intensive milling method (used in the present work): in the latter, the hard magnetic compound is already used as the starting material; the powder is produced by milling the homogenised ingot in order to produce amorphous or nanocrystalline alloy.

In the milling process, several factors must be taken into account such as the ball to powder weight ratio, milling time and milling intensity [98].

Subsequent heat treatment of the as-milled powders is necessary in order to reform the $R_2T_{14}B$ hard magnetic phase.

In this work, the starting alloys were crushed to < 250 μm and then milled in a planetary ball mill (Retsch PM4000) using a hardened stainless steel container and 10 mm stainless steel balls. The ball to powder weight ratio was 20:1 with 20 g of material milled at one time, and the angular speed of the mill was chosen to be 300 rpm. The vials were previously sealed under an argon atmosphere. Heat treatment of the as-milled powders was carried out at temperatures between 500 and 800 °C for 30 min under vacuum at pressures lower than 10^{-4} mbar.

The oxygen content of the milled and milled-and-annealed powders was determined with a Leco gas analyser using the hot-extraction method.

5.1.3 Reactive milling in hydrogen

This new process, developed recently [101,102] and used in the present work, tries to marry the advantages of the intensive milling with those of the hydrogenation disproportionation desorption and recombination (HDDR) process by making use of mechanically activated gas-solid reactions.

The HDDR process utilizes a reversible hydrogen induced phase transformation which yields highly coercive NdFeB- and SmFe-type powders, very suitable for the production of both bonded and fully dense hot pressed permanent magnets [103-105]. In the case of $Nd_2Fe_{14}B$, according to equation (5.1) the conventional-HDDR process consists of two stages: firstly, the disproportionation into a finely divided mixture of neodymium hydride, iron and ferroboron typically at 800°C and 10^5 Pa hydrogen and secondly, the desorption at a similar temperature leading to the recombination of the original $Nd_2Fe_{14}B$ phase, but now with a much refined grain size.

$$Nd_2Fe_{14}B + (2 \pm \delta)H_2 \Leftrightarrow 2NdH_{2\pm\delta} + 12Fe + Fe_2B \pm \Delta H \qquad (5.1)$$

The value of δ depends on temperature and hydrogen pressure and ΔH is the reaction enthalpy. The reactive milling technique applied in this work is shown schematically in Fig. 5.1. It is performed in the same way as the intensive milling technique but now argon is substituted by hydrogen at high pressure and the milling is performed at enhanced

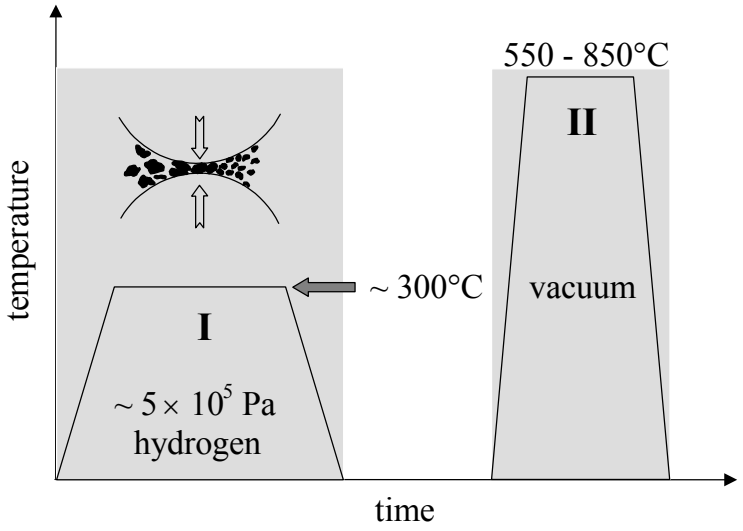

Fig. 5.1: Schematic representation of the reactive milling procedure (I) and the subsequent recombination step in a vacuum furnace (II).

temperature. The milling creates new surfaces to absorb the hydrogen. The energy input via the ball collisions might lead to local temperature peaks providing the kinetics for metal atom diffusion. The result is a very effective hydrogenation and a subsequent disproportionation of thermodynamically very stable compounds due to the high pressure

and the enhanced temperature used during milling [102]. A heat treatment under continuous pumping to desorb the hydrogen leads to the recombined material with grain sizes in the same order to those obtained by melt-spinning or mechanical alloying after optimum heat treatment. Another advantage compared with the intensive milling method is a reduced milling time resulting from the extreme conditions employed.

5.1.4 Hot deformation

The hot deformation process consists of two steps: first, the nanocrystalline flakes or powders are hot pressed to form an isotropic fully dense precursor; second, a die-upsetting procedure is applied resulting in an anisotropic material due to the crystallographic alignment of the *c* axis of the $R_2T_{14}B$ grains parallel to the direction of the pressure applied during the hot deformation [91,106].

Materials produced by melt-spinning and intensive milling were used for hot pressing of precursors with a diameter and height of 8 mm [90-92,99,100]. A hot pressing temperature of 700°C and a pressure of 150 MPa in vacuum (10^{-2} mbar) were sufficient to reach a density of 7.5 gcm^{-3} of the isotropic precursors. Die-upsetting was carried out in argon, at a temperature of 750°C, with a strain rate of 3.3×10^{-3} s^{-1}. For the die-upset magnets a degree of deformation of $\varepsilon \approx 1$ ($\varepsilon = ln(h_0 / h)$, with h_0 the starting height of the sample and h the height after deformation) led to optimum values for the energy density, $(BH)_{max}$. A cube was cut from the center of each die-upset magnet in order to measure the magnetic properties parallel to the pressing direction.

The hot deformation experiments were performed at the IFW by Dr. Kirchner.

5.2 Structural characterisation

5.2.1 Differential scanning calorimetry

Differential scanning calorimetry (DSC) was performed, heating the ribbon flakes and the intensively milled powders up to 700°C or 900°C at a rate of 20 $Kmin^{-1}$ under an argon atmosphere to study the crystallisation behaviour on first heating and magnetic and phase transitions on second heating. Two different devices were used: DSC 7 (Perkin-Elmer) and DSC 404 (Netzsch) with maximum operation temperatures of 800°C and

1500°C, respectively. Alumina and graphite pans were used in the measurements, the latter one presenting the advantage of a higher thermal conductivity and absence of any chemical reaction with the samples under investigation.

5.2.2 X-ray diffraction

A Philips PW 1830 diffractometer with a monochromatic Co-K_α radiation (λ =1.78896 Å) was used for X-ray analysis of the materials after the different processing steps.

The interplanar spacing of the crystal lattice, *d*, corresponding to a family of planes given by the (hkl) Miller indices, can be determined from Bragg's law: $2dsin\theta = n\lambda$, where θ is the angle between the incident beam and (hkl) planes, *n* is an integer and λ is the wavelength of the radiation [107]. All lattice planes with the same *d*-spacing will give rise to reflections at the same Bragg angle, 2θ. The major problem in X-ray analysis is the overlap of different intensity peaks. The most obvious result obtained is the position of the reflections and the subsequent calculation of the *d*-spacings. If the unit cell parameters are known, the Miller indices can be calculated by substituting $d_{(hkl)}=a/\sqrt{(h^2+k^2+l^2)}$ in the Bragg equation. A plot of $sin^2\theta$ vs. *N*, where $N=(h^2+k^2+l^2)$, will result in a straight line with a gradient of $\lambda^2/4a^2$. The lowest gradient for which all the reflections have an integer *N* value provides the Miller indices for the reflections. Several factors which could cause a broadening of the peaks (those due to the measuring instrument: divergence of the beam, natural broadening of the incident radiation, ... and to the material: internal stresses, grain size, for example) must be taken into account.

One of the major causes of peak broadening is finite particle size. As the number of diffracting planes reduces, the width of the line increases. This is analogous to light diffracting from a grating where the line width is proportional to the number of diffracting grooves in the grating. The effect of grain size on the width (in radians) of the diffraction peak is given by the Scherrer's equation:

$$\Delta_{size}(2\theta) = \frac{\kappa\lambda}{D\cos(\theta_B)} \tag{5.1}$$

where $\Delta(2\theta)$ is the width of the peak, λ the wavelength, D the grain size, θ_B the Bragg angle and κ a constant depending on the line shape profile. The constant in equation (5.1) is close to unity ($\kappa = 0.89$ for a Gaussian).

The peak can also be broadened by micro-strains, ε, within the crystal or powder. These strains cause variations in the d-spacing, Δd, and consequently cause a broadening of the diffraction peak. By differentiating Bragg's law it can be shown that strain affects the peak in the following way:

$$\Delta_{strain}(2\theta) = 2\varepsilon \tan(\theta_B) \tag{5.2}$$

Thus, information on grain size and strain can be obtained from the shape of the diffraction peak. The line shape is a convolution of three components: the wavelength dispersion, instrument characteristics and the effects of the sample itself. The intrinsically good wavelength dispersion and instrument characteristics make the two first terms negligible in X-ray experiments.

The Williamson-Hall method [108] considers that both, strain and size effects, occur within the sample resulting in a width of the diffraction peak given by the sum of equations (5.1) and (5.2). The angular dependence difference between the strain and size terms allows to separate them. Rearrangement of that sum gives:

$$\Delta^{hkl}(2\theta)\cos(\theta_B^{hkl}) = \frac{\lambda}{D} + 2\varepsilon \sin(\theta_B^{hkl}) \tag{5.3}$$

A plot of $\Delta^{hkl}(2\theta)\cos(\theta_B^{hkl})$ vs. $\sin(\theta_B^{hkl})$ allows the two broadening terms to be separated and measured. The width of the diffraction peak, $\Delta^{hkl}(2\theta)$, is quantified by using the width at half maximum.

In the present work X-ray diffraction has been used to identify phases matching the experimental data with patterns obtained from single-phase reference samples. These data are collected in a computer program (Philips-APD 3.5). The samples were fixed to a pyrex sample holder using double-sided Scotch tape. The Williamson-Hall method has been used to determine average grain sizes from the XRD patterns.

5.2.3 Electron microscopy

The microstructure of the starting alloys was studied by scanning electron microscopy (SEM) in the backscattering mode. The samples were prepared by standard metallographic means: firstly, they were cut to slices (1-2 mm thick) using a low speed cutting wheel and then embedded in resin and polished on cloth-covered polishing wheels charged with diamond paste on an automatic polishing machine. Polishing of the samples was carried out by the metallographic department at the IFW-Dresden and SEM studies were done using a Zeiss DSM962 microscope.

The nanostructure of processed magnet powders was studied by transmission electron microscopy (TEM) using a JEOL 2000 FX at the Jozef Stefan Institute (Ljubljana, Slovenia). Specimen preparation was done by Dr. Gec by embedding the powder samples in a polymer resin and, afterwards, reducing and polishing the sample by means of ion beam milling. The work at the TEM was carried out in cooperation with Dr. Drazic.

5.3 Characterisation of magnetic properties

5.3.1 Vibrating sample magnetometer

The vibrating-sample method was developed by Foner in 1959. It is based on the flux change in a coil when the sample is vibrated. The sample, situated at the end of a rod, is forced to vibrate in a vertical direction making an oscillatory movement inside the coil system. The oscillating magnetic field of the sample induces an alternating voltage in the detection coils. A small permanent magnet, acting as reference, oscillates at the same frequency as the sample and induces another voltage in two reference coils. The difference of both voltages is proportional to the magnetic moment of the sample.

Milled and annealed powders were mixed with epoxy resin for magnetic characterisation whereas the melt-spun and annealed materials were prepared by bonding about 30 ribbons (5 mm length each one) with every flake parallel to the next one but isolated. Magnetic properties of the different magnets were determined using an Oxford vibrating sample magnetometer (VSM) with a maximum applied field of 8 T at room temperature. The density for each sample was taken as that which corresponds to the

homogenised bulk material determined by the Archimedean principle at room temperature using Iodobutane (C_4HgI) with a density of $\rho \approx 1.6$ gcm^{-3} and a high precision balance.

5.3.2 Curie temperature measurements

Estimation of the Curie temperature, T_C, of the different phases present in the starting alloys and in those after processing was possible simply by heating them in the DSC (1st heating and 2nd heating, respectively) with a rate of 20 Kmin^{-1} under protected atmosphere.

Some T_C values were obtained from thermal demagnetisation curves taken by Dr. Eckert with a self-made VSM, and from curves obtained by thermomagnetic balance measurements by Dr. Roth. The first procedure was used only for some selected alloys, because of the temperature limitation of the device (700^{o}C).

Curie temperature measurements of nanocomposite magnets were carried out in a high temperature susceptometer magnetometer built by Dr. Eckert and Dr. Hinz. Figure 5.2 shows the result of a measurement performed using pure Fe.

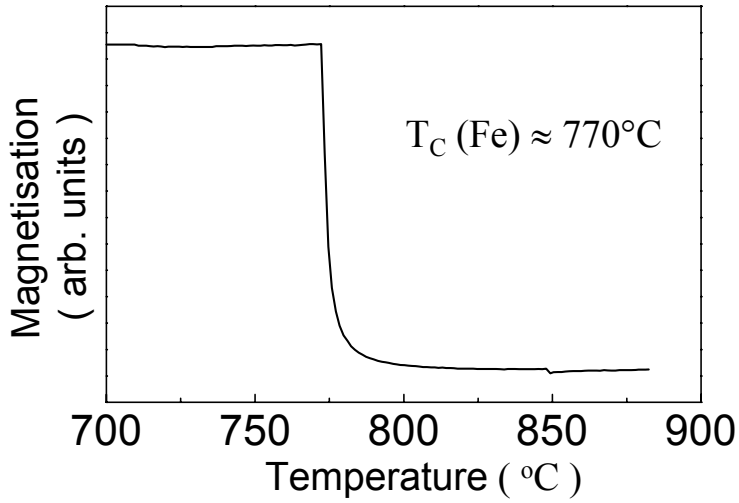

Fig. 5.2: Determination of the Curie temperature of pure Fe by using a high temperature susceptometer magnetometer, showing excellent agreement with the literature value [7].

6 Decoupled magnets: (Nd,Pr)-based magnets

A comparative study of the processing of highly coercive, isotropic (Nd,Pr)FeB-type magnets has been carried out using two different techniques: intensive milling and melt-spinning. The influence of small amounts of additives on microstructure, magnetic properties and processing characteristics is evaluated. Selected samples produced by the two different routes have been used for hot pressing showing significant differences in terms of behaviour during processing and final magnetic properties.

6.1 Thermal characterisation

Thermal characterisation of the materials is very useful to estimate important quantities as for example: crystallisation temperature, T_x, of the $R_2T_{14}B$ phase; Curie temperature, T_C, of the $R_2T_{14}B$ phase and melting temperature, T_m, of the R-rich phase. The corresponding values will be decisive when selecting processing conditions to obtain a magnet with optimised magnetic properties.

6.1.1 Starting alloys

Compositions of the starting alloys are listed in Table 6.1.

Thermal characterisation by first heating of the starting alloys showed two endothermic peaks. The first one corresponds to the Curie temperature, T_C, of the $R_2T_{14}B$ phase and the second one to the melting temperature, T_m, of the R-rich intergranular phase.

alloy no.	Nd (at.%)	Pr (at.%)	Dy (at.%)	Fe (at.%)	B (at.%)	Zr (at.%)
(1)	**14.7**	**-**	**-**	**77.3**	**8.0**	**-**
(2)	15.0	-	1.0	76.0	8.0	-
(3)	14.8	-	1.0	76.0	8.1	0.1
(4)	11.25	3.75	1.0	75.9	8.0	0.1
(5)	7.5	7.5	1.0	75.9	8.0	0.1
(6)	3.75	11.25	1.0	75.9	8.0	0.1
(7)	-	15.0	1.0	75.9	8.0	0.1
(8)	**-**	**14.7**	**-**	**77.3**	**8.0**	**-**

Table 6.1: Composition of the starting alloys (basic ternary alloys in bold).

The ternary NdFeB(1) and PrFeB(8) alloys (see Fig. 6.1a) exhibit values of $T_C \approx 310$ºC and $T_m \approx 675$ºC for the former one, and $T_C \approx 295$ºC and $T_m \approx 655$ºC for the latter one. The evolution of both quantities in dependence on the Pr-content for the additives-containing alloys is shown in Fig. 6.1b. A decrease of T_C with increasing Pr-content and, in addition, a decrease in T_m with values from 676ºC for NdDyFeBZr(3) to 658ºC for PrDyFeBZr(7) is observed. The low Zr content of the samples does not allow to establish marked differences between the T_C values for the $R_2T_{14}B$ phase of the ternary alloys and those corresponding to the additives-containing alloys ((3) and (7), respectively) from the calorimetric data.

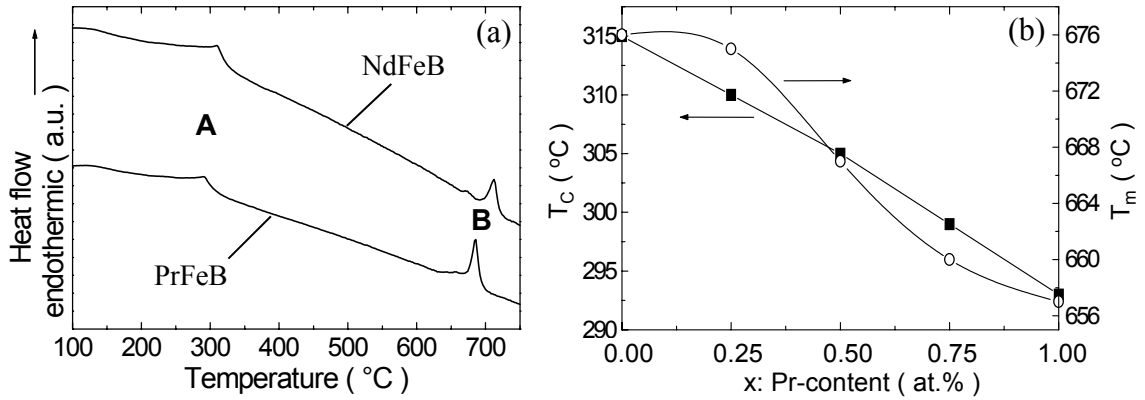

Fig. 6.1: (a) DSC curves on first heating (20 Kmin^{-1}) of the ternary alloys, NdFeB and PrFeB, showing two distinct endothermic peaks: A (T_C) and B (T_m). (b) Evolution of Curie temperature of the $R_2T_{14}B$ phase (squares), T_C , and melting temperature of the R-rich intergranular phase (circles), T_m , in dependence on the Pr-content for the $(Nd_{1-x}Pr_x)_{15}Dy_{1.0}Fe_{75.9}B_{8.0}Zr_{0.1}$ alloys (x = 0 - 1).

6.1.2 Milled and melt-spun alloys

DSC investigations by means of first heating of both milled and melt-spun alloys show two common characteristics related to the crystallisation behaviour (see Fig. 6.2): first, an increase of the onset temperature of crystallisation, T_x, in those samples with Dy and Zr additions by comparison with that of the ternary alloys and, second, a decreased T_x with increasing Pr amount. T_x values for melt-spun alloys show a shift to higher temperatures, i.e. higher stability of the amorphous structure, now with values closer to each other for the different alloys of the series.

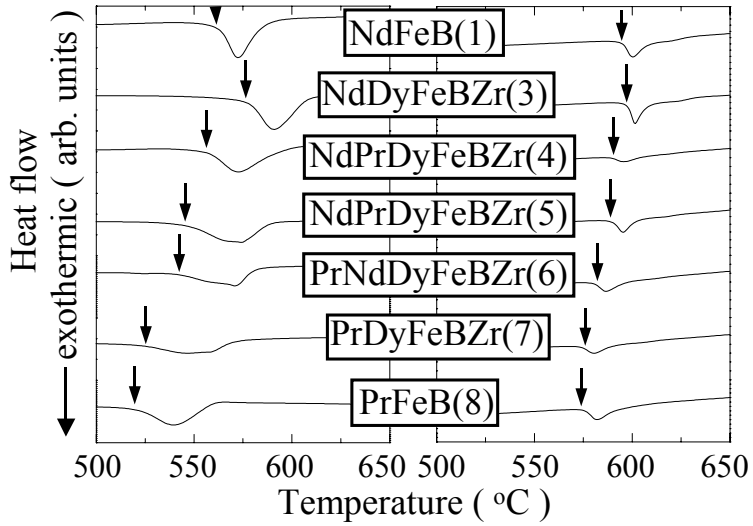

Fig. 6.2: DSC curves on first heating (20 Kmin^{-1}) of the milled powders (left-hand side) and melt-spun materials (right-hand side). Arrows indicate the onset temperature of crystallization, T_x.

In summary, Pr-based alloys show (a) a lower Curie temperatures, (b) a lower melting point of the intergranular phase and (c) a lower crystallisation temperature on annealing milled powders.

6.2 Microstructural characterisation

Heat treatment of either the powders produced by intensive milling or the flakes resulting from melt-spinning leads to the crystallisation of the $R_2T_{14}B$ phase from the amorphous state but with much refined microstructures compared to those of cast alloys. XRD patterns of Fig. 6.3 illustrate the evolution of the microstructure for the ternary PrFeB(8) alloy starting from the as-milled powders and finishing with those after annealing to develop the best combination of magnetic properties. The XRD pattern of the as-milled alloy shows an amorphous halo, reflection peaks of $Pr_{1.1}Fe_4B_4$ and broad peaks related to the nanocrystalline bcc-Fe phase. Annealing at 450ºC for 10 min leads to a reduced intensity of the amorphous halo and slightly narrower reflection peaks of α-Fe. XRD pattern after longer annealing time (450°C / 30 min) does not allow to distinguish any halo of the amorphous phase but reflections peaks of $Pr_{1.1}Fe_4B_4$ and much narrower reflection peaks of α-Fe indicating a significant grain growth of this phase. Crystallisation of the $Pr_2Fe_{14}B$ phase is clearly observed, in good agreement with DSC measurements, after

annealing at 500ºC for 10 min. Reflection peaks of $Pr_{1.1}Fe_4B_4$ are difficult to distinguish at this stage because of the overlapping with those of $Pr_2Fe_{14}B$. Further increased annealing temperatures and/or times lead to the progressive formation and subsequent grain growth of the nanocrystalline $Pr_2Fe_{14}B$ phase accompanied by a reduction in the amount of α-Fe. Optimised annealing conditions (600ºC / 30 min for PrFeB(8)) result in the development of an adequate nanostructure for excellent magnetic properties.

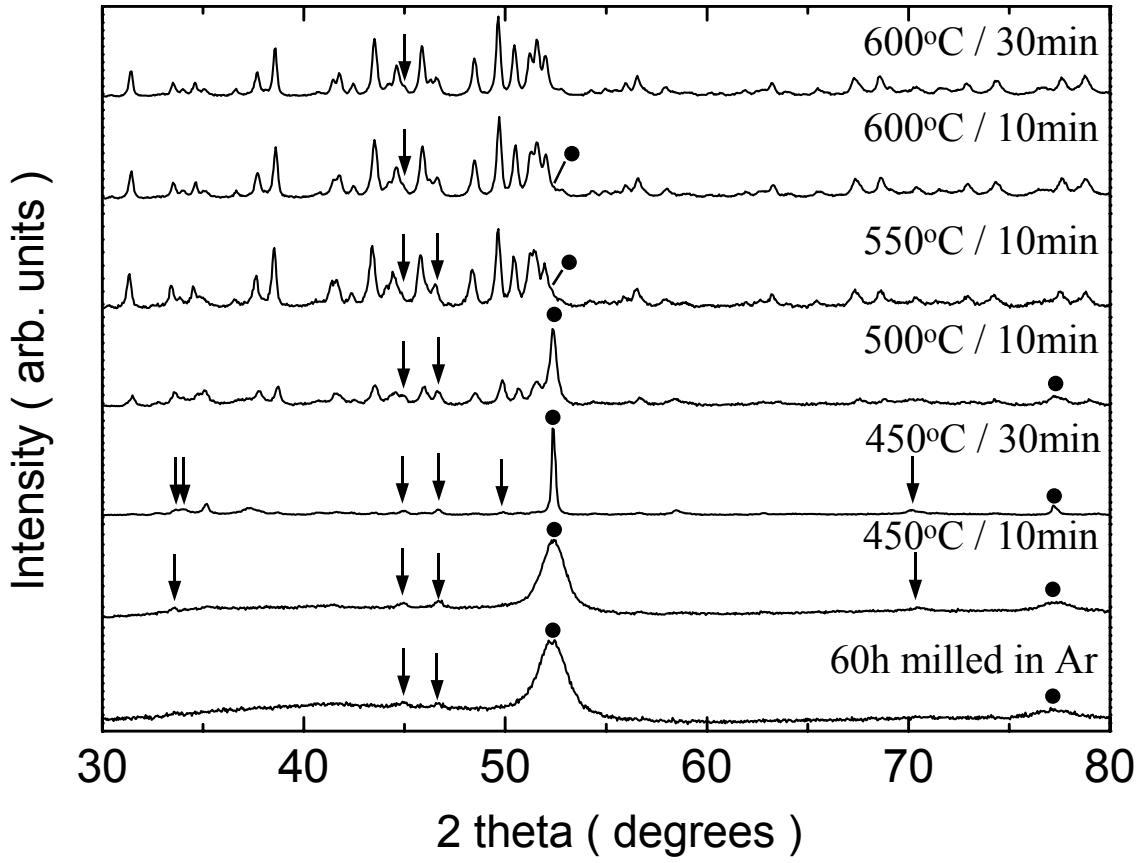

Fig. 6.3: XRD patterns of $Pr_{14.7}Fe_{77.3}B_{8.0}$ (alloy(8)) after different processing steps: milled in argon and milled-and-annealed at different annealing conditions. Markers indicate the main reflection peaks of $R_{1.1}Fe_4B_4$ (arrows) and α-Fe (circles). The non-labelled peaks correspond to the $Pr_2Fe_{14}B$ phase.

TEM studies performed on the ternary NdFeB(1) alloy processed by intensive milling (Fig. 6.4a) and melt-spinning (Fig. 6.4b) allow to see comparable nanostructures after annealing. The TEM micrograph for NdFeB(1) alloy after milling and annealing (Fig. 6.4a) shows a grain size in the range of 50 to 100 nm and small spherical precipitates of α-

Fe of about 2-5 nm within the 2:14:1-type phase. The same material, but now processed by melt-spinning, exhibits extremely fine grains within an amorphous matrix in the as-spun state (inset Fig. 6.4b) and a grain size in the range of 60-100 nm after optimum annealing, with the presence of some Nd rich regions.

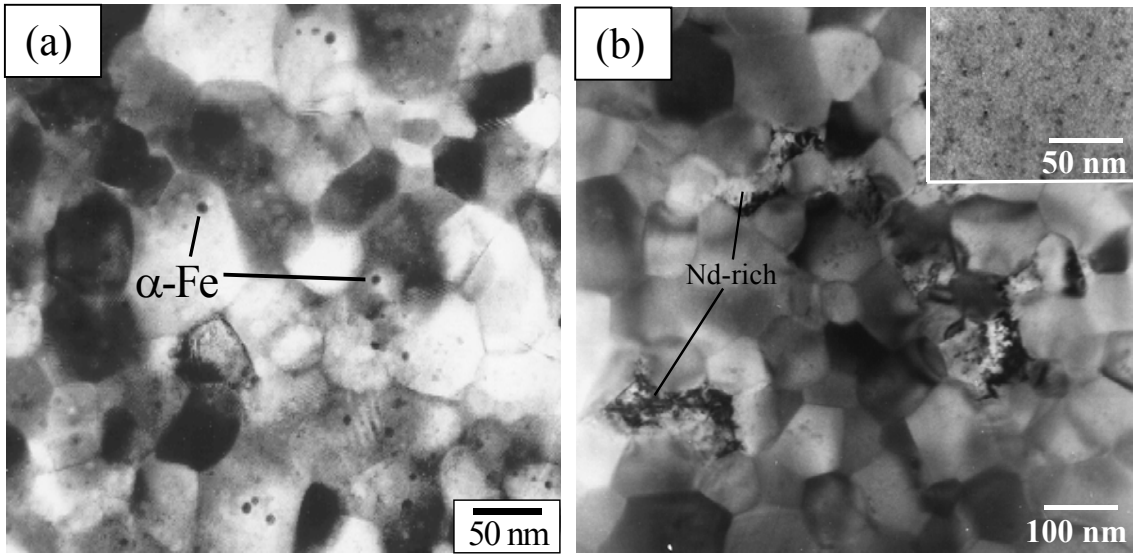

Fig. 6.4: TEM micrographs of $Nd_{14.7}Fe_{77.3}B_{8.0}$ (alloy(1)) after: (a) milling and annealing (600°C / 30 min); (b) melt-spinning and annealing (600°C / 10 min). The small spherical precipitates indicated in (a) correspond to α-Fe. Inset: TEM image showing the partly amorphous microstructure in the as-spun state.

6.3 Characterisation of magnetic properties

6.3.1 Evolution of magnetic properties of milled alloys in dependence on the annealing temperature

The evolution of coercivity when changing the annealing conditions (increasing temperature and/or time) for PrFeB(8) can be seen in Fig. 6.5. The development of the crystalline nanostructure from the initial amorphous state by optimised annealing (see Fig. 6.3) results in improved coercivities.

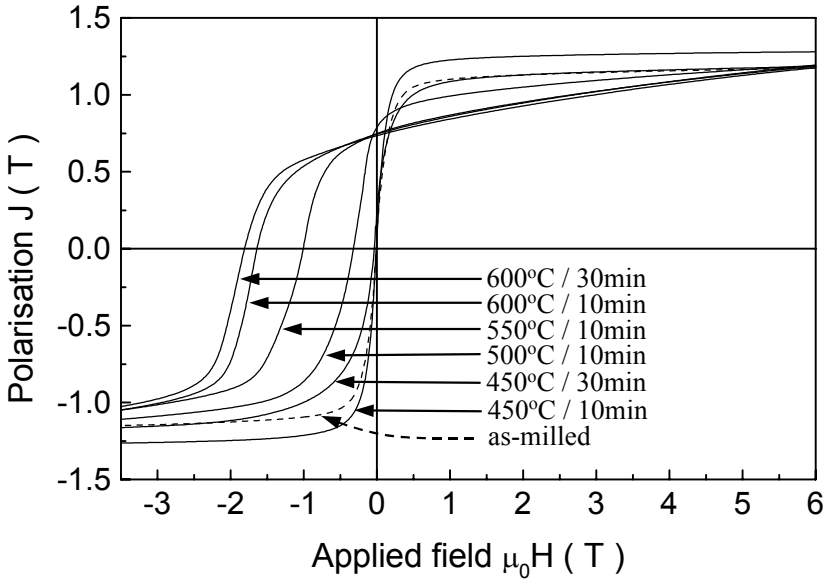

Fig. 6.5: Demagnetisation curves of $Pr_{14.7}Fe_{77.3}B_{8.0}$ (alloy(8)) after different processing steps: milled in argon (dashed line) and milled-and-annealed at different annealing conditions (indicated by arrows).

The evolution of coercivity and remanence with annealing temperature for some alloys of the series can be seen in Fig. 6.6. The Dy- and Zr-containing alloys show higher coercivities than those free of additives (see Fig. 6.6a). This can be attributed to, first, the higher anisotropy field associated with $Dy_2Fe_{14}B$ and, second, the grain-growth-inhibiting effect of the Zr addition. The result is a high value of $\mu_0 H_c$ = 2.47 T for NdDyFeBZr(3) whereas only 1.75 T for the ternary NdFeB(1) alloy, both of them annealed at 700ºC. The combined effect of both additions is especially evident for high annealing temperatures such as 800ºC. Figure 6.7 shows the TEM micrograph of the former exhibiting a more homogeneous nanostructure by comparison with that of NdFeB(1) (see Fig. 6.4a). The Dy addition results in a reduction of the saturation polarisation and, consequently, of the remanence (Fig. 6.6b) because of the anti-parallel coupling of the Dy and Fe magnetic moments which can be seen from a comparison of the corresponding remanence values for the NdFeB(1) and NdDyFeB(2) alloys: 0.73 T and 0.68 T, respectively, after annealing at 600°C. Again, the stabilisation against grain growth due to the Zr addition has a beneficial effect, avoiding a decrease in the remanence at high annealing temperatures which is observed for the NdFeB(1) and NdDyFeB(2) alloys (see Fig. 6.6b). Another feature of the Zr-containing alloys is the small variation in coercivity and remanence values observed

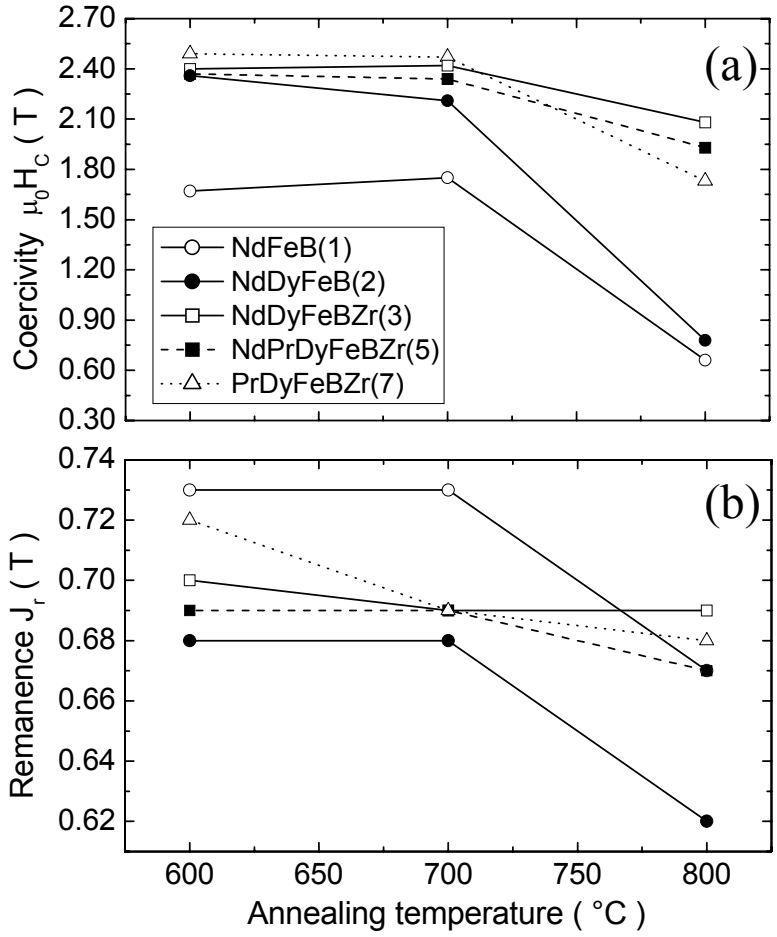

Fig. 6.6: Magnetic properties of milled-and-annealed powders after annealing at different temperatures: (a) coercivity $\mu_0 H_c$ and (b) remanence J_r.

when varying the annealing temperature. For example, when changing the annealing temperature from 600 to 800 °C a maximum difference in the coercivity values of 1 T for the NdFeB(1) alloy was observed, but only 0.1 T for the NdDyFeBZr(3) alloy, indicating a wider processing window for these Zr-containing alloys due to the inhibited grain growth. A similar effect can be found for the Pr-based alloys, with the highest coercivity, $\mu_0 H_c$ = 2.49 T, achieved for PrDyFeBZr(7) after annealing at 600°C due, in addition, to the higher anisotropy field associated with $Pr_2Fe_{14}B$.

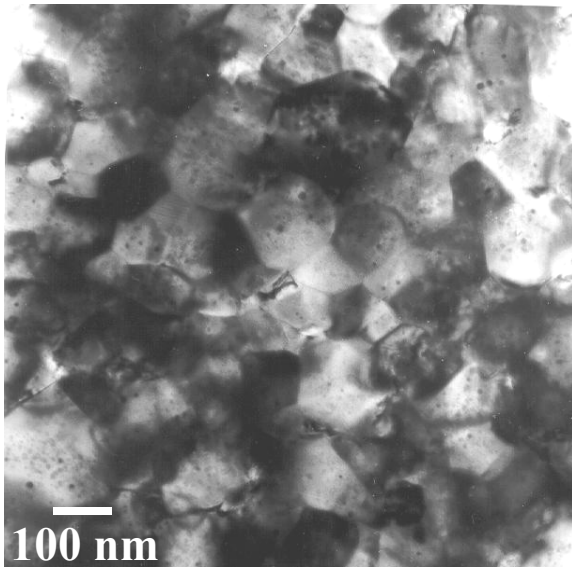

Fig. 6.7: TEM micrograph of milled $Nd_{14.8}Dy_{1.0}Fe_{76.0}B_{8.1}Zr_{0.1}$ (alloy(3)) after annealing (600ºC / 30 min).

6.3.2 Influence of additives and Pr-content on coercivity in alloys processed by milling and melt-spinning

The high coercivities obtained for PrDyFeBZr(7) in comparison with those obtained for PrFeB(8) processed by either intensive milling or melt-spinning (Fig. 6.8) illustrate the role played by the additives. They modify both the intrinsic properties and the microstructure (Fig. 6.9), and thus the extrinsic magnetic properties.

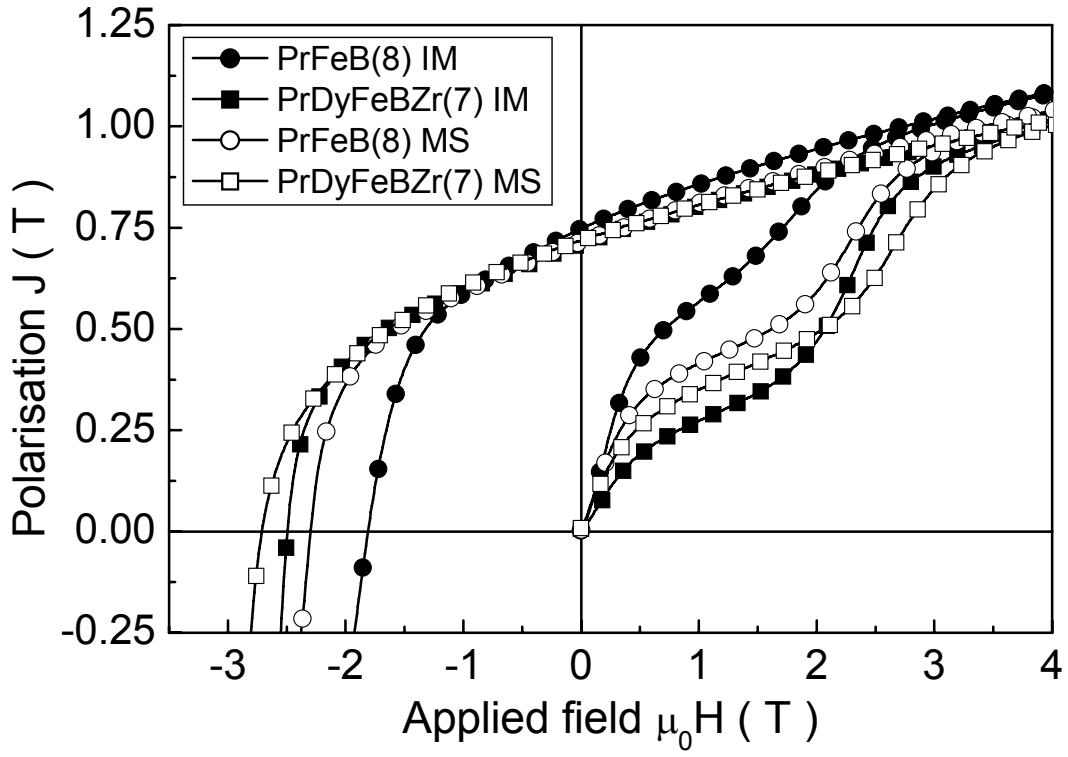

Fig. 6.8: Initial magnetisation and demagnetisation curves of $Pr_{14.7}Fe_{77.3}B_{8.0}$ (alloy (8)) and $Pr_{15.0}Dy_{1.0}Fe_{75.9}B_{8.0}Zr_{0.1}$ (alloy (7)) processed by intensive milling (IM) and melt-spinning (MS) after annealing: 600ºC for 30 and 10 min, respectively.

A TEM micrograph of the milled and annealed ternary alloy shows large platelets formed during crystallisation (see Fig. 6.9a). This is in contrast to the equiaxial grains and the finer and more homogeneous microstructure obtained after melt-spinning and annealing (Fig. 6.9c). The micrographs corresponding to PrDyFeBZr(7) show, in both cases, comparable microstructures with grain sizes in the range of 70-100 nm, but more uniform for the one processed by melt-spinning (Figs. 6.9b,d).

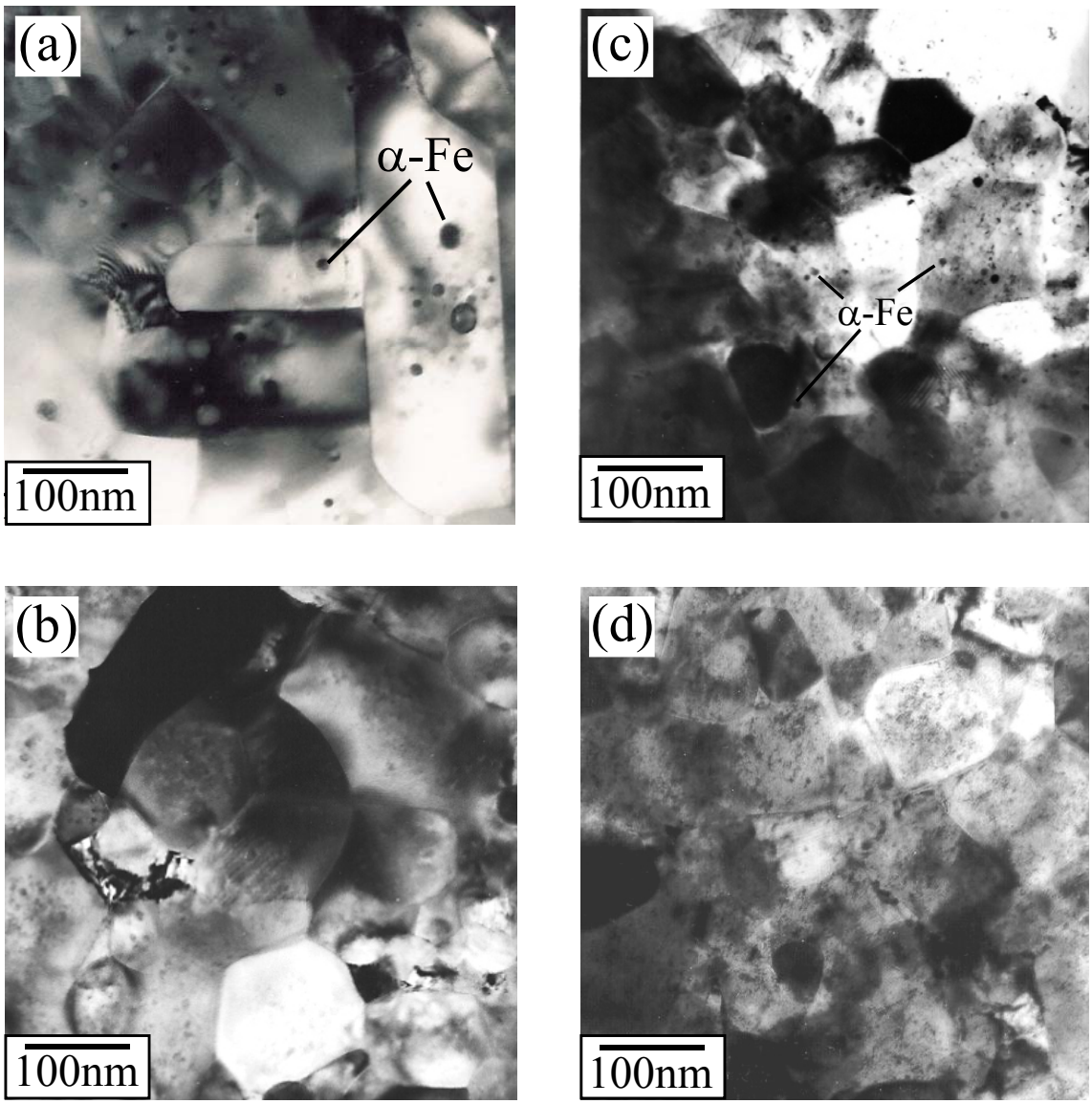

Fig. 6.9: TEM images of $Pr_{14.7}Fe_{77.3}B_{8.0}$ (alloy (8)) and $Pr_{15.0}Dy_{1.0}Fe_{75.9}B_{8.0}Zr_{0.1}$ (alloy (7)) processed by intensive milling ((a) and (b), respectively) and melt-spinning ((c) and (d), respectively), all of them after annealing: 600°C for 30 and 10 min, respectively.

A comparison of the optimum coercivities achieved for the additives-containing alloys processed by the two different techniques can be seen in Fig. 6.10. Higher values can be observed for the melt-spun and annealed materials along the whole series.

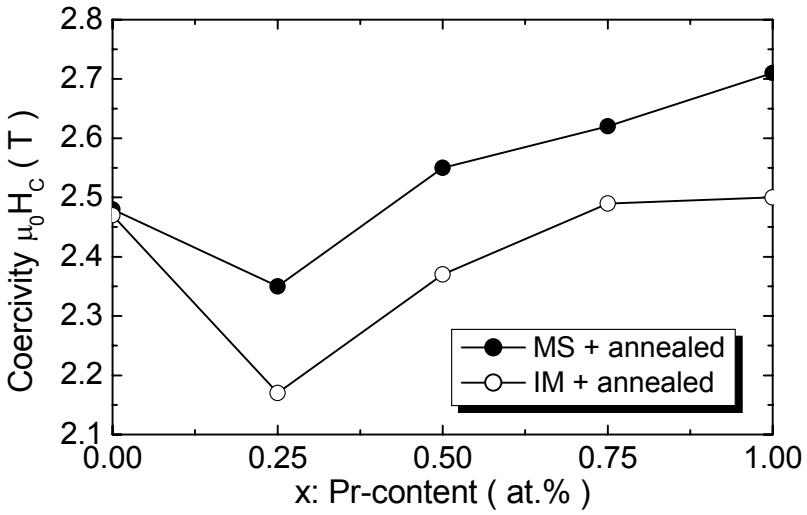

Fig. 6.10: Evolution of coercivities of annealed $(Nd_{1-x}Pr_x)_{15}Dy_{1.0}Fe_{75.9}B_{8.0}Zr_{0.1}$ alloys in dependence on Pr-content (x = 0 to 1) processed by two different routes: intensive milling (IM) and melt-spinning (MS).

6.4 Hot workability

Hot-pressing and hot-deformation were performed using (a) intensively milled powders with starting particles sizes lower than 160 μm and (b) powderised melt-spun flakes. Figure 6.11 shows the demagnetisation curves of the milled and annealed powders as well as those of milled, hot pressed and die-upset magnets. The grain growth inhibiting effect of Zr can be observed by comparison of the coercivities of the milled and annealed powders and those of the corresponding die-upset magnets. $Nd_{14.8}Dy_{1.0}Fe_{76.0}B_{8.1}Zr_{0.1}$ (alloy (3)) exhibits a decrease in coercivity after hot deformation of only 17% whereas a 64% decrease is observed for $Nd_{14.7}Fe_{77.3}B_{8.0}$ (alloy (1)). Both die-upset magnets show the same remanence, resulting in energy densities of $(BH)_{max}$ = 183 kJm^{-3} and 163 kJm^{-3}, respectively. However, $Pr_{14.7}Fe_{77.3}B_{8.0}$ (alloy (8)) textured by die-upsetting exhibits magnetic properties as high as J_r = 1.27 T, $\mu_0 H_c$ = 1.20 T and $(BH)_{max}$ = 307 kJm^{-3}. The higher coercivity could be explained in terms of the different morphology and distribution of the intergranular phase. Fuerst *et al* [90] proposed that differences in the transport properties of Nd and Pr atoms during cooling from the die-upset temperature could lead to a higher volume fraction of Pr-rich phase which would be responsible for the high coercivity. The high remanence of the Pr-based alloys could be explained by the lowest deformation stress [93] required for texturing (as low as 5 MPa) in contrast to the 25 MPa

necessary for NdFeB(1). Figure 6.12 compares the deformation stresses for $Pr_{14.7}Fe_{77.3}B_{8.0}$ and two commercially available materials: MQP-A ($Nd_{14.0}Fe_{81.1}B_{4.9}$) and MQU-F ($Nd_{13.6}Fe_{73.6}Ga_{0.6}Co_{6.6}B_{5.6}$). The lower remanence after die-upsetting of the melt-spun $Pr_{14.8}Dy_{1.0}Fe_{76.0}B_{8.1}Zr_{0.1}$ (alloy (7)) could be attributed to the high required deformation stress of about 40 MPa and to the reduction of the saturation polarisation of the alloy due to alloy additions.

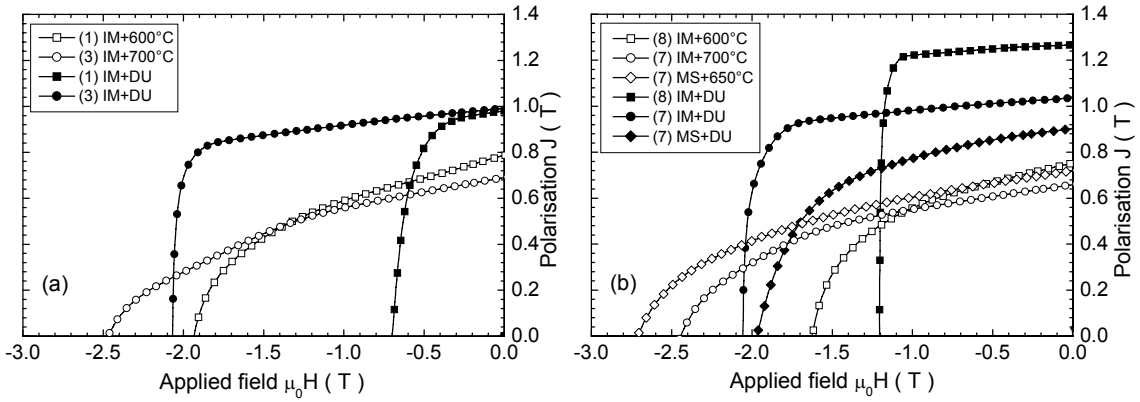

Fig. 6.11: Demagnetisation curves of magnets after milling (IM) and annealing and melt-spinning (MS) and annealing (empty symbols), and demagnetisation curves measured along the texture axis of the die-upset (DU) magnets (full symbols), corresponding to: (a) $Nd_{14.7}Fe_{77.3}B_{8.0}$ (alloy (1)) and $Nd_{14.8}Dy_{1.0}Fe_{76.0}B_{8.1}Zr_{0.1}$ (alloy (3)), (b) $Pr_{14.7}Fe_{77.3}B_{8.0}$ (alloy (8)) and $Pr_{14.8}Dy_{1.0}Fe_{76.0}B_{8.1}Zr_{0.1}$ (alloy (7)).

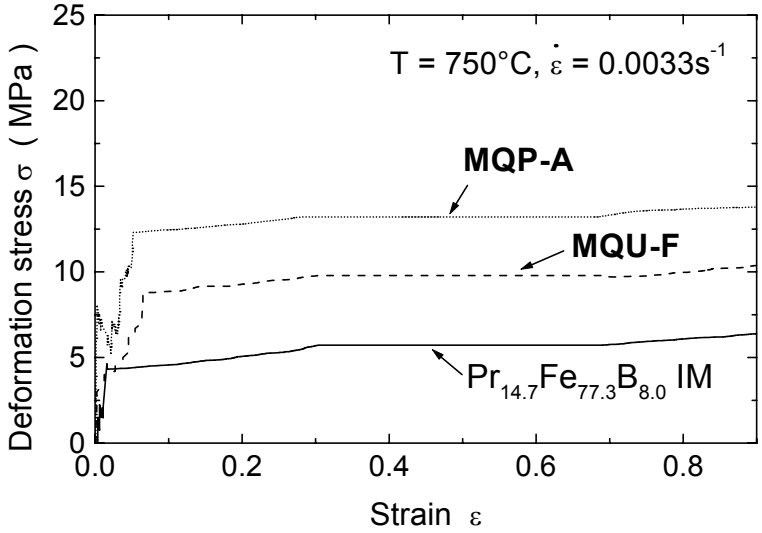

Fig. 6.12: Stress-strain curves and deformation stresses required for texturing by hot deformation for intensively milled $Pr_{14.7}Fe_{77.3}B_{8.0}$ powders, MQP-A ($Nd_{14.0}Fe_{81.1}B_{4.9}$) and MQU-F ($Nd_{13.6}Fe_{73.6}Ga_{0.6}Co_{6.6}B_{5.6}$). Die-upsetting carried out in argon, at a temperature of 750°C with a strain rate of 3.3×10^{-3} s^{-1}.

Figure 6.13 shows a Kerr image of die-upset intensively milled PrFeB(8). It can be seen by comparison with Fig. 2.5 how the interaction between the domains takes place on a more reduced scale than in the case of conventional die-upset melt-spun NdFeB. Actually, this is the first image of interaction domains of die-upset milled powders. A cooperative phenomenon leads to domain patterns on a scale much larger than the actual grain size.

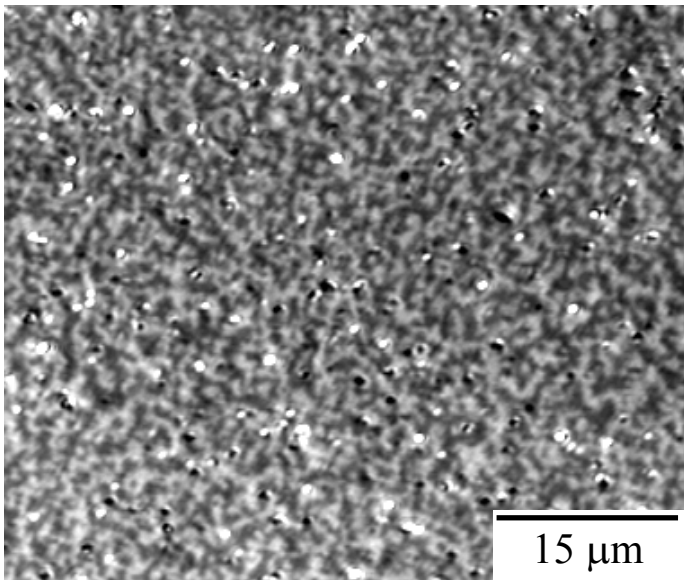

Fig. 6.13: Kerr image showing interaction domains in a die-upset intensively milled $Pr_{14.7}Fe_{77.3}B_{8.0}$ (alloy (8)), with the c-axis perpendicular to the imaging plane (courtesy O. Gutfleisch).

6.5 Summary

(Nd,Pr)FeB-type alloys have been prepared by intensive milling and melt-spinning resulting in isotropic powders with very good coercivities. Dy and Zr additions increase the onset temperature of the crystallization of the $R_2Fe_{14}B$ phase, i.e. they stabilize the amorphous structure. On the other hand, the substitution of Nd by Pr decreases the onset thereby allowing the application of lower annealing temperatures. The high coercivity exhibited by the powders containing Dy and Zr can be explained by the high anisotropy field associated with Dy and, secondly, by the grain growth inhibiting effect of the Zr addition. In this way, alloys containing these additives to the base composition show high coercivity values after annealing at 600-800 °C and even after die-upsetting. An additional

advantage of the Pr-containing alloys is the low deformation force necessary for texturing by hot deformation, with the lowest value obtained for the milled PrFeB ternary alloy.

7 Nanocomposite magnets: PrNdDyFeCoBZr + x wt.% α-Fe (x = 5 - 35)

In the previous section, the influence of Dy and Zr and the substitution of Pr by Nd on the microstructural and magnetic properties have been studied. Substitution of Pr by Nd leads to a decrease in coercivity but an increase in remanence, resulting in a higher value of $(BH)_{max}$. The best combination of magnetic properties was achieved for $Pr_{11.25}Nd_{3.75}Dy_{1.0}Fe_{76.0}B_{8.1}Zr_{0.1}$ (alloy (6)) with: $(BH)_{max}$ = 92 kJm^{-3}. This decoupled magnet exhibits a very high coercivity of $\mu_0 H_c$ = 2.49 T. Practical applications of bonded magnets do not require such a high coercivity. A decreased R-content is expected to result in a decreased coercivity but enlarged remanence, i.e. increased $(BH)_{max}$. This latter value can be further enlarged by means of an effective exchange-coupling. These aspects will be considered along this chapter.

7.1 Characterisation of the base alloy: $Pr_{9.0}Nd_{3.0}Dy_{1.0}Fe_{72.0}Co_{8.0}B_{6.9}Zr_{0.1}$

Since the best combination of magnetic properties was obtained for the decoupled magnet with composition $Pr_{11.25}Nd_{3.75}Dy_{1.0}Fe_{76.0}B_{8.1}Zr_{0.1}$ (alloy (6)), the Dy and Zr contents and the Pr:Nd ratio have remained unchanged in the new alloy: $Pr_{9.0}Nd_{3.0}Dy_{1.0}Fe_{72.0}Co_{8.0}B_{6.9}Zr_{0.1}$. A small amount of Fe has been substituted by Co to improve the relatively low Curie temperature of the $R_2T_{14}B$ phase.

7.1.1 DSC and thermomagnetic analysis of starting and milled material

The DSC analysis performed on the starting material shows two endothermic peaks: the first one corresponding to the Curie temperature of the $R_2T_{14}B$ phase and the second one to the melting-point of the R-rich phase (see Fig. 7.1a). An increased value of $T_C \approx$ 390°C due to the presence of Co and a much reduced melting-point of the R-rich phase ($T_m \approx$ 580°C) are significant advantages by comparison with the previously studied alloys. Additionally, a reduced crystallisation temperature of $T_x \approx$ 520°C is observed on first heating of the milled powders (Fig. 7.1b). Thermomagnetic measurements on milled and

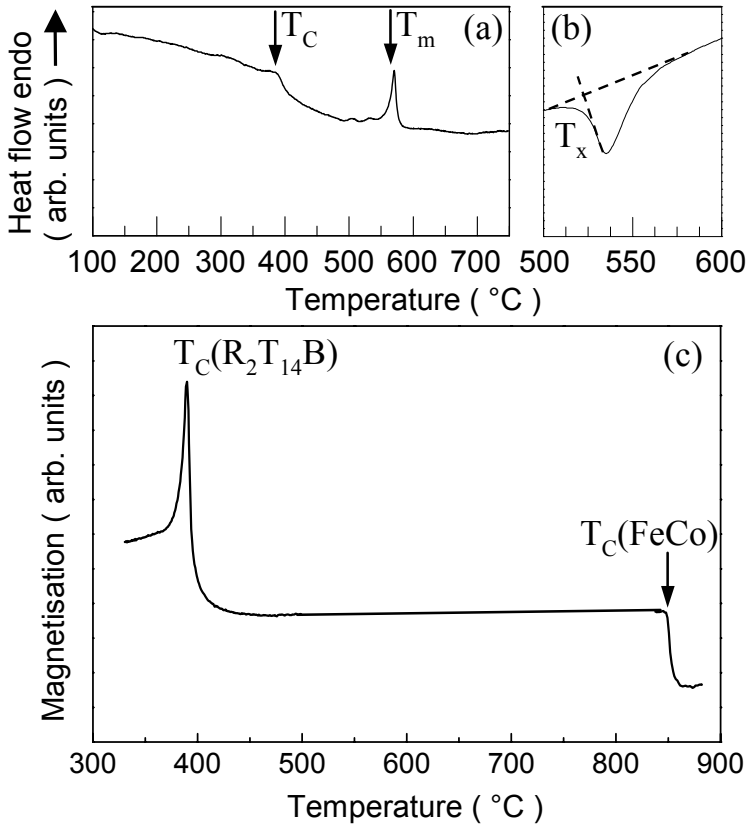

Fig. 7.1: Top: DSC curves on first heating (20 Kmin^{-1}) of the $Pr_{9.0}Nd_{3.0}Dy_{1.0}Fe_{72.0}Co_{8.0}B_{6.9}Zr_{0.1}$ alloy at different stages: (a) starting material (arrows indicating $T_C(R_2T_{14}B)$ and T_m, melting temperature of the R-rich phase); (b) milled powder (T_x: onset temperature of the crystallisation). Bottom: Thermomagnetic measurement of the same alloy after milling and annealing at 600°C, indicating the Curie temperature of the hard and soft magnetic phases (applied field during measurement: $\mu_0 H_{appl} \approx 0.02$ T).

annealed $Pr_{9.0}Nd_{3.0}Dy_{1.0}Fe_{72.0}Co_{8.0}B_{6.9}Zr_{0.1}$ show two different signals: the first one indicative of the Curie temperature of the hard magnetic phase, $T_C \approx 385$°C, and the second one at higher values, corresponding to that of a soft magnetic phase, $T_C \approx 850$°C (Fig. 7.1c). The presence of this soft magnetic phase is attributed to a decreased R-content in the resulting powders maybe due to evaporation during milling and subsequent annealing. The corresponding T_C value of this phase exceeds the T_C of pure Fe by 80°C. This is attributed to a diffusional redistribution of Co and Fe during the crystallisation process which would result in a reduction of the Co-content in the hard magnetic phase and a formation of an FeCo soft magnetic phase. A similar observation was made previously by Neu [109].

7.1.2 Microstructural characterisation

Co has been found to play an important role as a grain refiner of the microstructure in this system [110] as it can be seen from a comparison of the broadness of the reflection peaks in the corresponding XRD patterns with those of PrNdDyFeBZr(6) (see Fig. 7.2). Even after annealing at 700°C the peaks still remain significantly broad. A very homogeneous nanostructure with grains of about 20-25 nm was observed by TEM after annealing at 600ºC as it can be seen in Fig. 7.3. A reflection peak corresponding to the α-(Fe,Co) phase can be observed in the XRD patterns at about 52° which disappears after annealing at temperatures higher than 700°C due to the solution of this phase into the $R_2T_{14}B$ phase.

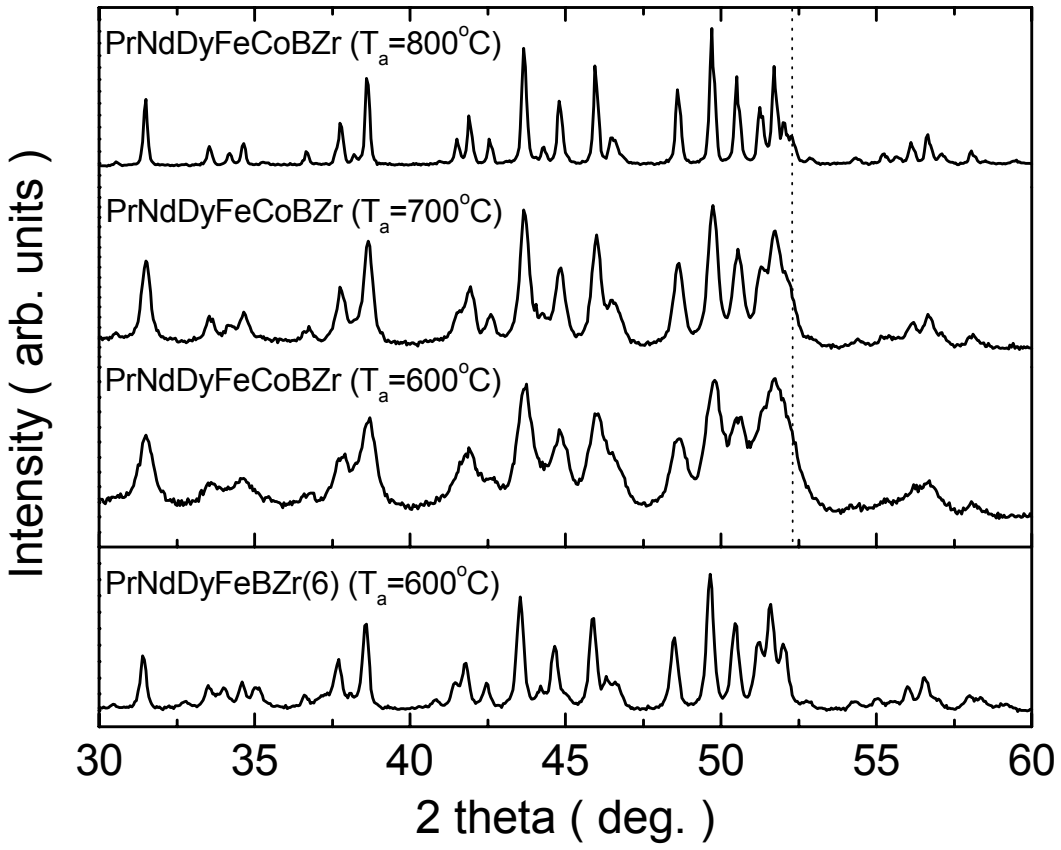

Fig. 7.2: XRD patterns of milled $Pr_{11.25}Nd_{3.75}Dy_{1.0}Fe_{75.9}B_{8.0}Zr_{0.1}$ (alloy (6)) and $Pr_{9.0}Nd_{3.0}Dy_{1.0}Fe_{72.0}Co_{8.0}B_{6.9}Zr_{0.1}$ alloys after subsequent annealing for 30min (annealing temperatures in brackets). The dotted line indicates the reflection peak at about 52° of the α-(Fe,Co) phase.

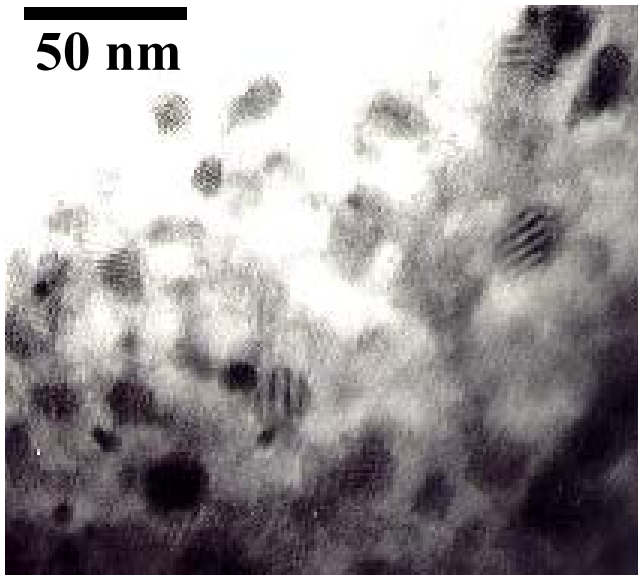

Fig. 7.3: TEM micrograph of milled $Pr_{9.0}Nd_{3.0}Dy_{1.0}Fe_{72.0}Co_{8.0}B_{6.9}Zr_{0.1}$ after annealing at 600°C.

7.1.3. Characterisation of magnetic properties

As-milled and annealed $Pr_{11.25}Nd_{3.75}Dy_{1.0}Fe_{75.9}B_{8.0}Zr_{0.1}$ (alloy(6)) exhibits the best combination of magnetic properties of the series previously studied resulting in the highest energy density: $(BH)_{max}$ = 92 kJm^{-3}. It is because of this that the Dy and Zr contents and the Pr:Nd ratio remained unchanged for $Pr_{9.0}Nd_{3.0}Dy_{1.0}Fe_{72.0}Co_{8.0}B_{6.9}Zr_{0.1}$ but the total R-content was reduced in order to increase the remanence. Figure 7.4 shows the initial magnetisation and demagnetisation curves for both alloys after optimum annealing conditions. The evolution of remanence and coercivity with increasing annealing temperature for PrNdDyFeCoBZr can be seen in the inset of Fig. 7.4: the increase in coercivity is accompanied by a decrease in remanence due to the grain growth effect and the complete dissolution of the soft magnetic phase with increasing annealing temperature. This makes necessary to achieve a balance between them to avoid a detriment of the magnetic performance ($(BH)_{max}$). A significant remanence enhancement, J_r = 0.92 T, and a still high coercivity, $\mu_0 H_c$ = 1.25 T, were obtained after annealing at 600°C. The high remanence results from the very fine and homogeneous nanostructure which leads to an effective exchange-coupling between the grains. A good square shape of the hysteresis loop is also obtained, resulting in a high $(BH)_{max}$ value of 140 kJm^{-3}.

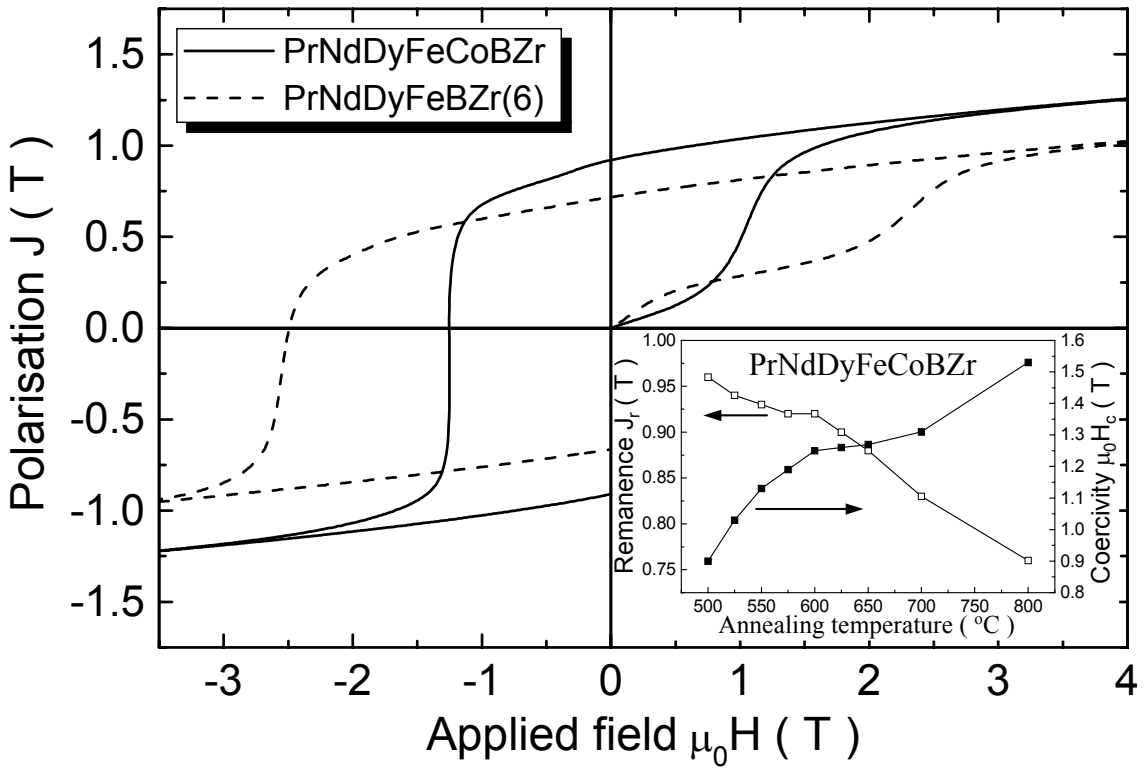

Fig. 7.4: Initial magnetisation and demagnetisation curves of milled and annealed $Pr_{11.25}Nd_{3.75}Dy_{1.0}Fe_{75.9}B_{8.0}Zr_{0.1}$ (alloy (6)) and $Pr_{9.0}Nd_{3.0}Dy_{1.0}Fe_{72.0}Co_{8.0}B_{6.9}Zr_{0.1}$ powders. Inset: Evolution of remanence, J_r, and coercivity, $\mu_0 H_c$, in dependence on annealing temperature for the latter alloy.

7.2 Characterisation of the base alloy blended with α-Fe:

PrNdDyFeCoBZr + x wt.% α-Fe (x = 5 - 35)

In this section, intensive milling will be shown to be a very versatile technique to obtain high-quality isotropic nanocomposite powders by blending the previously studied $Pr_{9.0}Nd_{3.0}Dy_{1.0}Fe_{72.0}Co_{8.0}B_{6.9}Zr_{0.1}$ starting alloy with elementary α-Fe powders as soft magnetic phase.

7.2.1 Compositional analysis

The $Pr_{9.0}Nd_{3.0}Dy_{1.0}Fe_{72.0}Co_{8.0}B_{6.9}Zr_{0.1}$ alloy was milled with different fractions of pure α-Fe powder (x = 5 – 35 wt.%). XRD patterns of the resulting powders after milling and annealing show, first, an increase of the intensity peak of the soft magnetic phase with

increasing α-Fe fraction and, second, very broad reflection peaks for both the hard and the soft magnetic phases (see Fig. 7.5).

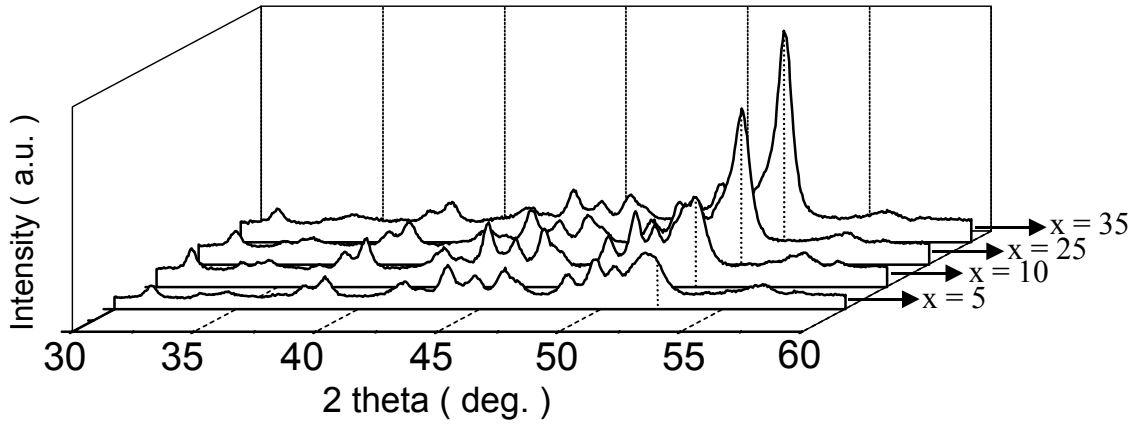

Fig. 7.5: XRD patterns of $Pr_{9.0}Nd_{3.0}Dy_{1.0}Fe_{72.0}Co_{8.0}B_{6.9}Zr_{0.1}$ + x wt.% α-Fe (x = 5, 10, 25 and 35) after milling-and-annealing. The dotted line indicates the reflection peak of the (Fe,Co)-phase at about 52°.

7.2.2 Magnetic behaviour

(i) Hysteresis loops

Figure 7.6 shows the decreased coercivity but enhanced remanence with increasing α-Fe content. Magnetically single-phase behaviour is observed in all cases indicative of an effective exchange-coupling between the hard and the soft magnetic phases due to a very fine nanostructure.

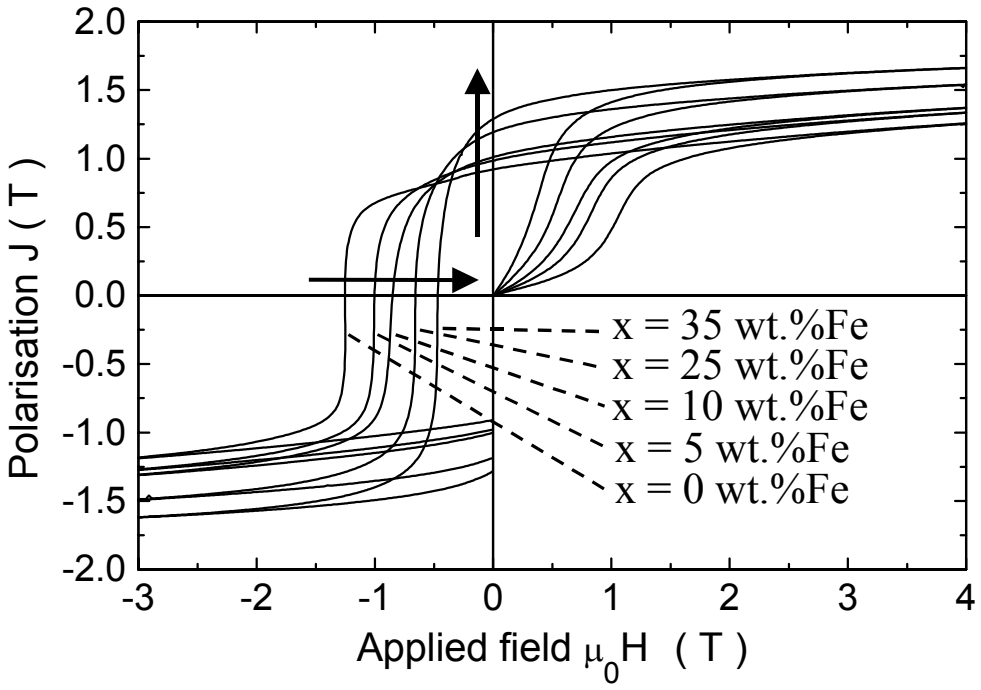

Fig. 7.6: Initial magnetisation and demagnetisation curves for $Pr_{9.0}Nd_{3.0}Dy_{1.0}Fe_{72.0}Co_{8.0}B_{6.9}Zr_{0.1}$ + x wt.% α-Fe (x = 0, 5, 10, 25 and 35) after milling and annealing. Arrows indicate the evolution of remanence and coercivity with increasing α-Fe fraction.

(ii) Evolution of magnetic properties vs. α-Fe-fraction

It is generally accepted that a small grain size improves both the remanence and the coercivity of isotropic nanocomposite magnets. However, according to theoretical models [31-36], too small soft magnetic grains (smaller than twice the domain wall width of the hard phase) can result in a coupling between the hard magnetic grains, i.e. in a low coercivity [64-66]. Figure 7.7 shows the evolution of the magnetic properties in dependence on the α-Fe fraction for the complete series after annealing to achieve the highest $(BH)_{max}$ values. The high remanences are due to the presence of α-Fe and the exchange-coupling effect. It can be seen how J_r is improved at the expense of coercivity. The maximum value for the maximum energy density is achieved for an α-Fe fraction of 25 wt.% α-Fe: $(BH)_{max}$ = 178 kJm^{-3}. For x ≤ 25 wt.% α-Fe the coercive field is higher than one half of the remanence, i.e. $(BH)_{max}$ is mainly controlled by the remanence resulting in an increase of $(BH)_{max}$ with increasing J_r . At higher α-Fe contents however, the coercive field is smaller than one half of the remanence and $(BH)_{max}$ decreases as a consequence of

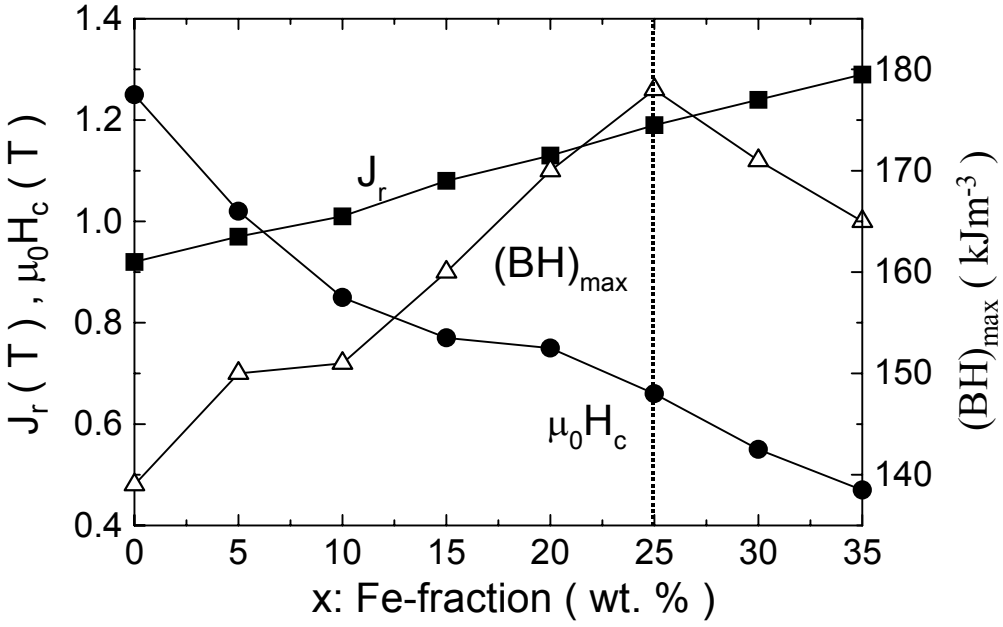

Fig. 7.7: Evolution of remanence, J_r (T); coercivity, $\mu_0 H_c$ (T); and energy product, $(BH)_{max}$ (kJm^{-3}) in dependence on the α-Fe fraction (wt.%). Dotted line indicates the α-Fe fraction which leads to the best combination of magnetic properties: x = 25wt.% α-Fe.

irreversible demagnetisation processes. The TEM bright field image of milled and optimally annealed PrNdDyFeCoBZr + 25 wt.% α-Fe powder shown in Fig. 7.8 allows to distinguish grains of about 20 nm corresponding to the hard magnetic phase and some smaller ones, of about 15 nm, corresponding to the soft magnetic phase. A relative remanence $\alpha' = 0.73$ (with $\alpha' = J_r / J(8T)$) is obtained for this sample.

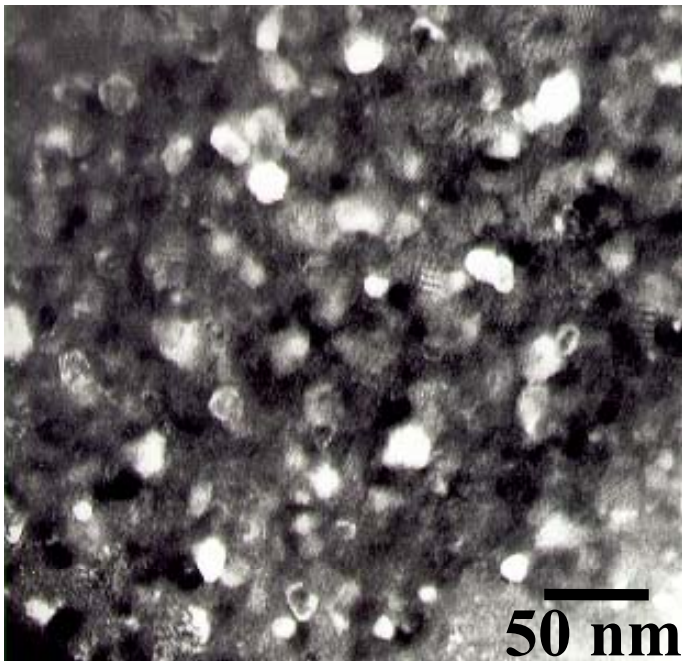

Fig. 7.8: TEM bright field image of $Pr_{9.0}Nd_{3.0}Dy_{1.0}Fe_{72.0}Co_{8.0}B_{6.9}Zr_{0.1}$ + 25wt.% α-Fe powder after milling and annealing at 600°C.

(iii) Thermomagnetic results

Thermomagnetic measurements on $Pr_{9.0}Nd_{3.0}Dy_{1.0}Fe_{72.0}Co_{8.0}B_{6.9}Zr_{0.1}$ + 25 wt.% α-Fe, after milling and annealing, shows a Curie temperature of the hard magnetic phase of about 365°C, and $T_C \approx 830$°C for the α-(Fe,Co) soft magnetic phase (see Fig. 7.9). This is attributed to a diffusional redistribution of Co and Fe during the crystallisation process and, due to the complete solubility of Co in the $R_2T_{14}B$ and α-Fe phases, this would result in a reduction of the Co-content in the hard magnetic phase and the formation of an α-FeCo soft magnetic phase. The solubility of Co in the $R_2T_{14}B$ and α-Fe phases during the crystallisation process can explain the reduction of T_C for the hard and the soft magnetic phases by comparison with the values obtained for the pure PrNdDyFeCoBZr milled without any Fe addition. The higher amount of α-Fe in the sample results in a higher dilution of Co in both phases giving rise to a reduction in the corresponding T_C values.

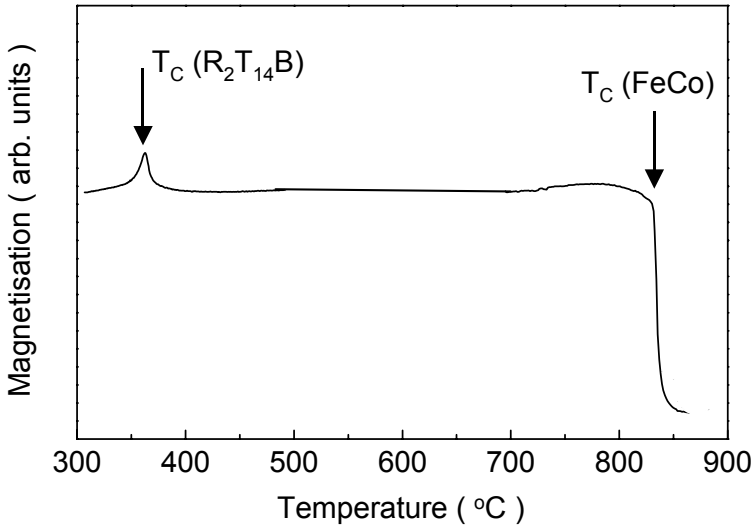

Fig. 7.9: Thermomagnetic measurement of $Pr_{9.0}Nd_{3.0}Dy_{1.0}Fe_{72.0}Co_{8.0}B_{6.9}Zr_{0.1}$ + 25wt.% α-Fe powder after milling and annealing at 600ºC, indicating the Curie temperatures of the hard and the soft magnetic phases (applied field during measurement: $\mu_0 H_{appl} \approx 0.02$ T).

7.3 Summary

This chapter has focused on studying high-quality nanocomposite Pr-based magnets produced from a $Pr_9Nd_3Dy_1Fe_{72}Co_8B_{6.9}Zr_{0.1}$ alloy blended with different fractions of α-Fe powder previous to milling. The starting alloy exhibits promising magnetic properties after milling and annealing: J_r = 0.92 T, $\mu_0 H_c$ = 1.25 T and $(BH)_{max}$ = 140 kJm^{-3}, due to a very fine microstructure with a mean grain size of 20 nm. A high Curie temperature of about 385°C was measured for this composition. The nanocomposite magnet with a 25 wt.% α-Fe addition exhibits the best combination of magnetic properties: J_r = 1.19 T, $\mu_0 H_c$ = 0.66 T and $(BH)_{max}$ = 178 kJm^{-3}. Zr and Co additives have been shown to play an important role controlling the microstructure and resulting in an average grain size of about 20 and 15 nm for the hard and the soft magnetic phases, respectively. The latter one is an α-(Fe,Co) phase due to a diffusional redistribution of Co and Fe taking place during the crystallisation process. This optimised nanocomposite magnet shows a $T_C \approx$ 365°C. Furthermore, magnetically single-phase behaviour is observed for magnets containing 5 - 35 wt.% α-Fe as a consequence of an effective exchange-coupling between the two different phases due to the very fine nanostructure.

8 Initial magnetisation and reversal magnetisation processes in nanocrystalline magnets

Three different types of milled-and-annealed alloys have been considered in this chapter: (i) a Pr-rich alloy with composition $Pr_{14.7}Fe_{77.3}B_{8.0}$; (ii) a nearly single-phase alloy with starting composition $Pr_{9.0}Nd_{3.0}Dy_{1.0}Fe_{72.0}Co_{8.0}B_{6.9}Zr_{0.1}$ and (iii) a series of nanocomposites prepared by milling the latter alloy with various amounts of α-Fe (5 - 35 wt.% α-Fe).

The behaviour of the initial magnetisation curves for different transition-metal contents and annealing temperatures, i.e. grain sizes, has been studied. Two characteristic lengths can be calculated from the corresponding intrinsic magnetic properties, the critical single-domain particle size given by the proportionality $d_c \sim \mu_0(AK_1)^{1/2}/J_s^2$, and the wall thickness $\delta_w \approx \pi(A/K_1)^{1/2}$. For the compounds studied here, d_c is in the range of several hundred nanometers, but δ_w is only a few nanometers (see Table 4.2). Thus, the mean grain sizes are decisive because the formation of classical domain structures can take place only within relatively large grains, but microstructural studies of the materials (Chapters 6 and 7) have shown, in general, very fine microstructures.

Reversibility measurements of the demagnetisation curves give important information about the magnetisation processes. Recoil loops have been measured for a number of starting fields along the demagnetisation curve of a previously saturated sample. A systematic analysis of the exchange-coupling phenomena when varying the α-Fe content, the annealing temperature (grain size) and the measurement temperature has been carried out, and the well known Wohlfarth's remanence analysis (Chapter 3) has been used to analyse the corresponding processes during demagnetisation. An additional study of the reversible and the irreversible changes in polarisation during magnetisation can be very useful to obtain additional information on the mechanisms responsible for exchange-coupling in these nanocomposite permanent magnets.

8.1 Initial magnetisation processes

Figure 8.1 shows the evolution of the initial magnetisation curves for $Pr_{14.7}Fe_{77.3}B_{8.0}$ (alloy (8)) in the thermally demagnetised state after milling and after different annealing treatments starting from the amorphous state. Annealing at 450°C for 10 minutes results in the highest saturation polarisation which can be due to a microstructure consisting of nanocrystallites of α-Fe embedded in an amorphous matrix (see XRD pattern in Fig. 6.3). The significant grain growth of the α-Fe phase and the practical disappearance of the amorphous phase after annealing at 450°C for 30 min lead to a decreased saturation polarisation. Annealing at 500°C leads to significant remanence and coercivity values due to the coexistence of the crystallised $Pr_2Fe_{14}B$ phase with enlarged α-Fe grains. After annealing at 550°C, the formation of the $Pr_2Fe_{14}B$ phase appears to be completed with only a small amount of α-Fe being present. XRD patterns (Fig. 6.3) and the origin of the coercivity (Fig. 6.5) support these observations. After annealing at 600°C the initial magnetisation curve exhibits two magnetisation stages as it can be seen in Fig. 8.1. The formation of an inhomogeneous microstructure at this annealing temperature (as shown in Fig. 6.9) with a fraction of grains in a multi-domain state as well as grains in a

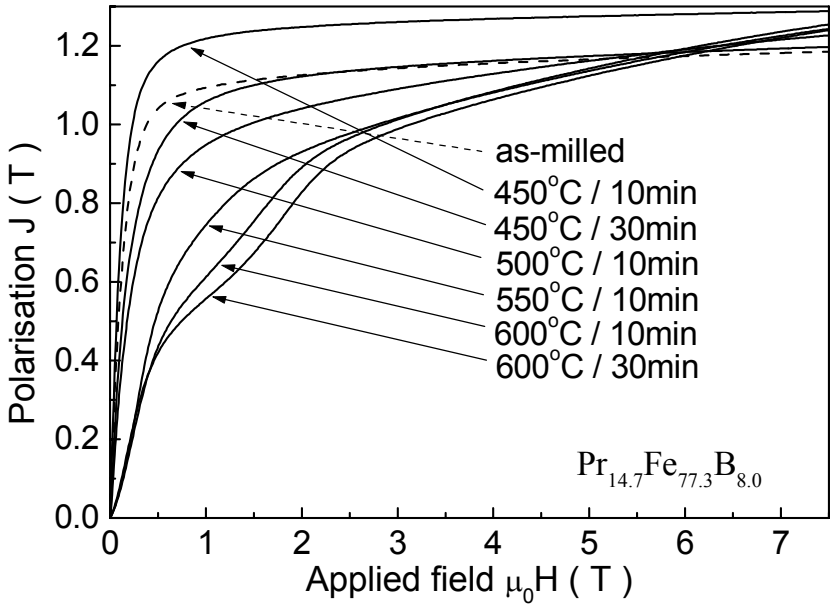

Fig. 8.1: Initial magnetisation curves for $Pr_{14.7}Fe_{77.3}B_{8.0}$ (alloy(8)) after milling and annealing at different temperatures and/or times.

single-domain state could be the reason for the more complicated magnetisation process. The theoretical critical domain size below which formation of a domain wall is energetically unfavourable, is d_c = 0.3 μm (assuming no interactions with neighbouring grains) [7,20]. However, the critical domain size in these samples could be significantly smaller than the theoretical value for an isolated grain as it is pointed by Kronmüller [35] and Folks [48]. For applied fields $\mu_0 H_{appl} < 1$ T, the domain walls are easily moved within the grains (which determines the first step of the magnetisation curve). Larger applied fields put all the grains into a single-domain state leading to a second step in the initial magnetisation curve for $H_{appl} \approx H_c$. Additionally, the pinning of the domain walls at the Pr-rich grain boundary phase during the magnetisation process must be considered. The first step cannot be observed during demagnetisation of the previously saturated sample (see Fig. 6.5) due to the fact that all the multi-domain grains have become single-domain grains. Increased annealing temperature and/or time lead to larger grains and thus, to an increased fraction of multi-domain particles, obtaining a behaviour more similar to nucleation type (as that typically observed in sintered magnets): high initial susceptibility and single-step process [11]. This can be observed in Fig. 8.2a where the initial magnetisation curve after annealing at 600°C has been plotted together with those after annealing at 700 and 800 °C. Figures 8.2b,c show the initial magnetisation curve for the nearly single-phase material ($Pr_{9.0}Nd_{3.0}Dy_{1.0}Fe_{72.0}Co_{8.0}B_{6.9}Zr_{0.1}$) and the nanocomposite material (($Pr_{9.0}Nd_{3.0}Dy_{1.0}Fe_{72.0}Co_{8.0}B_{6.9}Zr_{0.1}$ + 25wt.% α-Fe) after identical annealing conditions. After annealing at 600 and 700 °C the single-phase material (Fig. 8.2b) exhibits a behaviour which is very different to that of the PrFeB alloy under the same conditions. $Pr_{9.0}Nd_{3.0}Dy_{1.0}Fe_{72.0}Co_{8.0}B_{6.9}Zr_{0.1}$ shows a very fine microstructure (see Fig. 7.3) with grains smaller than the critical single-domain size, d_c. In such fine-grained materials, where classical domain walls cannot exist, the mechanism responsible for those different initial susceptibilities is not yet fully understood. Eckert *et al* [11] mention that a strong magnetic interaction between the grains must be taken into account to explain that behaviour. The single-phase material exhibits a change in the magnetisation process only after annealing at 800°C due to the grain growth effect (Fig. 8.2b). The nanocomposite magnet (Fig. 8.2c) shows the same magnetisation process characteristic for these fine-grained materials

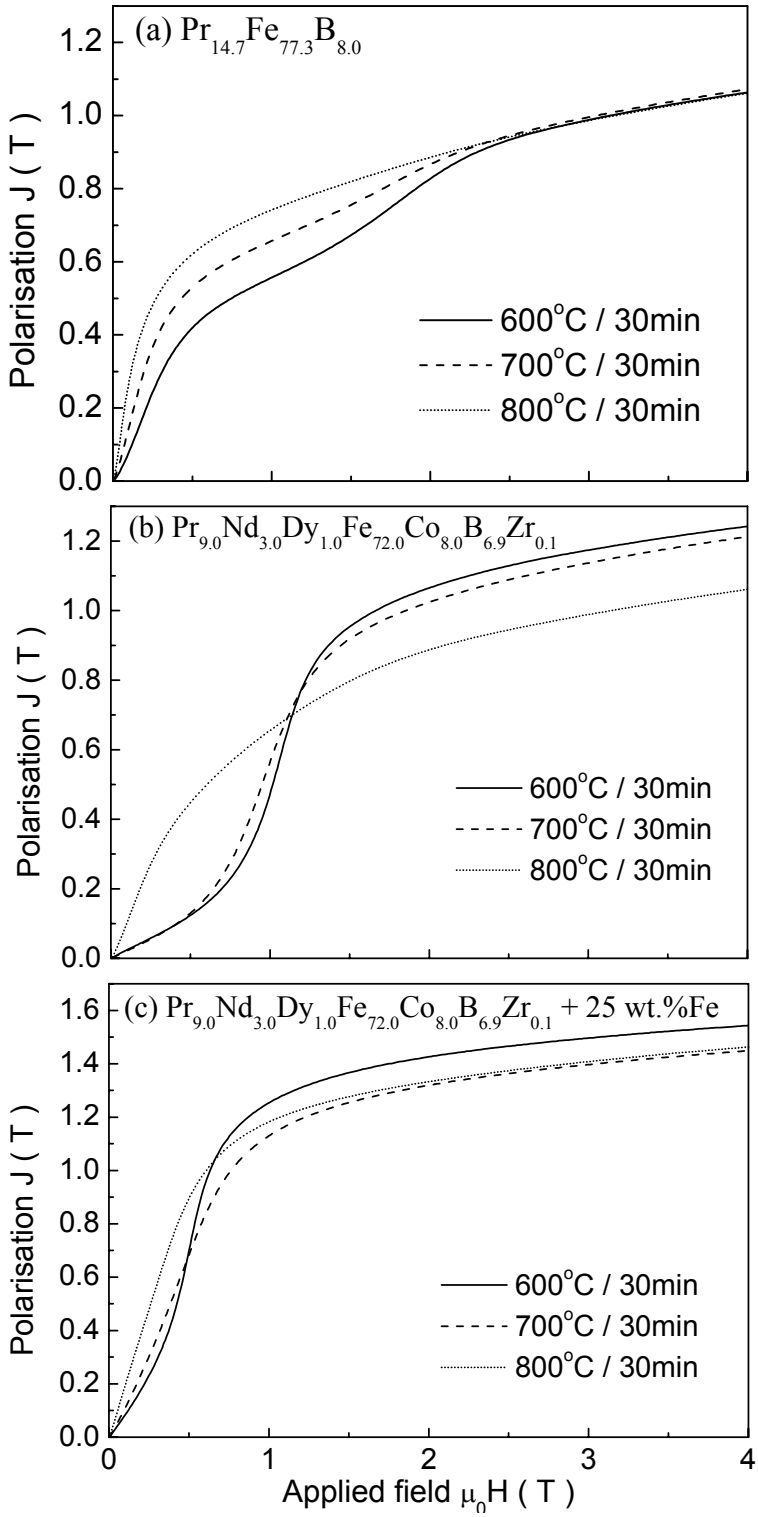

Fig. 8.2: Initial magnetisation curves after annealing at different temperatures for: (a) $Pr_{14.7}Fe_{77.3}B_{8.0}$ (alloy(8)); (b) $Pr_{9.0}Nd_{3.0}Dy_{1.0}Fe_{72.0}Co_{8.0}B_{6.9}Zr_{0.1}$ and (c) $Pr_{9.0}Nd_{3.0}Dy_{1.0}Fe_{72.0}Co_{8.0}B_{6.9}Zr_{0.1}$ + 25wt.% α-Fe.

after annealing at 600, 700 and 800 °C. There is an expected increased initial susceptibility with increasing annealing temperature possibly due to the existence of larger soft magnetic grains. However, a magnetically single-phase behaviour is observed during demagnetisation, even after annealing at 800°C (Fig. 8.3), as a result of an effective exchange-coupling between the different grains. By comparison, the demagnetisation curve for $Pr_{14.7}Fe_{77.3}B_{8.0}$ (Fig. 8.3) exhibits two steps, the first one is due to the nucleation of reverse domains in the larger grains ($d > d_c$) and, the second one, at high reverse applied fields ($H_{appl} > H_c$), is due to the demagnetisation process of the smaller grains ($d < d_c$).

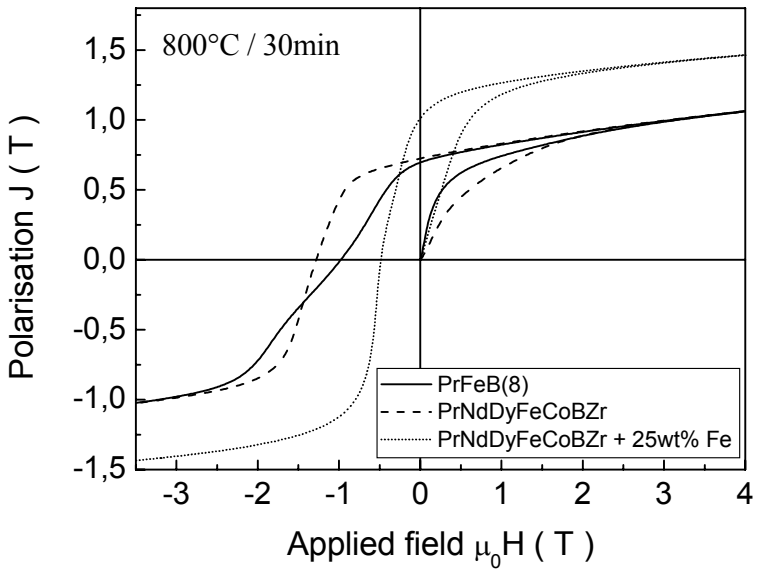

Fig. 8.3: Initial magnetisation and demagnetisation curves after annealing at 800°C for: (a) $Pr_{14.7}Fe_{77.3}B_{8.0}$ (alloy(8)); (b) $Pr_{9.0}Nd_{3.0}Dy_{1.0}Fe_{72.0}Co_{8.0}B_{6.9}Zr_{0.1}$ and (c) $Pr_{9.0}Nd_{3.0}Dy_{1.0}Fe_{72.0}Co_{8.0}B_{6.9}Zr_{0.1}$ + 25wt.% α-Fe.

The effect of the α-Fe content on the initial magnetisation for the nanocomposite $Pr_{9.0}Nd_{3.0}Dy_{1.0}Fe_{72.0}Co_{8.0}B_{6.9}Zr_{0.1}$ + x wt.% α-Fe (x = 0 – 35) can be seen in Fig. 8.4. This result shows that the addition of α-Fe leads to a magnetic softening of the nanocomposite magnet resulting in a higher initial susceptibility with increasing α-Fe content. Evolution of remanence and coercivity for different α-Fe fractions shows this behaviour very clearly (Fig. 7.6).

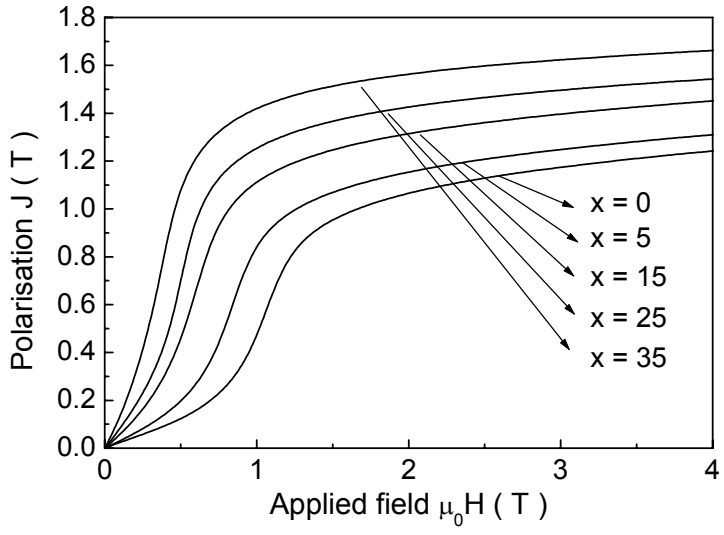

Fig. 8.4: Initial magnetisation curves for $Pr_{9.0}Nd_{3.0}Dy_{1.0}Fe_{72.0}Co_{8.0}B_{6.9}Zr_{0.1}$ + x wt.% α-Fe (x = 0 – 35) after milling and annealing (600°C / 30 min).

8.2 Recoil loops at room temperature

Recoil loops of the decoupled magnets are completely closed whereas those of the $Pr_{9.0}Nd_{3.0}Dy_{1.0}Fe_{72.0}Co_{8.0}B_{6.9}Zr_{0.1}$ alloy and the composite magnets are relatively open (Fig. 8.5), due to the reversible rotation of the exchange-coupled soft phase for fields not large enough to reverse the magnetisation of the hard magnetic phase (exchange-spring mechanism).

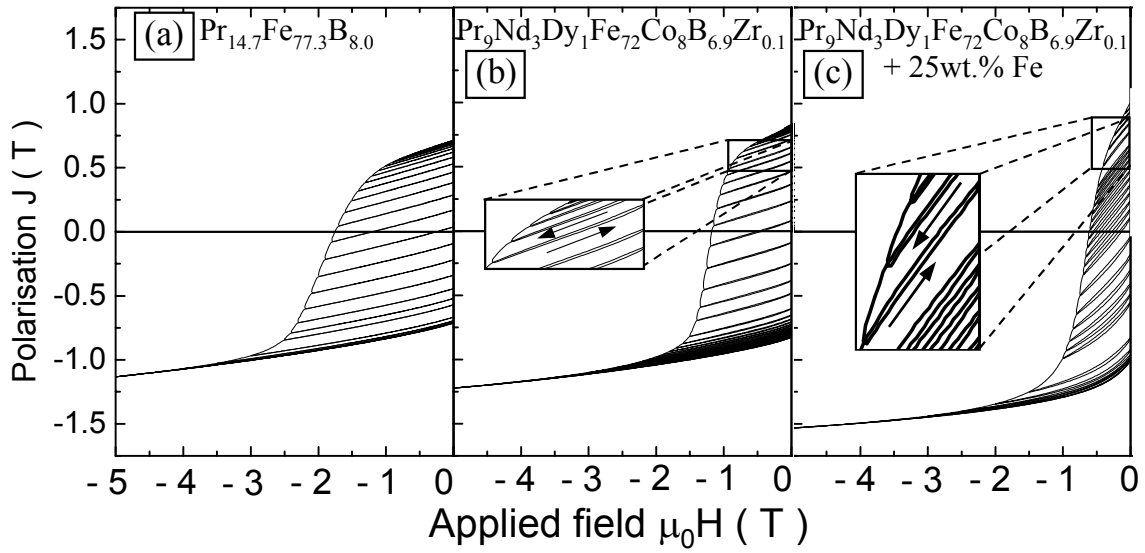

Fig. 8.5: Demagnetisation curves and recoil loops for (a) $Pr_{14.7}Fe_{77.3}B_{8.0}$ (alloy(8)), (b) $Pr_{9.0}Nd_{3.0}Dy_{1.0}Fe_{72.0}Co_{8.0}B_{6.9}Zr_{0.1}$ and (c) $Pr_{9.0}Nd_{3.0}Dy_{1.0}Fe_{72.0}Co_{8.0}B_{6.9}Zr_{0.1}$ + 25wt% α-Fe.

8.3 Analysis of exchange-coupling using δ*J*-plots

Wohlfarth [46] showed that the remanent polarisation $J_r(H_m)$, which is measured after magnetisation at the magnetising field H_m, and the demagnetisation remanence J_r^d, which is measured after demagnetisation at $-H_m$, should obey the relationship: $J_r^d(H_m) = J_r - 2J_r^m(H_m)$, where J_r is the maximum remanent polarisation (remanence) after magnetisation with the maximum field (see Section 3.3). The deviation of $J_r^d(H_m)$ from Wohlfarth's relationship can be used for an interpretation of intergrain interactions. In this way, the well known δ*J*-plot is a graphical presentation of Wohlfarth's relation in dependence on the applied magnetic field which illustrates the deviations from the theoretical value for $J_r^d(H_m)$. The evolution of the magnetisation curve and the δ*J* values have been studied when varying the (i) α-Fe content; (ii) the annealing temperature, i.e. the grain size and (iii) the measurement temperature.

8.3.1 The effect of the α-Fe content

It is obvious from Fig. 8.5 that samples with a lower R-content show a higher permeability on the recoil curves of the second and the third quadrant of the *J*-*H*-plane. The total polarisation, *J(H)*, becomes zero along the major demagnetisation curve for a certain applied reverse field: the coercive field, H_c. However, removal of the field brings the magnetic material back to a remanent state with a considerably large polarisation, $J_r^d(H_c)$. The quantity $J_r^d(H_m)$ is defined as the remanent polarisation after demagnetising the saturated sample in a reverse field H_m. If $J_r^d(H_m) = 0$ the applied field $H_m = H_r$ is denoted as remanent coercivity. H_r depends only on the irreversible part of the demagnetisation process in contrast to the intrinsic coercivity, H_c, which includes both reversible and irreversible changes. For different samples Fig. 8.6 shows plots of: (left) initial magnetisation and demagnetisation curves and recoil loops; (right) total polarisation during major magnetisation (*m*) and demagnetisation (*d*) curves, $J_s^{(m/d)}(H_m)$, remanent polarisation, $J_r^{(m/d)}(H_m)$, and the difference between both amounts, $J_{rev}^{(m/d)}(H_m)$, which is associated to reversible rotation of the magnetic moments during application of the field H_m.

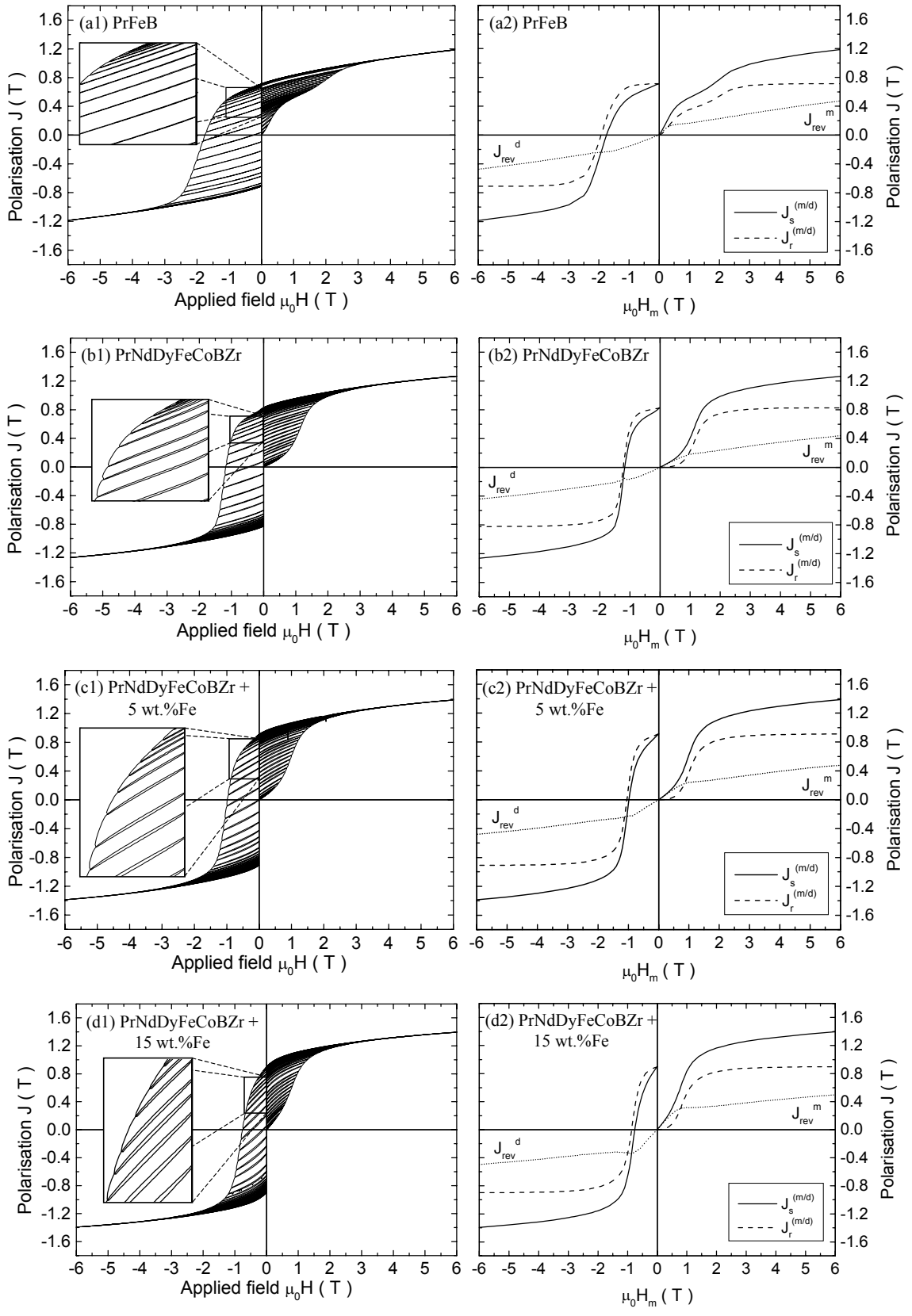
(a1) PrFeB
(a2) PrFeB
(b1) PrNdDyFeCoBZr
(b2) PrNdDyFeCoBZr
(c1) PrNdDyFeCoBZr + 5 wt.%Fe
(c2) PrNdDyFeCoBZr + 5 wt.%Fe
(d1) PrNdDyFeCoBZr + 15 wt.%Fe
(d2) PrNdDyFeCoBZr + 15 wt.%Fe
Polarisation J (T)
Applied field μ0H (T)
μ0Hm (T)
Jrev d
Jrev m
Js (m/d)
Jr (m/d)

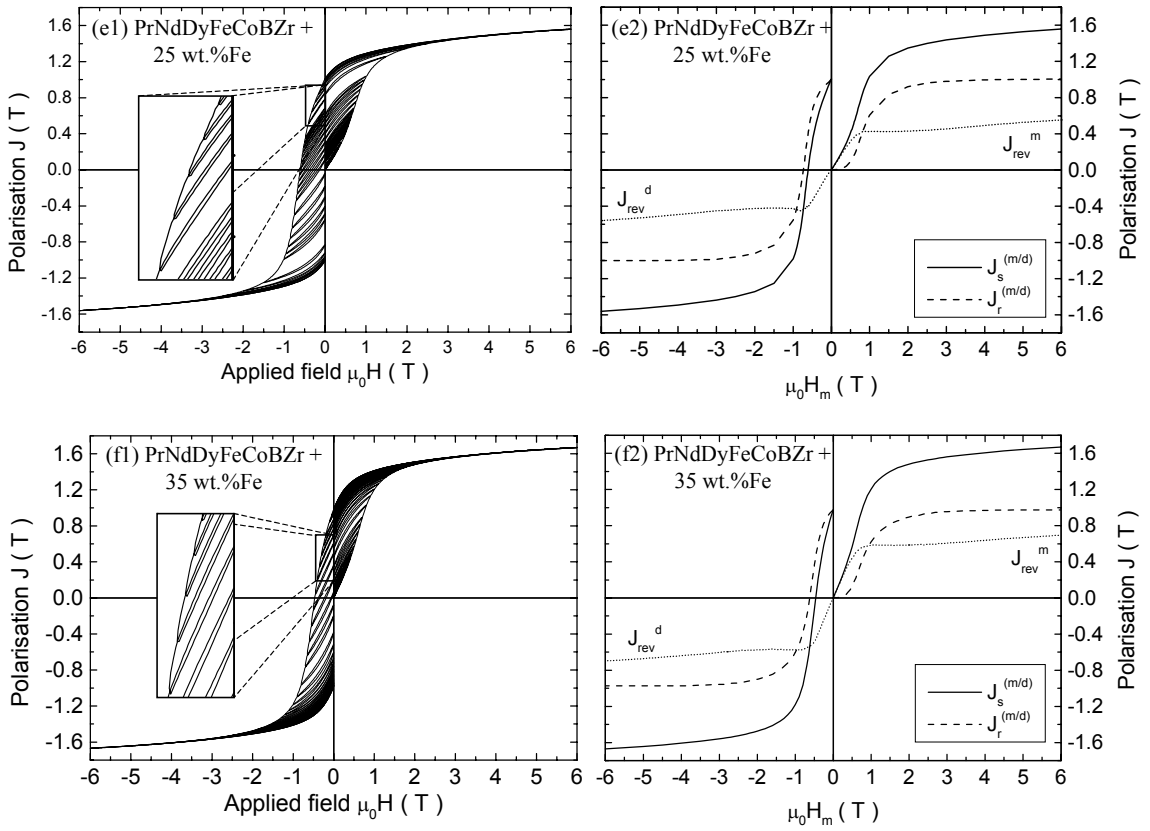

Fig. 8.6: Left: Initial magnetisation curves, demagnetisation curves and recoil loops for milled and annealed (T_a = 600°C): (a) $Pr_{14.7}Fe_{77.3}B_{8.0}$; (b) $Pr_{9.0}Nd_{3.0}Dy_{1.0}Fe_{72.0}Co_{8.0}B_{6.9}Zr_{0.1}$; (c) $Pr_{9.0}Nd_{3.0}Dy_{1.0}Fe_{72.0}Co_{8.0}B_{6.9}Zr_{0.1}$ + 5wt.% α-Fe; (d) $Pr_{9.0}Nd_{3.0}Dy_{1.0}Fe_{72.0}Co_{8.0}B_{6.9}Zr_{0.1}$ + 15wt.% α-Fe; (e) $Pr_{9.0}Nd_{3.0}Dy_{1.0}Fe_{72.0}Co_{8.0}B_{6.9}Zr_{0.1}$ + 25wt.% α-Fe and (f) $Pr_{9.0}Nd_{3.0}Dy_{1.0}Fe_{72.0}Co_{8.0}B_{6.9}Zr_{0.1}$ + 35wt.% α-Fe. Right: Plots of total polarisation during major magnetisation (m) and demagnetisation (d) curves, $J_s^{(m/d)}(H_m)$, remanent polarisation, $J_r^{(m/d)}(H_m)$, and the difference between both amounts, $J_{rev}^{(m/d)}(H_m)$, which is associated to reversible rotation of the magnetic moments during application of the field H_m. Measurements performed at room temperature using thermally demagnetised samples.

Values for the remanent coercivity obtained from the plot of J_r^d vs. H_m are listed in Table 8.1. The increased recoil permeability with increasing α-Fe content due to the reversible rotation of the exchange-coupled soft phase for fields not large enough to switch the hard magnetic phase should be noted. Considering the difference in magnetisation when traversing the recoil curve, starting from a point on the demagnetisation curve for a given field and terminating on the recoil curve at zero field (reversible change in polarisation, J_{rev}^d), m_{rev} can be defined as $m_{rev}=J_{rev}^d / J_r$. The corresponding irreversible change is defined as $m_{irr}=[J_r - J_r^d(H_m)]/2J_r$ [51,53]. Both quantities are plotted versus the

demagnetising field, H_m^d, in Figs. 8.7a,b, respectively. The irreversible susceptibility is given by $\chi_{irr}(H) = dm_{irr} / dH$ [55] and, according to the model of Kneller and Hawig [31], the maximum corresponds to the nucleation field, H_{no}, for irreversible magnetisation reversal (Fig. 8.7c). The corresponding H_{no} values are listed in Table 8.1.

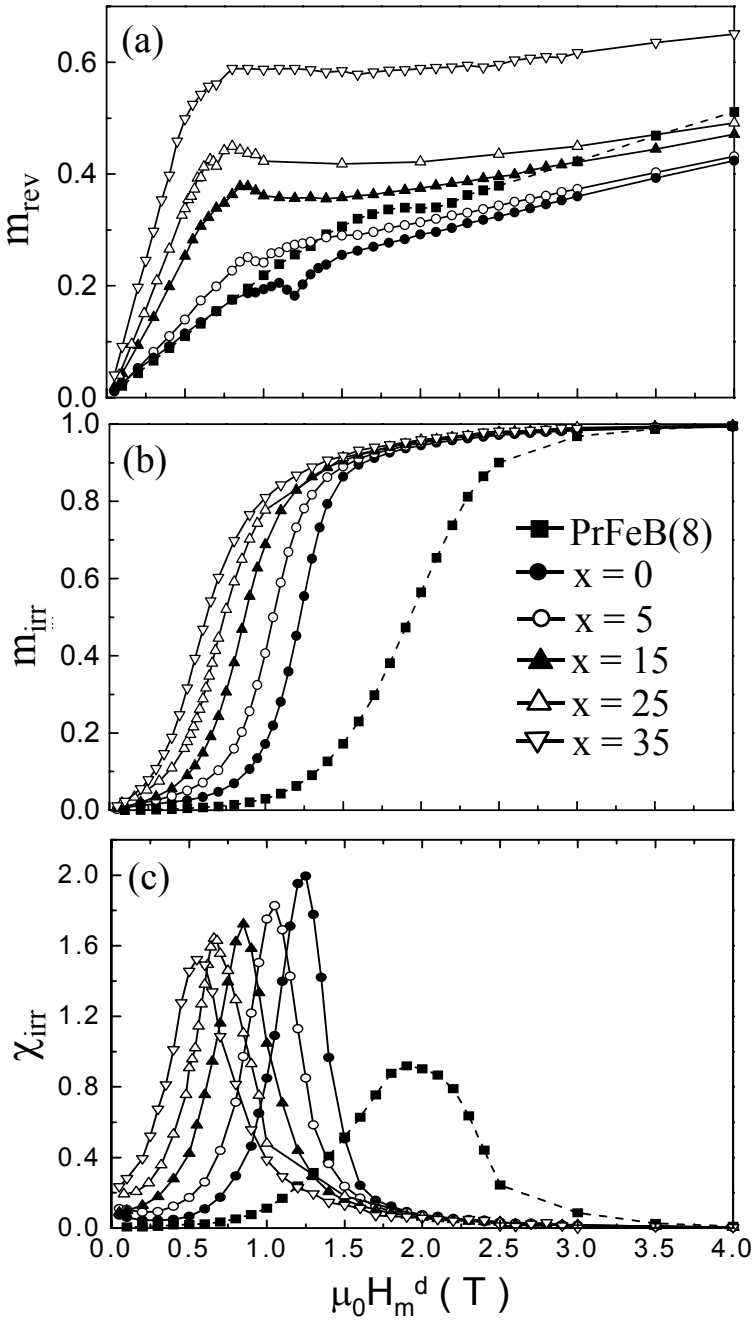

Fig. 8.7: (a) Reversible reduced portion, $m_{rev} = J_{rev}^d / J_r$; (b) irreversible reduced portion, $m_{irr} = J_{irr} / J_r$ and (c) irreversible susceptibility, $\chi_{irr} = dm_{irr} / dH$ in T^{-1} vs. the demagnetising field H_m^d for $Pr_{14.7}Fe_{77.3}B_{8.0}$ (alloy (8)) and $Pr_{9.0}Nd_{3.0}Dy_{1.0}Fe_{72.0}Co_{8.0}B_{6.9}Zr_{0.1}$ + x wt.% α-Fe (x = 0, 5, 15, 25 and 35).

Sample	$\mu_0 H_c$ (T)	$\mu_0 H_{no}$(T)	$\mu_0 H_r$ (T)	$\alpha' = J_r / J(8T)$
PrFeB(8)	1.74	1.92	1.92	0.50
PrNdDyFeCoBZr (x=0)	1.17	1.22	1.22	0.66
x = 5 wt.%Fe	0.98	1.04	1.05	0.68
x = 15 wt.%Fe	0.76	0.85	0.87	0.69
x = 25 wt.%Fe	0.60	0.68	0.74	0.73
x = 35 wt.%Fe	0.46	0.55	0.62	0.74

Table 8.1: Coercivity, $\mu_0 H_c$ (T); nucleation field, $\mu_0 H_{no}$ (T); remanent coercivity, $\mu_0 H_r$ (T) and relative remanence, $\alpha' = J_r / J(8T)$, for milled $Pr_{14.7}Fe_{77.3}B_{8.0}$ (alloy (8)) and $Pr_{9.0}Nd_{3.0}Dy_{1.0}Fe_{72.0}Co_{8.0}B_{6.9}Zr_{0.1}$ + x wt.% α-Fe (x = 0 - 35) alloys after annealing at 600ºC.

The nucleation field, H_{no}, and the remanent coercivity, H_r, depend only on the irreversible part of the demagnetisation process. In the case of the PrFeB and PrNdDyFeCoBZr (x = 0) alloys, only one critical field is found: $H_m = H_{no} = H_r$ (see Table 8.1) corresponding to the necessary applied field for irreversible magnetisation reversal. However, there is a difference between the values for both fields for the nanocomposite magnets, with $H_r > H_{no}$ for all of them, and this difference becomes larger with increasing α-Fe content. This can be explained considering the mechanism of magnetisation reversal in two-phase magnets [31]: under the action of a reverse field the magnetisation vector of the decoupled soft magnetic phase rotates towards the field. When increasing the reverse field, reversible rotation of the exchange-coupled soft phase will take place until it becomes energetically unfavourable to support the non-uniform magnetisation at the interface [49]. Thus, at a value of the reverse field of $H_m = H_{no}$, the reversible magnetisation of the soft phase provides the additional driving force for reversal of the hard phase, i.e. the magnetisation of the hard magnetic phase undergoes an irreversible change. This can be explained considering that, in addition to the external demagnetising field, there is a further reversing action on the moments of the hard phase that comes from the exchange-coupling to the soft phase [66]. Thus, an irreversible magnetisation reversal will not occur in the hard phase for reverse fields $H_m < H_{no}$. It is necessary, however, to increase further the reverse field, up to $H_m = H_r$, in order to initiate the irreversible rotation of the decoupled or partly-coupled inner hard magnetic moments. Higher reverse fields, $H_m > H_r$, will lead to more magnetic moments of the hard phase contributing to the irreversible change in polarisation, J_r^d, up to a certain applied field ($\mu_0 H_m \approx 4.5$ T for PrFeB; $\mu_0 H_m \approx$

4 T for x = 0 - 15; $\mu_0 H_m \approx 3.75$ T for x = 25 and $\mu_0 H_m \approx 3.5$ T for x = 35, as it can be observed on the right hand side of Fig. 8.6). Increased reverse fields lead to a constant value of the irreversible change in polarisation: $J_r^d = J_r$ (Fig. 8.6); thus, the corresponding increase of the total polarisation (containing contributions from both reversible and irreversible processes), J_s^d, can be attributed exclusively to reversible changes in the polarisation, J_{rev}^d, at those higher applied fields. The explained behaviour is supported by the evolution of the $m_{rev}(H_m)$ curve (Fig. 8.7a). Steeper starting curves are obtained with increasing α-Fe content as a result of the larger contribution of the soft phase to the recoverable portion. PrFeB and PrNdDyFeCoBZr (x = 0) alloys exhibit the same reversible change in polarisation for fields $H_m < H_{no}$ of the latter, which could explain this contribution to be mainly due to the reversible rotation of the decoupled hard magnetic moments for the single-phase alloy. At $H_m \approx H_{no}$ the most unfavourably aligned magnetic moments (those strongly exchange-coupled in the remanent state, J_r), which are responsible for the remanent demagnetisation of the whole sample, begin to irreversibly rotate in the direction of the applied field. All nanocomposite materials (x = 5 - 35) exhibit a decreased susceptibility in the $m_{rev}(H_m)$ curve at $H_m \approx H_{no}$ due to the beginning of irreversible rotation of the hard magnetic moments exchanged-coupled to the neighbouring soft magnetic grains. A local maximum is observed when increasing the reverse field up to $H_m \approx H_r$. The immediate decrease in the m_{rev} values is associated to the change of reversible-to-irreversible rotation of the decoupled hard magnetic moments. Once these magnetic moments are irreversibly rotated, further increased reversed fields lead to a progressive increase of the m_{rev} values. This is mainly due to a more parallel alignment of the moments to the applied field with increasing its intensity.

The study of the interactions between the grains during magnetisation reversal can be done by dividing the $J_r^d(H_m)$ curve into two parts: first, starting from the remanence state after saturation, J_r, and finishing at $J_r^d(H_r) = 0$; second, starting from this latter remanent state and finishing at $-J_r$ after removing the highest reversal applied field. Considering only the changes in polarisation due to magnetisation reversal and normalising this change in respect to J_r, an amount δ*J* can be defined as

$$\delta J = \{[J_r^m(H_m) - (J_r - J_r^{d1}(H_m))] + [J_r^m(H_m) - (0 - J_r^{d2}(H_m))]\} / J_r \qquad (8.1)$$

where $J_r^{d1}(H_m)$ and $J_r^{d2}(H_m)$ are the remanent polarisation values for each of the considered processes. Taking into account that $J_r^{d1}(H_m) + J_r^{d2}(H_m) = J_r^{d}(H_m)$, the following expression results

$$\delta J = (2J_r^{m}(H_m) - (J_r - J_r^{d}(H_m))) / J_r \,. \tag{8.2}$$

This is exactly the expression shown in Section 3.4.2 for measuring the deviations from the theoretical value for $J_r^{d}(H_m)$ given by $J_r - 2J_r^{d}(H_m)$, corresponding to an assembly of magnetically non-interacting uniaxial single-domain particles, in other words, the deviation from the ideal behaviour according to Wohlfarth's model. For comparison Fig. 8.8 shows the δ*J* plots for PrFeB(8) and PrNdDyFeCoBZr(4) + x wt.% α-Fe (x = 0, 5, 15, 25 and 35). Here, two kinds of interactions are responsible for the deviation, δ*J*, from Wohlfarth's relationship (Eq. 3.1): magnetostatic and exchange interactions. It must be noted that in the case of the decoupled ternary alloy, δ*J* is exclusively positive. Such behaviour has been interpreted indicative of magnetostatic interactions being dominant between the decoupled hard magnetic grains [52]. In contrast, the base alloy (x = 0) shows an almost symmetrical shape (positive and negative deviations) and the alloys with lower Fe-addition (x = 5 - 15 wt.% α-Fe) show positive values of δ*J* that become negative after reversal of the hard magnetic grains, indicative of the dominating role of the exchange interactions in these samples although magnetostatic interactions must be also considered. In fact, it can be observed that an increase of the soft magnetic phase content leads to a stronger exchange interaction, with exclusively negative δ*J* values for the samples with x = 25 - 35 wt.% α-Fe. The final result is a more effective exchange-coupling between the two different magnetic phases, with relative remanences ranging from $\alpha' = 0.66$ for PrNdDyFeCoBZr to 0.74 for PrNdDyFeCoBZr + 35wt.% α-Fe. It must be noted, however, that these values for α' can be used only for comparison between the different samples because an applied field of 8 T is not sufficient to saturate them.

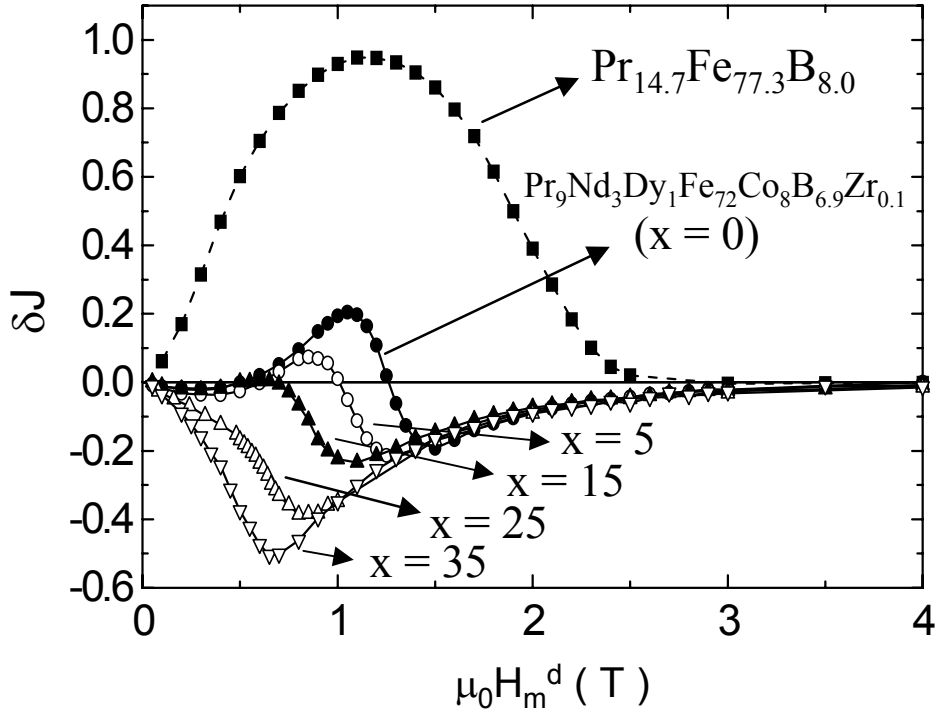

Fig. 8.8: Deviation of demagnetisation remanence, δJ, as function of the applied field for the decoupled $Pr_{14.7}Fe_{77.3}B_{8.0}$ (alloy (8)) and the nanocomposite magnets: $Pr_{9.0}Nd_{3.0}Dy_{1.0}Fe_{72.0}Co_{8.0}B_{6.9}Zr_{0.1}$ + x wt.% α-Fe (x = 0, 5, 15, 25 and 35).

8.3.2 The effect of the annealing temperature (grain size)

The effect of the annealing temperature on the hysteresis and inner recoil loops for $Pr_{9.0}Nd_{3.0}Dy_{1.0}Fe_{72.0}Co_{8.0}B_{6.9}Zr_{0.1}$ can be seen in Fig. 8.9. It must be noted that, by comparison with the sample annealed at 600ºC (see Fig. 8.6(b1)), the recoil loops are now completely closed after annealing at higher temperatures (700 or 800 ºC). This can be due to a significantly reduced content of α-Fe in the powders with increasing annealing temperature, with only a residual amount present after annealing at 700 and 800 °C.

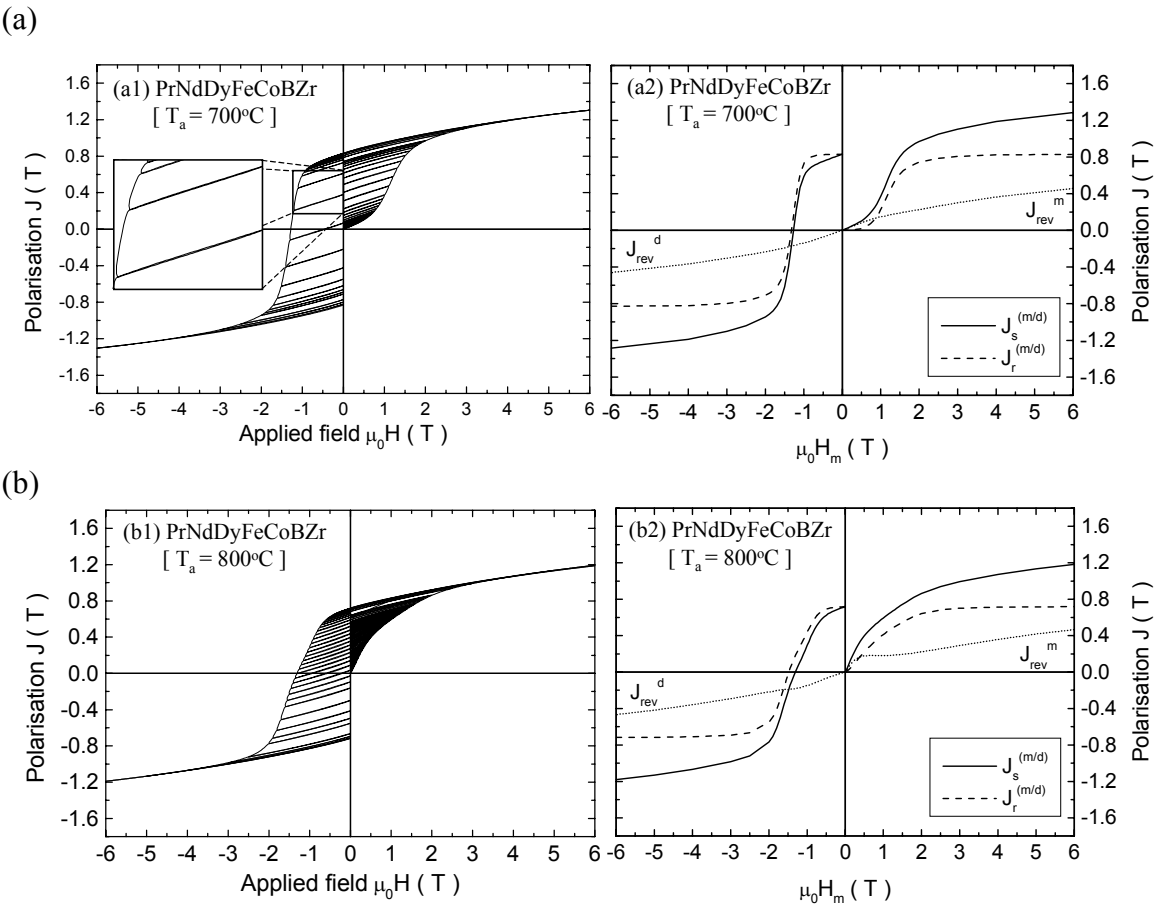

Fig. 8.9: $Pr_{9.0}Nd_{3.0}Dy_{1.0}Fe_{72.0}Co_{8.0}B_{6.9}Zr_{0.1}$ milled and annealed at: (a) T_a = 700ºC; and (b) T_a = 800ºC. Plots of: (left) initial magnetisation and demagnetisation curves including recoil loops; (right) total polarisation during major magnetisation (m) and demagnetisation (d) curves, $J_s^{(m/d)}(H_m)$, remanent polarisation, $J_r^{(m/d)}(H_m)$, and the difference between both amounts, $J_{rev}^{(m/d)}(H_m)$.

The reversible reduced portion, m_{rev}, and the irreversible susceptibility, χ_{irr}, after annealing at different temperatures are plotted in Fig. 8.10. The faster increase of the starting m_{rev} values after annealing at 600ºC can be due to the presence of the remaining exchange-coupled soft magnetic phase. Increased annealing temperatures result in a grain growth effect and, as a consequence, a decreased effectiveness of the exchange-coupling between the grains can be observed (see Table 8.2).

The corresponding values for coercivity, H_c, nucleation field, H_{no}, and remanent coercivity, H_r, after annealing at 600, 700 and 800 °C are listed in Table 8.2. The presence of two maxima in the $\chi_{irr}(H_m^d)$ curve for the sample annealed at 800ºC could be due to the

presence of larger hard magnetic grains. This could explain the slight shoulder observed in the corresponding major demagnetisation curve (see Fig. 8.9(b1)).

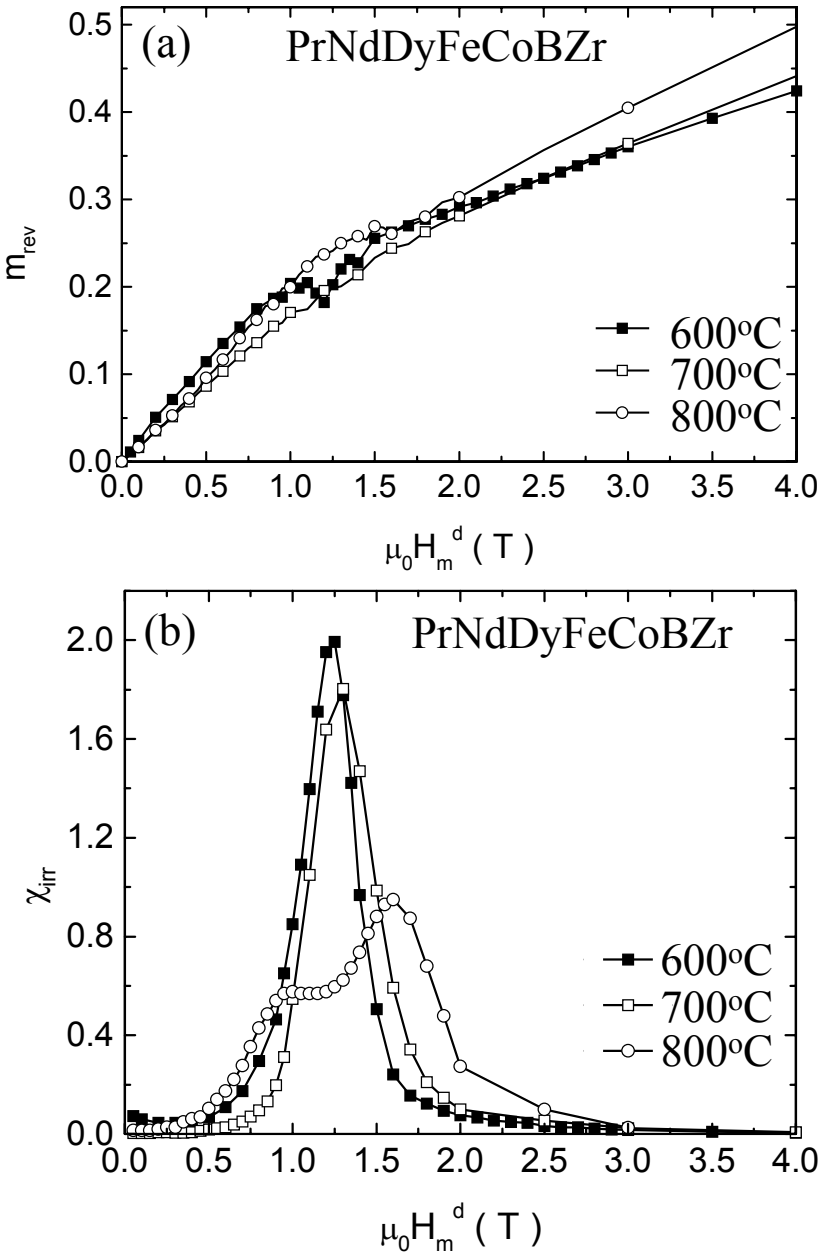

Fig. 8.10: (a) Reversible reduced portion, $m_{rev} = J_{rev}^{d} / J_r$, and (b) irreversible susceptibility defined as $\chi_{irr} = dm_{irr} / dH$ in T^{-1}, where m_{irr} is the normalised irreversible polarisation ($m_{irr} = J_{irr} / J_r$), vs. the applied field for $Pr_{9.0}Nd_{3.0}Dy_{1.0}Fe_{72.0}Co_{8.0}B_{6.9}Zr_{0.1}$ (x = 0) after annealing at: 600, 700 and 800 °C.

Annealing temp. (°C)	$\mu_0 H_c$ (T)	$\mu_0 H_{no}$ (T)	$\mu_0 H_r$ (T)	$\alpha' = J_r / J(8T)$
600	1.17	1.22	1.22	0.66
700	1.26	1.30	1.32	0.61
800	1.30	1;1.60	1.52	0.55

Table 8.2: Coercivity, $\mu_0 H_c$ (T); nucleation field, $\mu_0 H_{no}$ (T); remanent coercivity, $\mu_0 H_r$ (T); relative remanence, $\alpha' = J_r / J(8T)$, for milled $Pr_{9.0}Nd_{3.0}Dy_{1.0}Fe_{72.0}Co_{8.0}B_{6.9}Zr_{0.1}$ after annealing at different temperatures.

Figure 8.11 shows the δ*J* plots for PrNdDyFeCoBZr after the different annealing treatments. An increase of the annealing temperature leads to more positive deviations so that for the sample annealed at 800°C hardly any negative deviations are found, pointing to magnetostatic interactions to be predominant. This is the result of the decreased effectiveness of the exchange-coupling between the grains with increasing mean sizes, consistent with the expectations derived from the earlier described model.

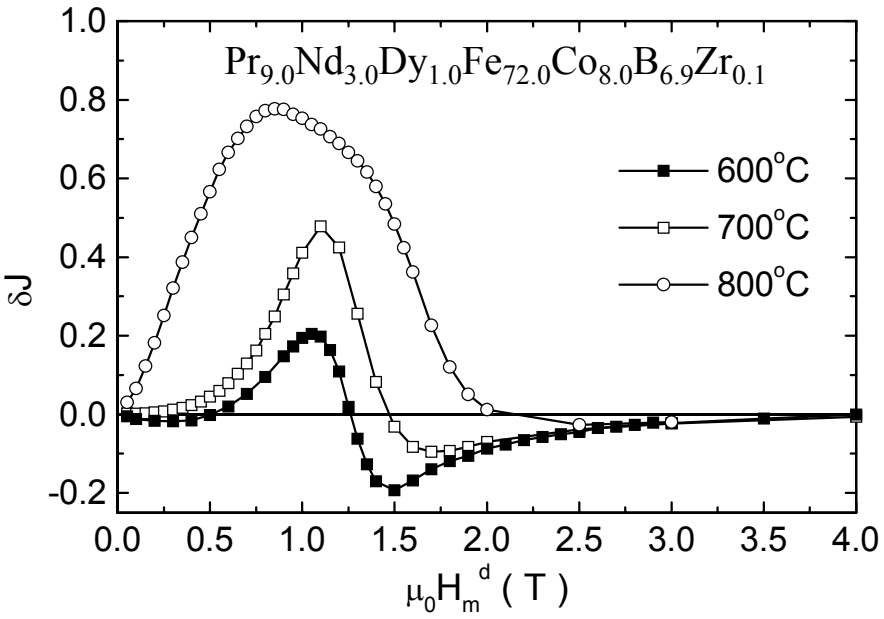

*Fig. 8.11: Deviation of demagnetisation remanence, δ*J*, as function of the field $\mu_0 H_m^d$ for as-milled $Pr_{9.0}Nd_{3.0}Dy_{1.0}Fe_{72.0}Co_{8.0}B_{6.9}Zr_{0.1}$ after annealing at: 600, 700 and 800 ºC.*

The hysteresis loop and inner recoil curves for the nanocomposite material PrNdDyFeCoBZr + 25wt.% α-Fe, after annealing at 700 and 800 ºC, are shown in Fig. 8.12. It can be observed that the recoil loops measured along the demagnetisation curve

look different from those corresponding to the single-phase magnet (Fig. 8.9). The recoil loops for the nanocomposite magnet after annealing at 600, 700 and 800 ºC exhibit comparatively steep recoil loops and they are relatively open due to the presence of the α-(FeCo) soft magnetic phase. An increased annealing temperature results, however, in less open recoil loops due to a decreased exchange-coupling between the different grains as a consequence of a grain growth effect. As it was shown in the XRD patterns of Fig. 6.3 a solid state reaction between the amorphous and nanocrystalline phases is required for crystallisation of the hard phase, and thus undesired grain growth of the soft phase cannot be avoided. The slightly higher coercivity of the sample annealed at 700ºC (see Table 8.3)

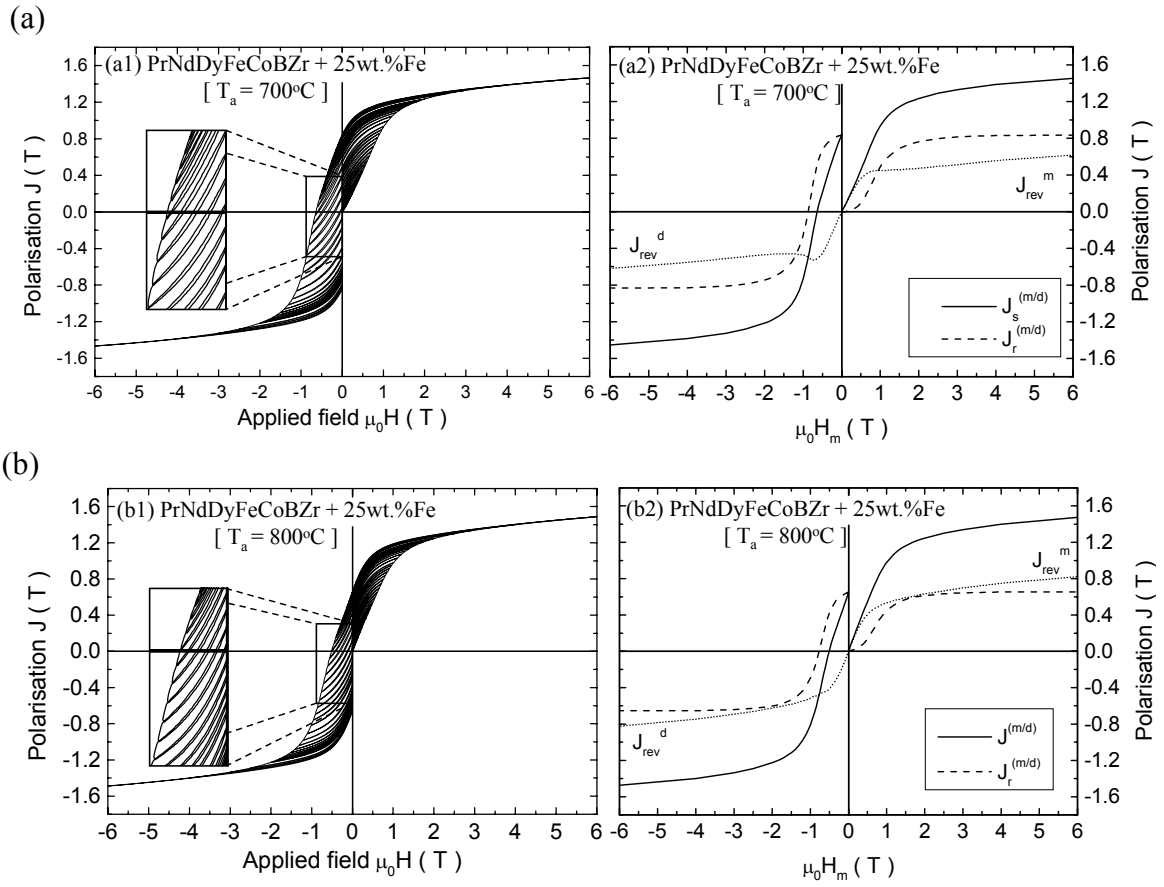

Fig. 8.12: $Pr_{9.0}Nd_{3.0}Dy_{1.0}Fe_{72.0}Co_{8.0}B_{6.9}Zr_{0.1}$ + 25wt.% α-Fe milled and annealed at: (a) T_a = 700ºC; and (b) T_a = 800ºC. Plots of: (left) initial magnetisation and demagnetisation curves including recoil loops; (right) total polarisation during major magnetisation (m) and demagnetisation (d) curves, $J_s^{(m/d)}(H_m)$, remanent polarisation, $J_r^{(m/d)}(H_m)$, and the difference between both amounts, $J_{rev}^{(m/d)}(H_m)$, which is associated to reversible rotation of the magnetic moments during application of the field H_m.

suggests that complete crystallisation of the hard phase was not completed at 600ºC. A decreased relative remanence, α', with increasing annealing temperature is indicative of the reduced exchange-coupling between the soft and the hard magnetic grains (Table 8.3). Grain growth of both, soft and hard magnetic grains, occurs when the annealing temperature is increased but the effective exchange-coupling range between both phases does not change. Considering the grain growth inhibiting effect of Zr on the $R_2T_{14}B$ phase, a faster increase in size for the soft magnetic grains can be expected when increasing the annealing temperature. Thus, the influence of the reversed magnetic moments of the soft phase will be relatively strong. In this situation, a reversing action on the moments of the hard phase that comes from the exchange-coupling to the soft phase is expected in addition to the applied demagnetising field [66]. This may explain the occurrence of larger m_{rev} values obtained with increasing annealing temperature (Fig. 8.13a), and the decreased critical fields, H_{no} and H_r, when increasing the annealing temperature from 700ºC (crystallisation of the $R_2T_{14}B$ phase completed) to 800ºC (see Table 8.3). The very large reversible contribution to the total polarisation for the annealing at 800ºC can be directly observed in Fig. 8.12(b2) by looking at the corresponding $J_{rev}^{\ d}$ values.

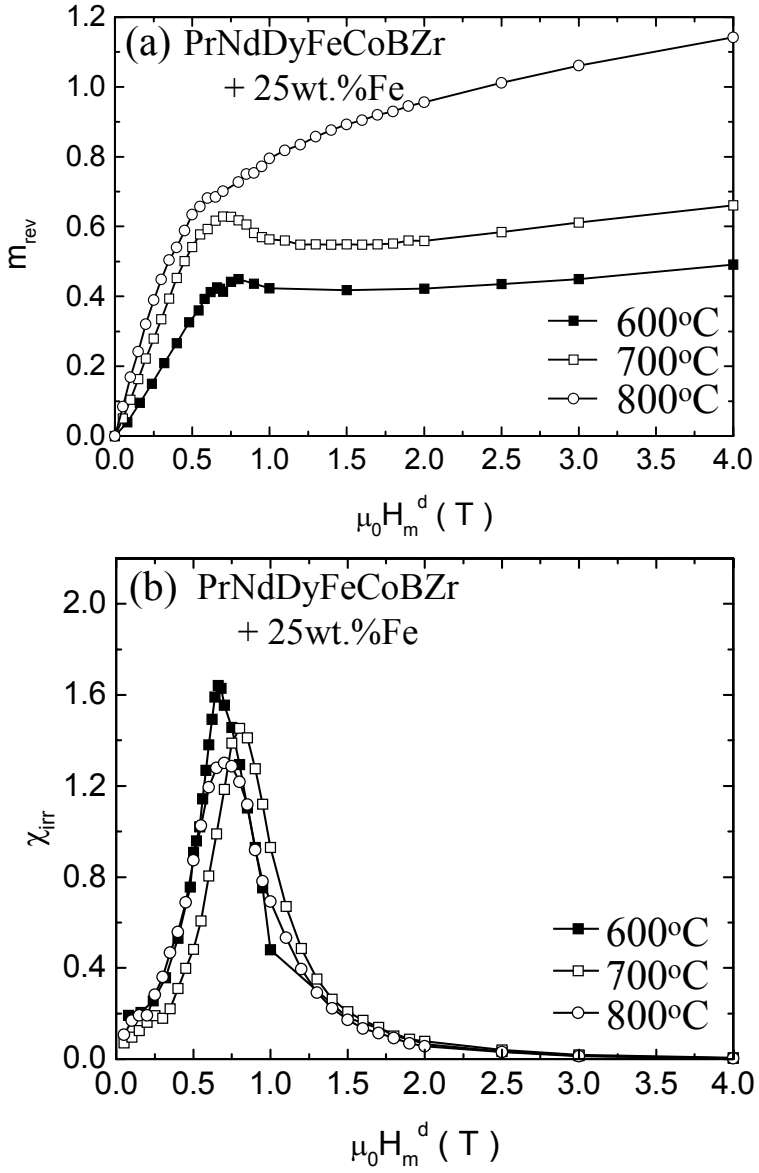

Fig. 8.13: (a) Reversible reduced portion, $m_{rev} = J_{rev}^{d} / J_r$, and (b) irreversible susceptibility defined as $\chi_{irr} = dm_{irr} / dH$ in T^{-1}, where m_{irr} is the normalised irreversible polarisation ($m_{irr} = J_{irr} / J_r$), vs. the applied field for $Pr_{9.0}Nd_{3.0}Dy_{1.0}Fe_{72.0}Co_{8.0}B_{6.9}Zr_{0.1}$ + 25wt.% α-Fe.

Annealing temp. (°C)	$\mu_0 H_c$ (T)	$\mu_0 H_{no}$ (T)	$\mu_0 H_r$ (T)	$\alpha' = J_r / J(8T)$
600	0.60	0.68	0.74	0.73
700	0.63	0.81	0.87	0.69
800	0.50	0.70	0.77	0.60

Table 8.3: Coercivity, $\mu_0 H_c$ (T); nucleation field, $\mu_0 H_{no}$ (T); remanence coercivity, $\mu_0 H_r$ (T); relative remanence, $\alpha' = J_r / J(8T)$, for milled $Pr_{9.0}Nd_{3.0}Dy_{1.0}Fe_{72.0}Co_{8.0}B_{6.9}Zr_{0.1}$ + 25wt.% α-Fe after annealing at different temperatures.

The evolution of δ*J* with increasing annealing temperature agrees very well with the previous results, showing a shift to positive values with increasing temperature (Fig. 8.14). Grain growth resulting in a less effective exchange-coupling explains the sign of the deviations from the theoretical value for $J_r^d(H_m)$.

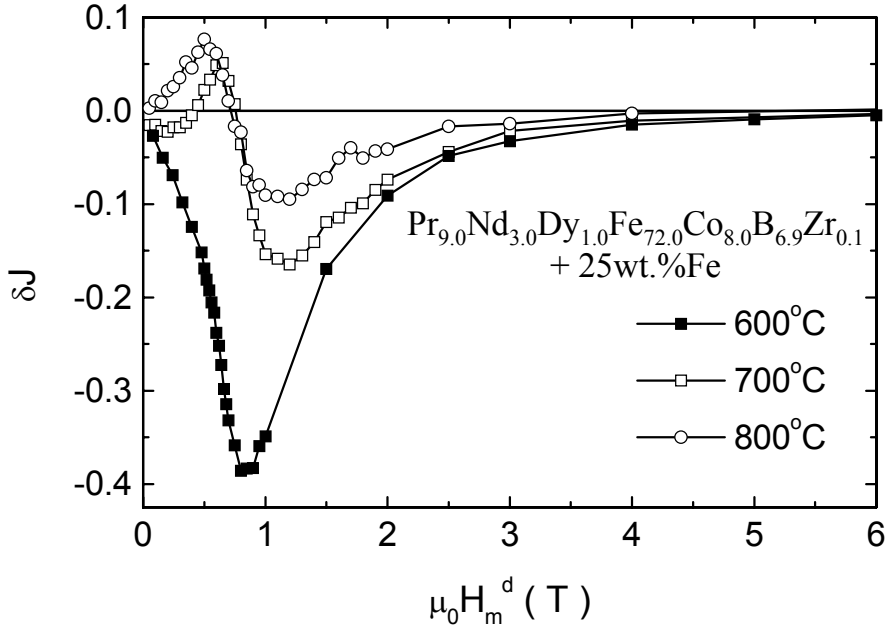

Fig. 8.14: Deviation of demagnetisation remanence, δJ, as a function of the field $\mu_0 H_m^d$ *(T) for milled* $Pr_{9.0}Nd_{3.0}Dy_{1.0}Fe_{72.0}Co_{8.0}B_{6.9}Zr_{0.1}$ *+ 25wt.% α-Fe after annealing at: 600, 700 and 800 °C.*

8.3.3 The effect of the measurement temperature

The evolution of the magnetic properties of $Pr_{9.0}Nd_{3.0}Dy_{1.0}Fe_{72.0}Co_{8.0}B_{6.9}Zr_{0.1}$ + x wt.% α-Fe (x = 0 and 25) milled and annealed at 600ºC in dependence on the temperature was studied in the temperature range from -200 to 200ºC. Both exchange-coupled magnets exhibit an enhanced remanence in that temperature range. Figure 8.15 shows the temperature dependence of (a) the remanence, (b) the coercivity and (c) the energy product $(BH)_{max}$. An increased content of α-Fe results in higher remanences but also in a better temperature stability of the remanence. Significantly smaller coercivities are obtained when increasing the α-Fe fraction but, on the other side, the thermal stability of the coercivity is largely improved. The energy product $(BH)_{max}$ takes higher values for the

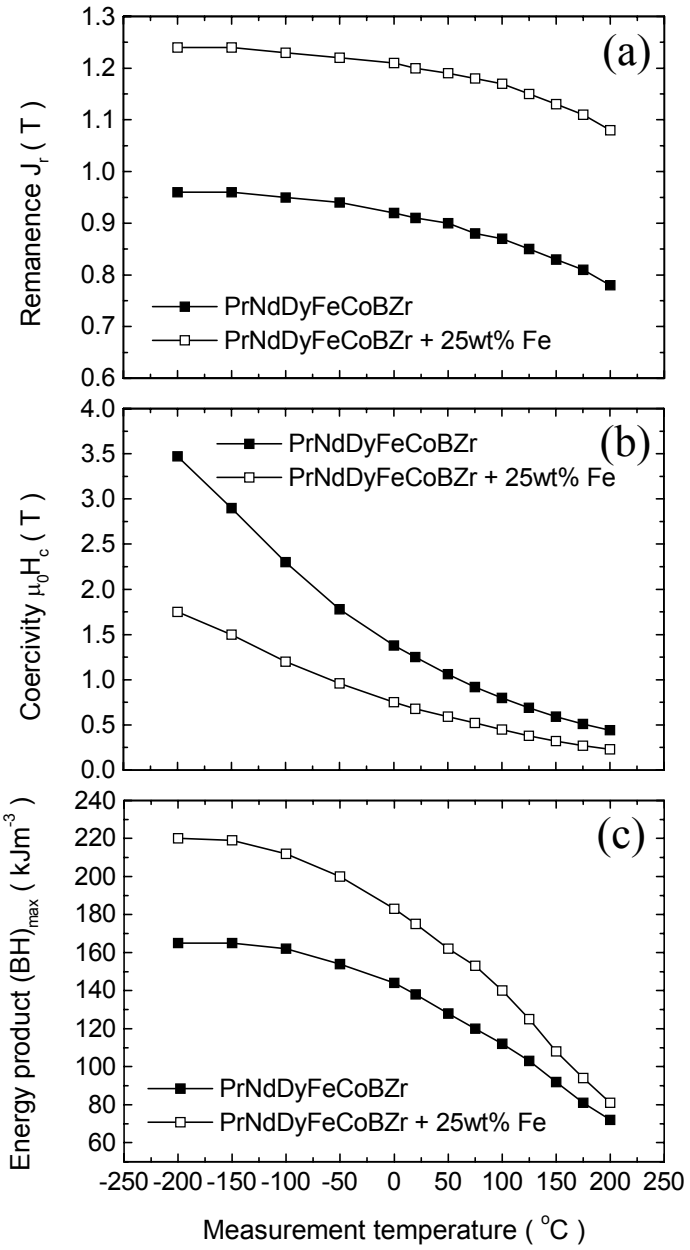

Fig. 8.15: Evolution of (a) remanence; (b) coercivity and (c) energy product $(BH)_{max}$ in dependence on the measurement temperature for milled and annealed (T_a = 600°C) $Pr_{9.0}Nd_{3.0}Dy_{1.0}Fe_{72.0}Co_{8.0}B_{6.9}Zr_{0.1}$ and $Pr_{9.0}Nd_{3.0}Dy_{1.0}Fe_{72.0}Co_{8.0}B_{6.9}Zr_{0.1}$ + 25wt.% α-Fe.

nanocomposite magnet (x = 25) in the whole temperature range due to the superior remanences exhibited by this latter material. The difference in $(BH)_{max}$ between both materials becomes smaller with increasing temperature because of the low $\mu_0 H_c$ values. Similar tendencies were obtained by Goll *et al* [16] for a series of exchange-coupled PrFeB-based alloys produced by melt-spinning.

The absence of spin reorientation in PrFeB makes it interesting to study the differences between the magnetic properties at room temperature and at low temperatures in more detail. The corresponding major demagnetisation curves for PrNdDyFeCoBZr and PrNdDyFeCoBZr + 25 wt.% α-Fe are shown in Fig. 8.16. The increase of the anisotropy field and the coercivity of the hard magnetic phase with decreasing temperature is clearly reflected in the evolution of the plotted data. The anomalous behaviour of the nanocomposite magnet at low temperatures must be noted [16]. The slight shoulder present in the demagnetisation curves, for temperatures lower than –100ºC, is indicative of a two-step demagnetisation behaviour which can be explained considering the temperature dependence of the exchange length. As it was already mentioned in Section 3.1.2, an optimum grain size of the soft magnetic phase must be of the order of $\delta_w \approx \pi(A/K_1)^{1/2}$ for an effective exchange-coupling between the hard and the soft magnetic grains [32,36]. The increase of K_1 with decreasing temperature leads to a smaller value of δ_w (see Fig. 4.6) and, as a consequence, there is a shift of the grain size necessary for an effective exchange-coupling to smaller values. The result is that the larger soft grains will not be as well coupled as they are at room temperature. In this way, the first step in the demagnetisation curve would correspond to the larger soft magnetic grains which reverse independently, whereas the second step, at larger fields, would be due to the reversal of the exchange-coupled grains.

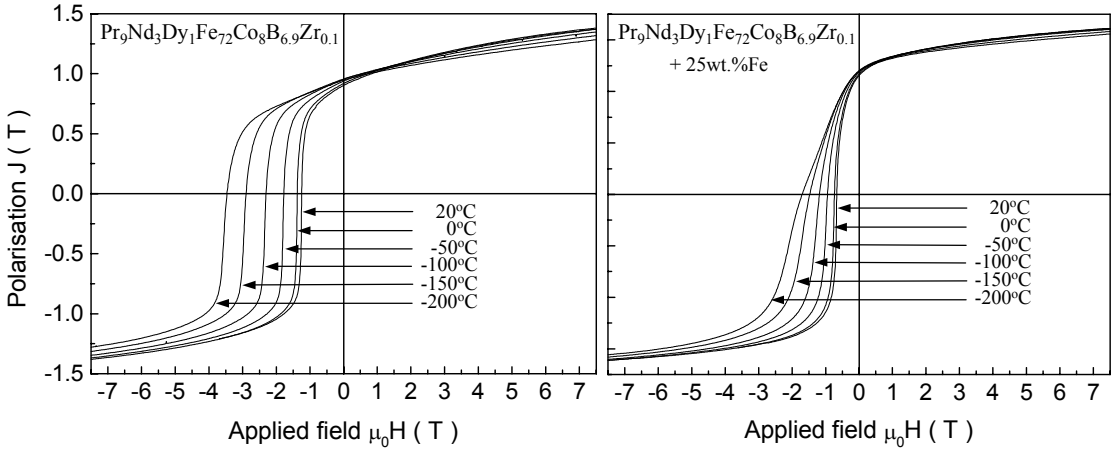

Fig. 8.16: Demagnetisation curves of milled and annealed (T_a = 600ºC) $Pr_{9.0}Nd_{3.0}Dy_{1.0}Fe_{72.0}Co_{8.0}B_{6.9}Zr_{0.1}$ (left) and $Pr_{9.0}Nd_{3.0}Dy_{1.0}Fe_{72.0}Co_{8.0}B_{6.9}Zr_{0.1}$ + 25wt.% α-Fe (right) measured at different temperatures.

In order to understand the temperature dependence of the "exchange-spring" behaviour, inner recoil loops during demagnetisation have been measured at –200ºC (see Fig. 8.17) and compared with those measured at 20ºC (see Fig. 8.6). Recoil loops for $Pr_{9.0}Nd_{3.0}Dy_{1.0}Fe_{72.0}Co_{8.0}B_{6.9}Zr_{0.1}$ are completely closed at –200ºC whereas they are slightly open at 20ºC. This can be explained by considering the small amount of soft magnetic phase present in the sample in combination with the reduction in the exchange length with decreasing temperature. The result is a decreased volume fraction of the exchange-coupled hard/soft regions (in addition to that of the hard/hard regions) obtaining

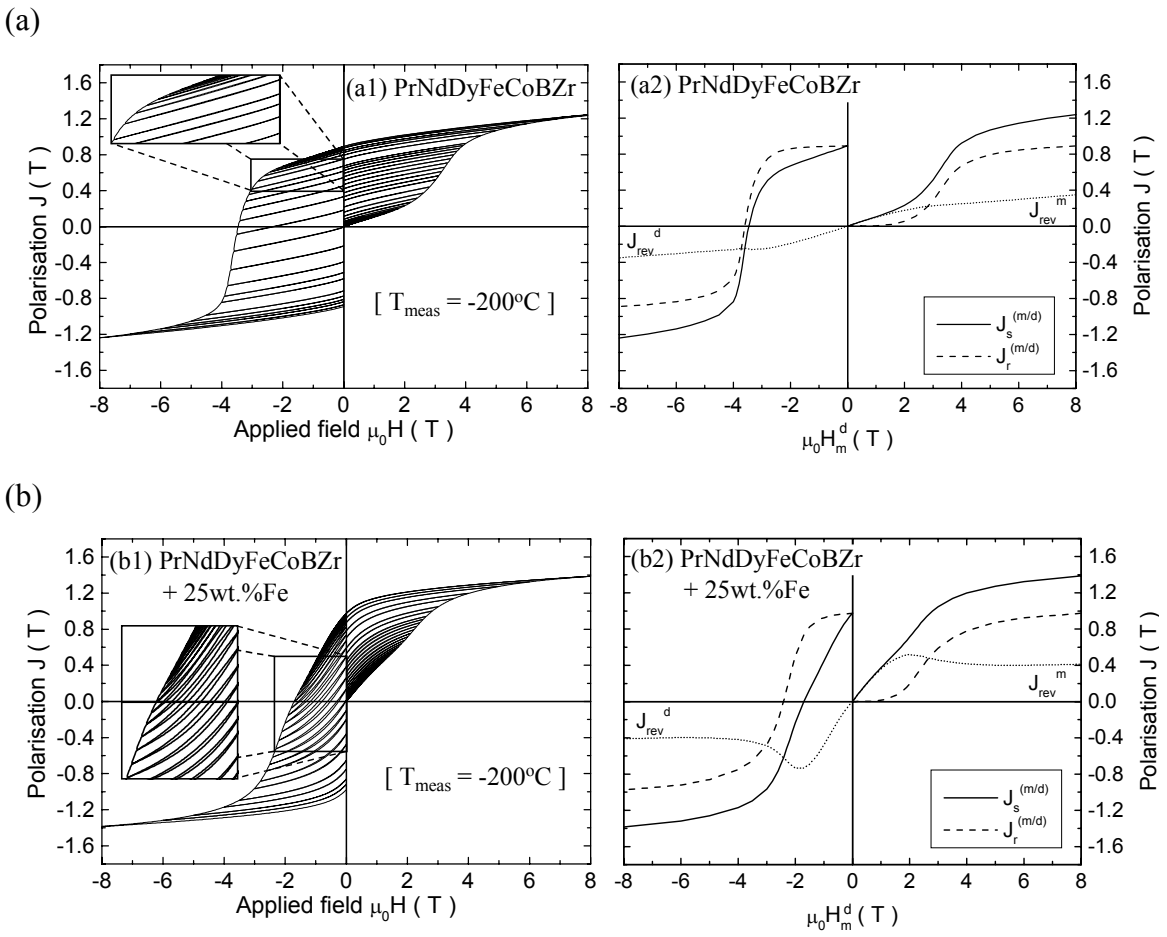

Fig. 8.17: Measurements at –200ºC of $Pr_{9.0}Nd_{3.0}Dy_{1.0}Fe_{72.0}Co_{8.0}B_{6.9}Zr_{0.1}$ (top) and $Pr_{9.0}Nd_{3.0}Dy_{1.0}Fe_{72.0}Co_{8.0}B_{6.9}Zr_{0.1}$ + 25 wt.%Fe (bottom) milled and annealed at T_a=600ºC. Plots of: (left) initial magnetisation and demagnetisation curves including recoil loops; (right) total polarisation during major magnetisation (m) and demagnetisation (d) curves, $J_s^{(m/d)}(H_m)$, remanent polarisation, $J_r^{(m/d)}(H_m)$, and the difference between both amounts, $J_{rev}^{(m/d)}(H_m)$, which is associated to reversible rotation of the magnetic moments during application of the field H_m^d.

the characteristic closed recoil loops observed for single-phase magnets (as those observed for this material after annealing at 700ºC (Fig. 8.12(a1)), in that case due to the complete solution of the residual soft phase in the $R_2T_{14}B$). In the case of the nanocomposite $Pr_{9.0}Nd_{3.0}Dy_{1.0}Fe_{72.0}Co_{8.0}B_{6.9}Zr_{0.1}$ + 25wt.% α-Fe powders, recoil loops at –200ºC are less open than those at 20ºC due to the mentioned reduction of the exchange length with decreasing temperature.

Additionally, it must be noted that, first, an applied field of 8 T is not sufficient to saturate the samples and, second, the remanent polarisation during magnetisation, J_r^m , keeps increasing significantly at the highest applied field. This means that there exists a remarkable difference to the measurements performed at 20ºC where J_r^m was saturated for applied fields significantly lower than 8 T (see Figs. 8.6b,e). The conclusion is that, after applying a field of 8 T at –200ºC, there is still a significant fraction of magnetic moments which have not been irreversibly rotated into the field direction.

The field dependences of the $m_{rev} = J_{rev} / J_r$ curves derived from the recoil curves at –200 and 20 ºC are shown in Fig. 8.18. The m_{rev} values for the single alloy at –200ºC are lower than those at 20ºC for any reversed applied field. This behaviour can be understood considering the increase of the anisotropy constant K_1 of the hard magnetic phase with decreasing temperature: a reduction in δ_w leads to a larger contribution of the soft phase to the reversible portion but, on the other hand, it causes a large increase of the anisotropy field. This second effect is predominant at any applied field due to the small amount of soft magnetic phase present in the sample. The decreased exchange length leads to partly decoupled regions in the hard magnetic grains which can be irreversibly reversed at lower fields than the exchange-coupled regions. This would explain the fact that the remanent coercivity, H_r, is lower than the corresponding nucleation field for irreversible rotation of the exchange-coupled hard phase, H_{no} (see Table 8.4). In contrast to the behaviour observed for the single-phase alloy, an increase of the maximum value of the m_{rev} curve is observed for $Pr_{9.0}Nd_{3.0}Dy_{1.0}Fe_{72.0}Co_{8.0}B_{6.9}Zr_{0.1}$ + 25wt.% α-Fe with decreasing temperature. It must be noted by comparison with the single phase alloy, first, a smaller difference between the corresponding m_{rev} values at –200ºC and those at 20ºC for low reversed fields; second, the m_{rev} values at low temperature become larger than those at 20ºC at $\mu_0 H_m^d \approx 1$ T. This is attributed to a larger fraction of Fe moments in the soft grains

participating in the reversible portion for reverse fields smaller than the switching field of the hard phase. Thus, beginning of irreversible rotation is expected to take place first in the exchange-coupled regions. In fact, determination of the critical fields, H_{no} and H_r, shows in good agreement that $H_{no} < H_r$ (see Table 8.4).

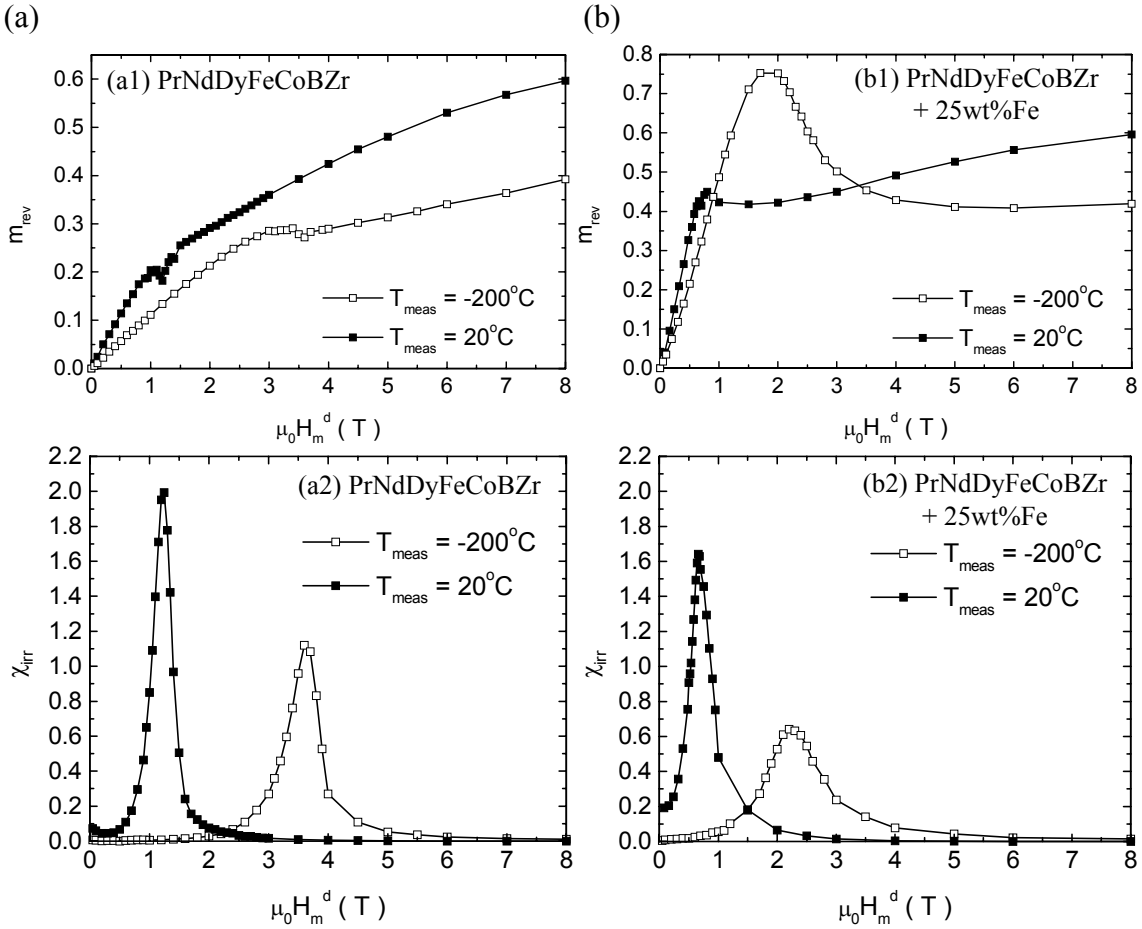

Fig. 8.18: Measurements at –200°C and 20°C of (a) $Pr_{9.0}Nd_{3.0}Dy_{1.0}Fe_{72.0}Co_{8.0}B_{6.9}Zr_{0.1}$ and (b) $Pr_{9.0}Nd_{3.0}Dy_{1.0}Fe_{72.0}Co_{8.0}B_{6.9}Zr_{0.1}$ + 25wt.% α-Fe milled and annealed at T_a=600°C. Top: reversible reduced portion, $m_{rev} = J_{rev}^{d} / J_r$, and bottom: irreversible susceptibility defined as $\chi_{irr} = dm_{irr} / dH$ in T^{-1}, where m_{irr} is the normalised irreversible polarisation ($m_{irr} = J_{irr} / J_r$), vs. the applied reverse field.

Sample	$\mu_0 H_c$ (T)	$\mu_0 H_{no}$ (T)	$\mu_0 H_r$ (T)
PrNdDyFeCoBZr (x=0)	3.45	3.65	3.59
x = 25 wt.% α-Fe	1.68	2.24	2.40

Table 8.4: Measurements at –200°C of coercivity, $\mu_0 H_c$ (T); nucleation field, $\mu_0 H_{no}$ (T) and remanence coercivity, $\mu_0 H_r$ (T), for milled and annealed (600°C) $Pr_{9.0}Nd_{3.0}Dy_{1.0}Fe_{72.0}Co_{8.0}B_{6.9}Zr_{0.1}$ and $Pr_{9.0}Nd_{3.0}Dy_{1.0}Fe_{72.0}Co_{8.0}B_{6.9}Zr_{0.1}$ + 25wt.% α-Fe powders.

The δJ plots for $Pr_{9.0}Nd_{3.0}Dy_{1.0}Fe_{72.0}Co_{8.0}B_{6.9}Zr_{0.1}$ and $Pr_{9.0}Nd_{3.0}Dy_{1.0}Fe_{72.0}Co_{8.0}B_{6.9}Zr_{0.1}$ + 25wt.% α-Fe at –200ºC are shown, together with those at 20ºC for comparison, in Figs. 8.19a,b, respectively. An expected shift of the curves to higher values of the reversed field is observed when the temperature is decreased. The almost symmetrical shape of the δJ curve for the single-phase alloy at 20ºC is deteriorated at –200ºC resulting in smaller negative values for δJ. This points to a lower contribution of the exchange interactions mainly due to the reduced exchange-coupling resulting from the temperature dependence of the exchange length. The same effect on δJ has been also found for the nanocomposite material. Additionally, a local minimum can be observed at –200ºC for low reversed fields which is not present at 20ºC. This could be interpreted as the result of the combined effects of magnetostatic and exchange interactions, the first ones starting to play a significant role at the lower temperature as a consequence of the reduced exchange-coupling between the different grains.

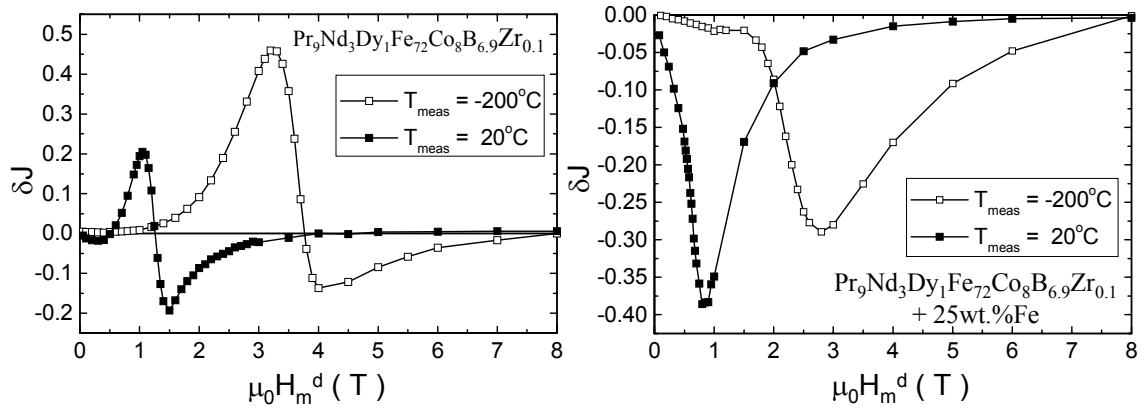

Fig. 8.19: Deviation of demagnetisation remanence, δJ, as function of the applied field for milled and annealed (600°C) $Pr_{9.0}Nd_{3.0}Dy_{1.0}Fe_{72.0}Co_{8.0}B_{6.9}Zr_{0.1}$ and $Pr_{9.0}Nd_{3.0}Dy_{1.0}Fe_{72.0}Co_{8.0}B_{6.9}Zr_{0.1}$ + 25wt.% α-Fe powders measured at -200 and 20 °C.

8.4 Summary

The important differences in the magnetisation behaviour of decoupled and exchange-coupled (nearly single-phase and two-phase) materials have been studied by comparison of their respective magnetisation curves.

An analysis of the initial magnetisation curves for milled-and-annealed thermally demagnetised samples has shown significant differences depending on the microstructure. An inhomogeneous microstructure consisting of large and small grains for a decoupled ternary PrFeB alloy has been shown to be responsible for a complicated magnetisation process. A fraction of grains in a multi-domain state as well as grains in a single-domain state could be the reason for an observed two-step magnetisation process. The optimally annealed exchanged-coupled materials have exhibited, however, a more simple shape of the initial magnetisation curve. A very homogeneous microstructure consisting of very fine grains with sizes below the critical single-domain size makes definitely not possible to attribute that behaviour to classical domain-wall processes but interaction domains may, however, be relevant.

Recoil loops of the nanocomposite magnets are relatively open whereas those of the Pr-rich and single-phase alloys are closed. Open recoil loops result from the reversible rotation of the exchange-coupled soft phase for fields not large enough to reverse the magnetisation of the hard magnetic phase. These remanence enhanced nanocomposites consisting of hard and soft phases exhibit exchange-spring magnet behaviour, namely, high values of reversible susceptibility for magnetic fields below coercivity along the demagnetisation curve. An analysis of the deviations, δJ, from the theoretical value for the remanent polarisation given by Wohlfarth's relation gives information on the intergrain interactions during the demagnetisation process. Plots of δJ when varying the α-Fe content show that an increased amount of soft magnetic phase, effectively exchange-coupled to the hard phase, results in more negative δJ values, indicative of the stronger exchange interactions. In contrast, a decoupled ternary alloy exhibits exclusively positive δJ values which could be associated to dominant magnetostatic interactions between the hard magnetic grains. The effect of the annealing temperature and the measurement temperature show good agreement with the given description for the evolution of δJ. Increased annealing temperatures result in reduced negative deviations, pointing to magnetostatic interactions to be predominant, as a result of the decreased effectiveness of the exchange-coupling between the grains with increasing mean sizes. A similar effect is observed by decreasing the measurement temperature as a consequence of the reduction of the exchange length which results in a decreased exchange-coupling.

9 Reactive milling in hydrogen

Gas-solid reactions of R-T compounds with hydrogen are an alternative route to mechanical alloying, intensive milling or rapid quenching for the preparation of amorphous or nanocrystalline materials [5]. The HDDR process is well established as a method for production of highly coercive $Nd_2Fe_{14}B$ and $Sm_2Fe_{17}N_y$ magnets [101,111,112]. Recent studies have been focused on HDDR PrFeB-type processed alloys [113-115]. The HDDR process is based on a reversible hydrogen-induced phase transformation as described in Section 5.1.3. The reactive milling procedure consists of ball milling at enhanced hydrogen pressure and temperature; this is followed by vacuum annealing to ensure the full desorption of hydrogen and a recombination of the intermetallic phase.

Nd forms dihydrides with fcc structure. The absorption of extra hydrogen forms the trihydride without any change of structure [116]. The absorption of hydrogen by the $Nd_2Fe_{14}B$ phase results in the $Nd_2Fe_{14}BH_x$ hydride. The hydride retains the same structure as the original $Nd_2Fe_{14}B$ starting material when moderate charging conditions are employed. An isotropic expansion in the *a* and *c* directions is inferred from the fact that the *c*/*a* value for the hydride remains the same as that for the original structure [78,117].

This study begins with the analysis of the structural changes after different stages of $Pr_{14.7}Fe_{77.3}B_{8.0}$ (alloy (8)) processed by reactive milling. The magnetic properties on desorption are shown and compared with the properties of the alloy after milling in Ar and subsequent annealing (see Section 6.1.3).

In the second part, $Nd_2(Fe,Co)_{14}B$-based alloys processed by this technique are studied. When Fe is substituted by Co in the $R_2T_{14}B$ phase, the absorption of hydrogen is less, which can be attributed to a higher stability of the $Nd_2Co_{14}B$ compound and more specifically to a decrease of the unit cell volume. Consistent with this reduced amount of absorbed hydrogen, Fujita and Harris [78] observed that high Co content compounds exhibit a smaller lattice expansion (see Fig. 9.1). They produced the hydrides by heating under a hydrogen pressure of 1 bar until absorption was completed and then cooled to room temperature. It can be observed again that the *c/a* value for the hydride remains approximately the same as that for the original structure.

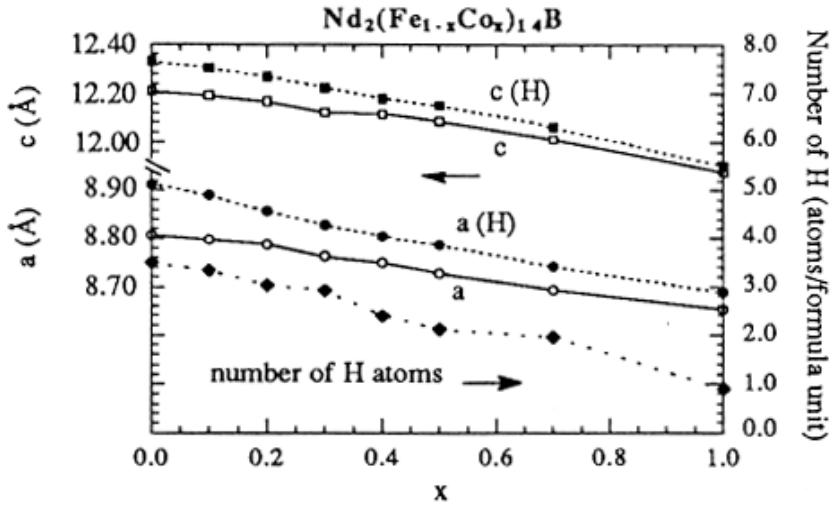

Fig. 9.1: Dependence of the lattice parameters of the $Nd_2(Fe_{1-x}Co_x)_{14}B$ compounds and their hydrides on Co content. Circles and squares represent the a and c parameters of the 2:14:1 tetragonal unit cell, respectively. Solid circles and squares are those of the hydrides. Diamonds are the number of absorbed hydrogen atoms per formula unit, evaluated from the difference of the pressure before and after absorption (from Fujita and Harris [78]).

The main problem of substituting Fe by Co is the thermodynamic stabilisation of the parent compound which essentially makes the disproportionation by hydrogen absorption and thus, the application of the conventional-HDDR process, impossible [78]. Figure 9.2 shows by means of a temperature-pressure-analysis (TPA) that in the case of more than 70% Co substitution, there is no evidence of a disproportionation reaction.

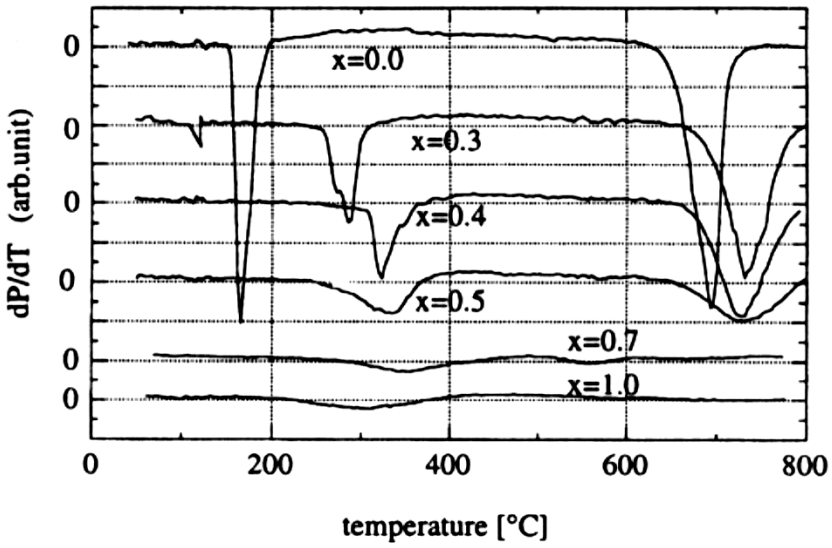

Fig. 9.2: Hydrogen pressure changes in the sample chamber of a TPA system for $Nd_2(Fe_{1-x}Co_x)_{14}B$ ingots as a function of temperature (from Fujita and Harris [78]).

Compounds such as Sm_2Co_{17} and $Sm_2Fe_{17-x}Ga_x$ ($0 \leq x \leq 2$), which are thermodynamically more stable than the $Nd_2Fe_{14}B$ and Sm_2Fe_{17}, can be disproportionated by reactive milling [101,102] and high-hydrogen-pressure disproportionation [118,119].

9.1 Reactive milling of a $Pr_{14.7}Fe_{77.3}B_{8.0}$ alloy

A compound with the starting composition $Pr_{14.7}Fe_{77.3}B_{8.0}$ has been reactively milled and subsequently annealed under different conditions to analyse the evolution of the different phases during the recombination process. Structural changes and the evolution of magnetic properties on desorption have been studied. Similar studies performed on the same alloy but processed by the intensive milling technique (see Sections 6.2 and 6.3) allow to make a comparison of the magnetic properties of the resulting powders after annealing.

9.1.1 Structural changes throughout the different processing stages

Reactive milling of $Pr_{14.7}Fe_{77.3}B_{8.0}$ for 20 h leads to the disproportionation of the $Pr_2Fe_{14}B$ phase into a mixture of $PrH_{2+\delta}$ and bcc-Fe. Additionally, a small amount of $Pr_{1.1}Fe_4B_4$ is observed throughout the different processing stages in the XRD patterns of Fig. 9.3. Subsequent annealing at 450ºC for 10 min is not sufficient for the recombination reaction to take place. The hydrogen desorption of the disproportionated material was observed by monitoring the pressure during heating the sample at a rate of 10 $Kmin^{-1}$ in vacuum and under continuous pumping. The desorption behaviour is shown in Fig. 9.4. The low temperature peak (A) is attributed to the desorption of the over-stoichiometric hydrogen of $PrH_{2+\delta}$. The onset temperature T_s (indicated by an arrow) of the recombination reaction (peak B) is about 525ºC. In good agreement with this last result, annealing at 600ºC for 10 min gives rise to the beginning of the desorption and simultaneous recombination of the $Pr_2Fe_{14}B$ phase. The corresponding XRD pattern (Fig. 9.3) shows the coexistence of $PrH_{2+\delta}$, bcc-Fe and $Pr_2Fe_{14}B$ ($Pr_{1.1}Fe_4B_4$ cannot be distinguished due to the overlapping of the corresponding intensity peaks with those of $Pr_2Fe_{14}B$). Annealing at higher temperatures or longer times than 30 min at 600ºC results in the complete recombination of the material to the original phase.

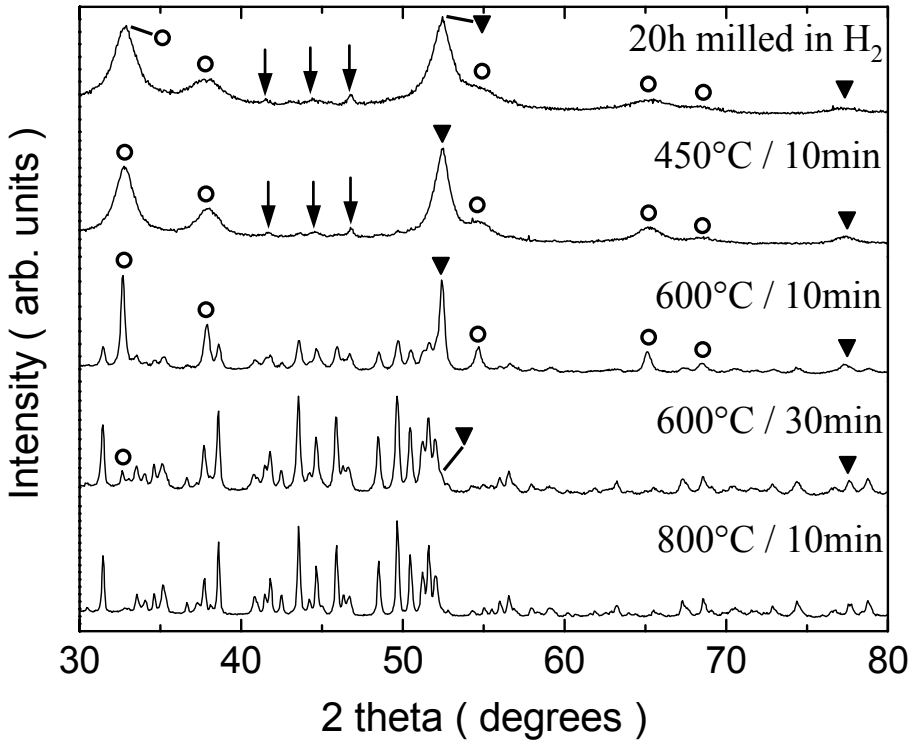

Fig. 9.3: XRD patterns of $Pr_{14.7}Fe_{77.3}B_{8.0}$ after different processing steps: milled in hydrogen and milled-and-annealed in vacuum at various temperatures / times. Markers indicate the main reflection peaks of $PrH_{2+\delta}$ (circles), α-Fe (triangles) and $Pr_{1.1}Fe_4B_4$ (arrows). The non-labelled peaks correspond to the $Pr_2Fe_{14}B$ phase.

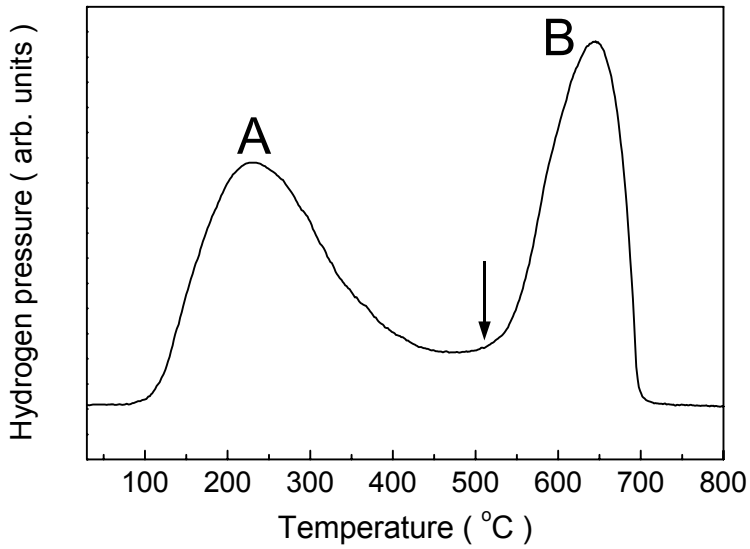

Fig. 9.4: Desorption behaviour of reactively milled $Pr_{14.7}Fe_{77.3}B_{8.0}$ powders on heating in vacuum (10 $Kmin^{-1}$ under continuous pumping); the first peak (A) corresponds to the desorption of the over-stoichiometric hydrogen from $PrH_{2+\delta}$ and the arrow indicates the onset temperature of the recombination reaction (B), T_s.

9.1.2 Evolution of magnetic properties on desorption

The highest coercivity, $\mu_0 H_c$ =1.40 T, is achieved after annealing at 700ºC due to a complete recombination of the $Pr_2Fe_{14}B$ without any residual amount of $PrH_{2+\delta}$ or bcc-Fe detected by XRD. Figure 9.5 shows the initial magnetisation and demagnetisation curves after annealing at three different temperatures. Table 9.1 shows the magnetic properties for $Pr_{14.7}Fe_{77.3}B_{8.0}$ processed by reactive milling in hydrogen and intensive milling in argon, after annealing at 600, 700 and 800 ºC. The differences in coercivity between the two different processing routes can be attributed to the effect of the extreme conditions used during reactive milling on the final nanostructure. Further investigations must be undertaken in this way. It must be remarked the absence of any oxide after the different processing steps.

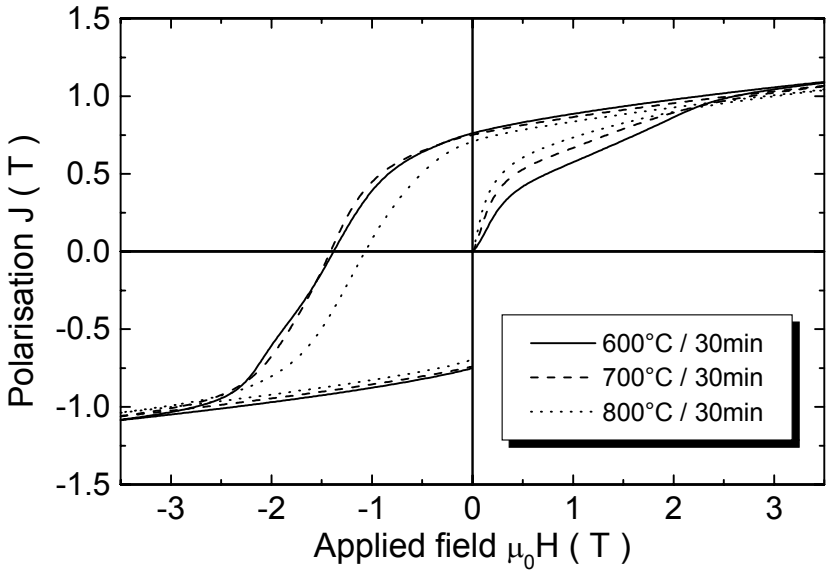

Fig. 9.5: Initial magnetisation and demagnetisation curves of reactively milled and recombined $Pr_{14.7}Fe_{77.3}B_{8.0}$ powders after annealing at 600, 700 and 800 ^oC (introduced into the pre-heated furnace).

Processing route	$\mu_0 H_c$ (T)	J_r(T)	$(BH)_{max}$ (kJm^{-3})
RM + 600°C/30min	1.37	0.76	94
RM + 700°C/30min	1.40	0.75	95
RM + 800°C/30min	1.07	0.71	77

Processing route	$\mu_0 H_c$ (T)	J_r(T)	$(BH)_{max}$ (kJm^{-3})
IM + 600°C/30min	1.81	0.75	97
IM + 700°C/30min	1.78	0.74	96
IM + 800°C/30min	0.98	0.69	72

Table 9.1: Comparison of magnetic properties for reactively milled (RM)-and-recombined $Pr_{14.7}Fe_{77.3}B_{8.0}$ powders (top) and intensively milled (IM)-and-annealed $Pr_{14.7}Fe_{77.3}B_{8.0}$ powders (bottom). Optimum processing conditions are marked in bold.

9.2 Reactive milling of $Nd_2(Fe,Co)_{14}B$ alloys

Stoichiometric $Nd_2(Fe_{1-x}Co_x)_{14}B$ alloys (x = 0, 0.25, 0.5, 0.75 and 1) have been reactively milled. The main aim is the disproportionation of the thermodynamically very stable alloys (those with high Co content) via this modified "extreme" HDDR process.

9.2.1 Microstructural characterisation of starting alloys

Figure 9.6 shows the XRD patterns of $Nd_2Fe_{14}B$ and $Nd_2Co_{14}B$ in the as-cast and homogenized states. In the as-cast state, intensity peaks of bcc-Fe and $Nd_2Fe_{14}B$ phases are observed for the former alloy, and fcc-Co, $Nd_2Co_{14}B$ and some minority phases for the latter one. The presence of fcc-Co in this latter alloy (instead of the hcp phase) can be ascribed to a non-equilibrium process taking place during fabrication of the alloy. Identification of the minority phases is difficult due to the low intensity of the reflections and their overlapping. After homogenisation, only the $R_2T_{14}B$ phase is observed for both samples. The patterns of the three intermediate alloys (x = 0.25, 0.5 and 0.75) in the as-cast form show intensity peaks of a soft magnetic FeCo-phase and the hard magnetic $R_2T_{14}B$ phase, besides minority phases, and again after homogenisation only the $R_2T_{14}B$ phase. This is in good agreement with the corresponding SEM results which show, in addition to the mentioned phases for the as-cast alloys, a Nd-rich phase in the case of the two first samples (x = 0 and 0.25), again a Nd-rich phase and $Nd(Fe,Co)_3$ for the alloys where 50 and 75 at.% Fe are substituted, and $NdCo_3$ and some tiny spots of fcc-Co for $Nd_2Co_{14}B$.

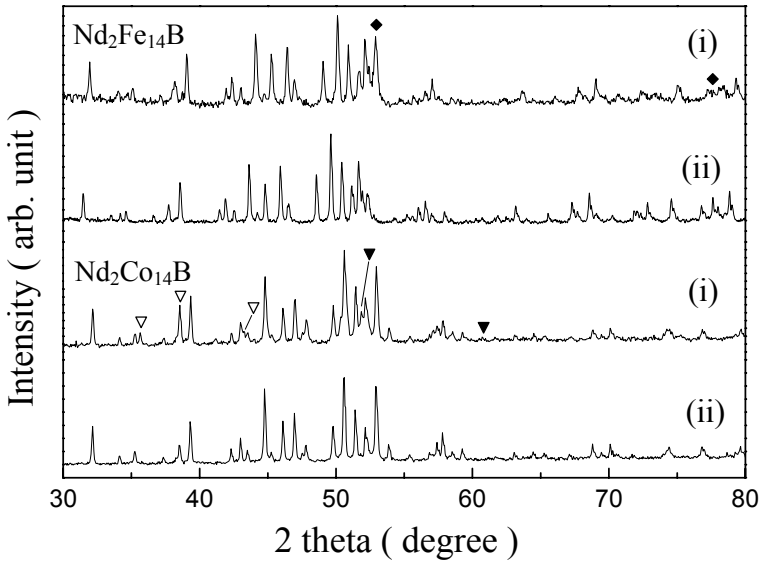

Fig. 9.6: XRD patterns of $Nd_2Fe_{14}B$ and $Nd_2Co_{14}B$ in the as-cast (i) and homogenised (ii) states. Reflections of bcc-Fe (◆) and fcc-Co (▼), besides some minority phases for $Nd_2Co_{14}B$ (▽), can be seen in the patterns of the as-cast samples. After homogenisation, only 2:14:1 peaks are present.

As an example, the SEM micrographs in the backscattered mode of the $Nd_2Fe_{14}B$, $Nd_2(Fe_{0.5}Co_{0.5})_{14}B$ and $Nd_2Co_{14}B$ alloys in the as-cast state and after homogenisation are shown in Fig. 9.7. The first micrograph (Fig. 9.7a) shows the typical view for a stoichiometric $Nd_2Fe_{14}B$-type alloy in the as-cast condition [78,117]: significant amounts of primary Fe dendrites (1) and Nd-rich material (2) within the 2:14:1 matrix phase (3). After homogenisation (see Fig. 9.7b) there is practically only 2:14:1 phase, with a small residual amount of free α-Fe. The microstructures of the as-cast and homogenised $Nd_2(Fe_{0.5}Co_{0.5})_{14}B$ and $Nd_2Co_{14}B$ alloys are shown in the micrographs of Figs. 9.7c-f. In the high magnification micrographs of the as-cast sample, the different phases present are indicated. It is interesting to note that now the free Co is not localised as dendrites, like bcc-Fe in the case of the $Nd_2Fe_{14}B$ alloy. Additionally, the volume fraction of the free Fe or FeCo is significantly decreased with increasing the Co-content. In this way, it is not surprising that the homogenisation works better for the $Nd_2Co_{14}B$ alloy: 2:14:1 phase and only a really insignificant amount of free Co (not detected by X-rays) can be observed (Fig. 9.7f).

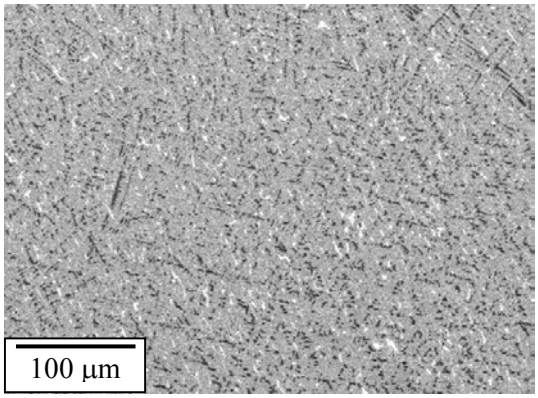

(a) $Nd_2Fe_{14}B$ as-cast

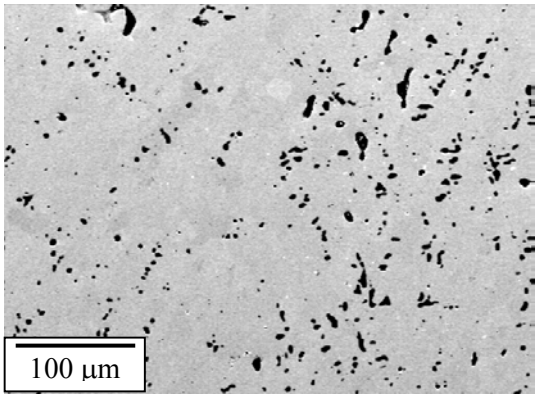

(b) $Nd_2Fe_{14}B$ homogenised

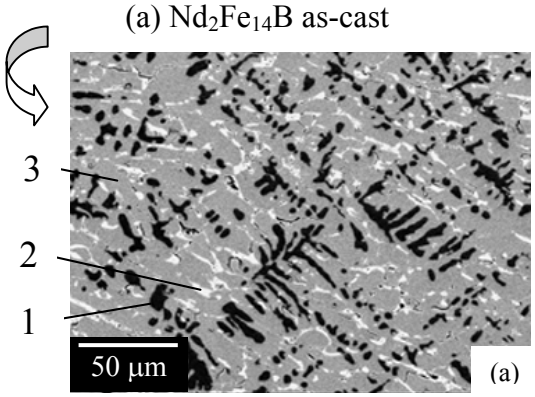

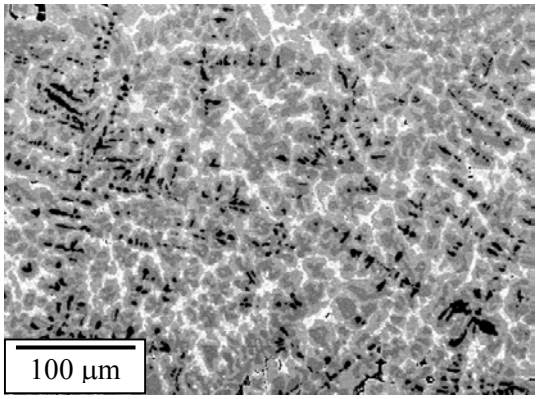

(c) $Nd_2(Fe_{0.5}Co_{0.5})_{14}B$ as-cast

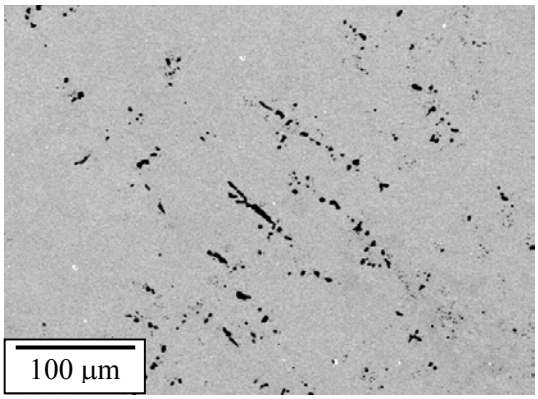

(d) $Nd_2(Fe_{0.5}Co_{0.5})_{14}B$ homogenised

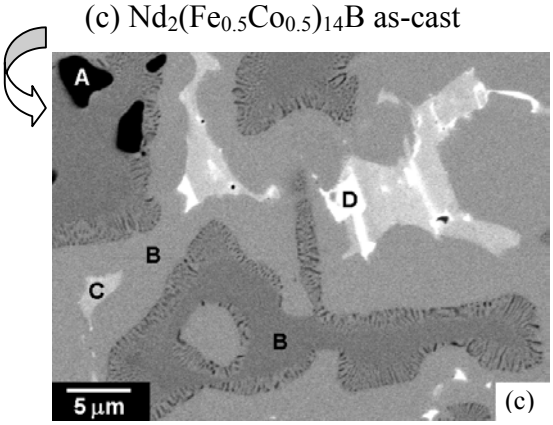

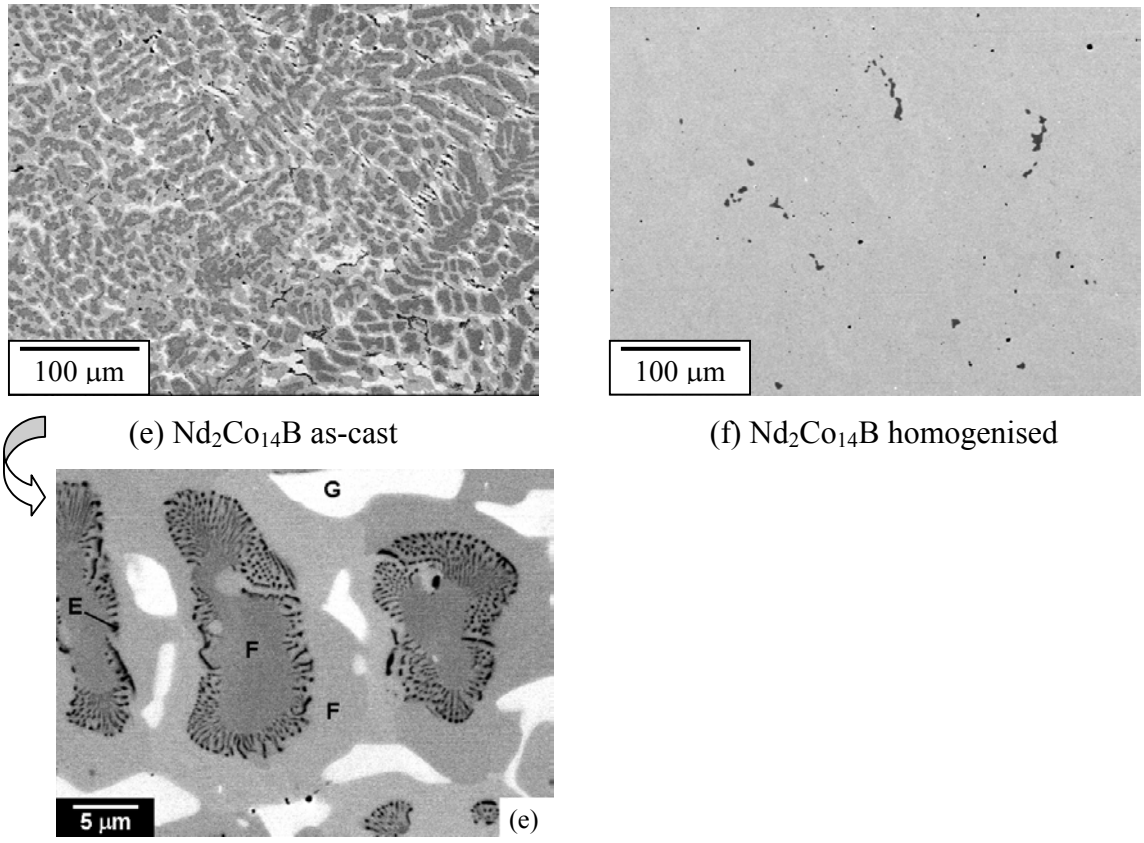

Fig. 9.7: SEM micrographs of (a) $Nd_2Fe_{14}B$, (b) $Nd_2(Fe_{0.5}Co_{0.5})_{14}B$ and (c) $Nd_2Co_{14}B$ in the as-cast and homogenised states. Phases distinguishable by EDX analysis in the as-cast condition: (a) $Nd_2Fe_{14}B$: Fe dendrites (1), Nd-rich phase (2) and 2:14:1 matrix phase (3); (c) $Nd_2(Fe_{0.5}Co_{0.5})_{14}B$: bcc-(Fe,Co) (A), $Nd_2(Fe,Co)_{14}B$ (B), $Nd(Fe,Co)_3$ (C) and a Nd-rich phase (D); (e) $Nd_2Co_{14}B$: fcc-Co (E), $Nd_2Co_{14}B$ (F) and $NdCo_3$ (G). After homogenisation (see b,d and f) only 2:14:1 phase, with a small residual amount of free Fe or FeCo (dark regions), can be detected.

9.2.2 Effect of Co-content on density and Curie temperature

The dependence of the density and the Curie temperature of $Nd_2(Fe_{1-x}Co_x)_{14}B$ on Co concentration can be seen in Fig. 9.8, where the results from the two different methods, thermal demagnetisation and magnetic balance, have been plotted. These Curie temperature values are in good agreement with other studies [80,81], and it can be seen that it rises from T_C = 312°C for $Nd_2Fe_{14}B$ to 722°C for $Nd_2Co_{14}B$.

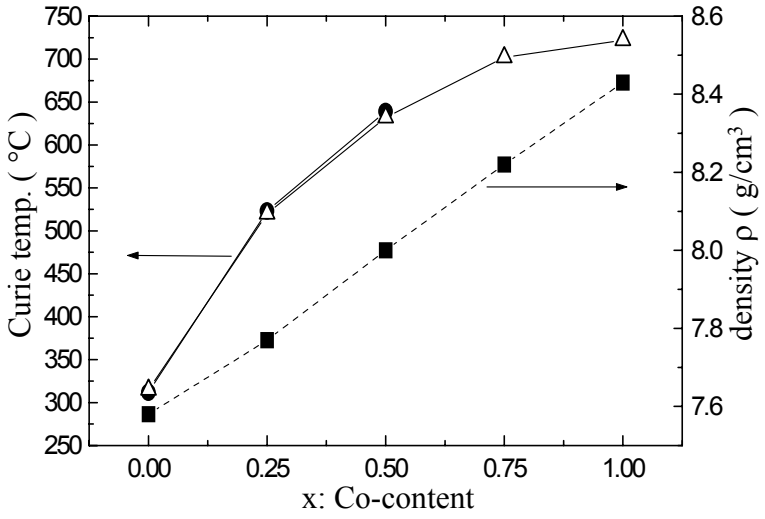

Fig. 9.8: Dependence of the density (squares) and the Curie temperature of $Nd_2(Fe_{1-x}Co_x)_{14}B$ on Co concentration. Curie temperatures measured by thermal demagnetisation (circles) and magnetic balance (triangles) are plotted.

9.2.3 Disproportionation by reactive milling

Figure 9.9 shows the XRD patterns of the reactively milled powders. It can be seen that the disproportionation reaction is completed after 20 h of milling in hydrogen for the $Nd_2Fe_{14}B$ alloy. This milling time was not sufficient to completely disproportionate the other four alloys, illustrating the higher thermodynamic stability of the Co-substituted alloys. In the XRD patterns of 20 h reactively milled $Nd_2(Fe_{0.5}Co_{0.5})_{14}B$ and $Nd_2Co_{14}B$ some residual amount of 2:14:1 phase can be detected (higher for the latter one). The reaction is completed for the five alloys, x = 0, 0.25, 0.5, 0.75 and 1, after 20, 25, 30, 35 and 40 hours of milling, respectively. With increasing Co content a shrinkage of the 2:14:1 unit cell is observed [80] and this could affect hydrogen diffusional processes in the bulk as well as the thermodynamic stability of the $R_2T_{14}B$ compound. The increased stability of the $Nd_2(Fe,Co)_{14}B$ parent compounds [78,120] shifts the balance in the equation for the disproportionation (Eq. (5.1)) into the direction of the starting material. Therefore, the reaction with hydrogen, i.e. disproportionation, is less likely. Broad reflections of $NdH_{2+\delta}$ and bcc-Fe, bcc-FeCo or fcc-Co are present in the case of $Nd_2Fe_{14}B$, the three intermediate alloys and $Nd_2Co_{14}B$, respectively (see Fig. 9.9). The grain sizes of the disproportionated materials were estimated by HRTEM to be < 10 nm which is significantly smaller than those of conventionally HDDR processed NdFeB materials [121].

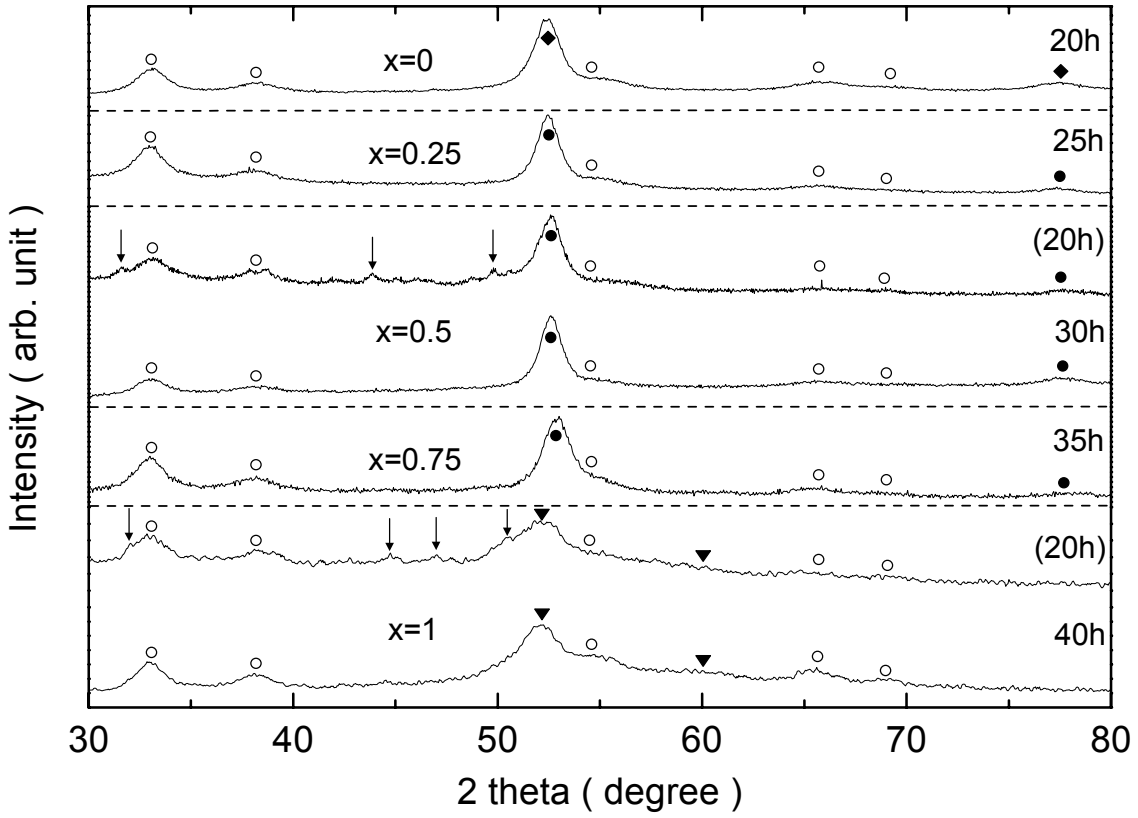

Fig. 9.9: XRD patterns of disproportionated $Nd_2(Fe_{1-x}Co_x)_{14}B$ (x = 0, 0.25, 0.5, 0.75 and 1) after optimum milling times (20, 25, 30, 35 and 40 hours, respectively). Reflections of $NdH_{2+\delta}$ (○), bcc-Fe (◆), bcc-(FeCo) (●) and fcc-Co (▼) are shown. XRD patterns of $Nd_2(Fe_{0.5}Co_{0.5})_{14}B$ and $Nd_2Co_{14}B$ after 20 h of milling show some residual amount of 2:14:1 phase (indicated by arrows).

9.2.4 Desorption and recombination

The desorption behaviour of reactively milled $Nd_2(Fe_{1-x}Co_x)_{14}B$ powders with x = 0 (20 h), x = 0.25 (25 h), x = 0.5 (30 h), x = 0.75 (35 h) and x = 1 (40 h) on heating in vacuum, is shown in Fig. 9.10. In all cases the low temperature peaks (A) are attributed to the desorption of the over-stoichiometric hydrogen of $NdH_{2+\delta}$. As expected from thermodynamic considerations, a decrease in the onset temperature T_s (indicated by arrows) of the recombination reaction (B) is observed for the Co-containing compounds, indicative of their higher thermodynamic stability compared to the Fe based alloy. In this way, T_s decreases from 554°C for $Nd_2Fe_{14}B$ to 460°C for $Nd_2Co_{14}B$. A very low desorption temperature of 380°C for the 20 h milled $Nd_2Co_{14}B$ sample was observed, which is attributed to the incomplete disproportionation resulting in nucleation centers of the

original $R_2T_{14}B$ phase for the recombination reaction. It is also interesting to note that the recombination reaction of the reactively milled $Nd_2Fe_{14}B$ sample takes place at lower temperatures compared to conventionally disproportionated stoichiometric NdFeB material [122]. This could be attributed firstly to the much finer grain size of the reactively milled sample leading to a higher amount of interfaces between $NdH_{2+\delta}$, bcc-Fe and 2:14:1, i.e. more effective sites for the initiation of the recombination reaction and, secondly, to a generally larger and more activated surface area.

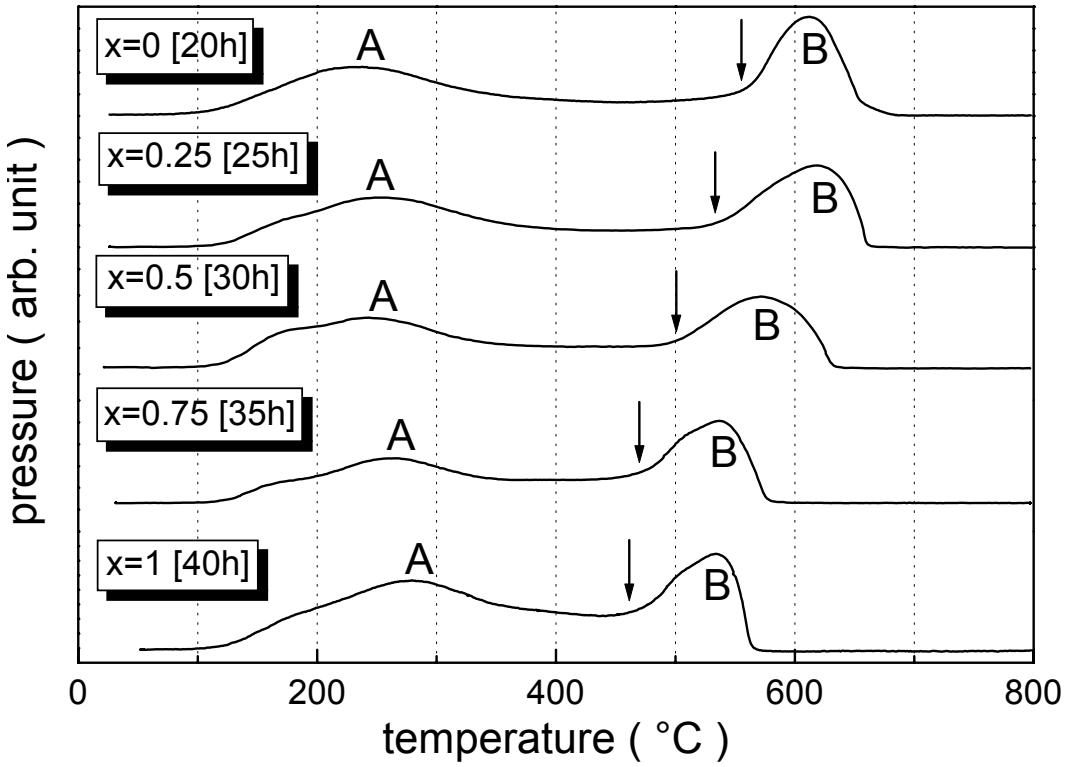

Fig. 9.10: Desorption behaviour of reactively milled $Nd_2(Fe_{1-x}Co_x)_{14}B$ powders (x = 0 (20 h), 0.25 (25 h), 0.5 (30 h), 0.75 (35 h) and 1 (40 h)) on heating in vacuum (10 $Kmin^{1}$); the first peak (A) corresponds to the desorption of the over-stoichiometric hydrogen from $NdH_{2+\delta}$. Arrows indicate the onset temperature of the recombination reaction (B), T_s.

The XRD patterns of the reactively milled and annealed $Nd_2Fe_{14}B$ and $Nd_2Co_{14}B$ materials show that both can be recombined successfully to the original phases, now with reflections of minor amounts of bcc-Fe and fcc-Co, respectively (see Fig. 9.11). Lower annealing temperatures lead to broadened diffraction peaks indicative of smaller grain sizes. In addition, it should be pointed out that $Nd_2Co_{14}B$ can be recombined at

temperatures as low as 550°C whereas for the former material a minimum temperature of 600°C is required.

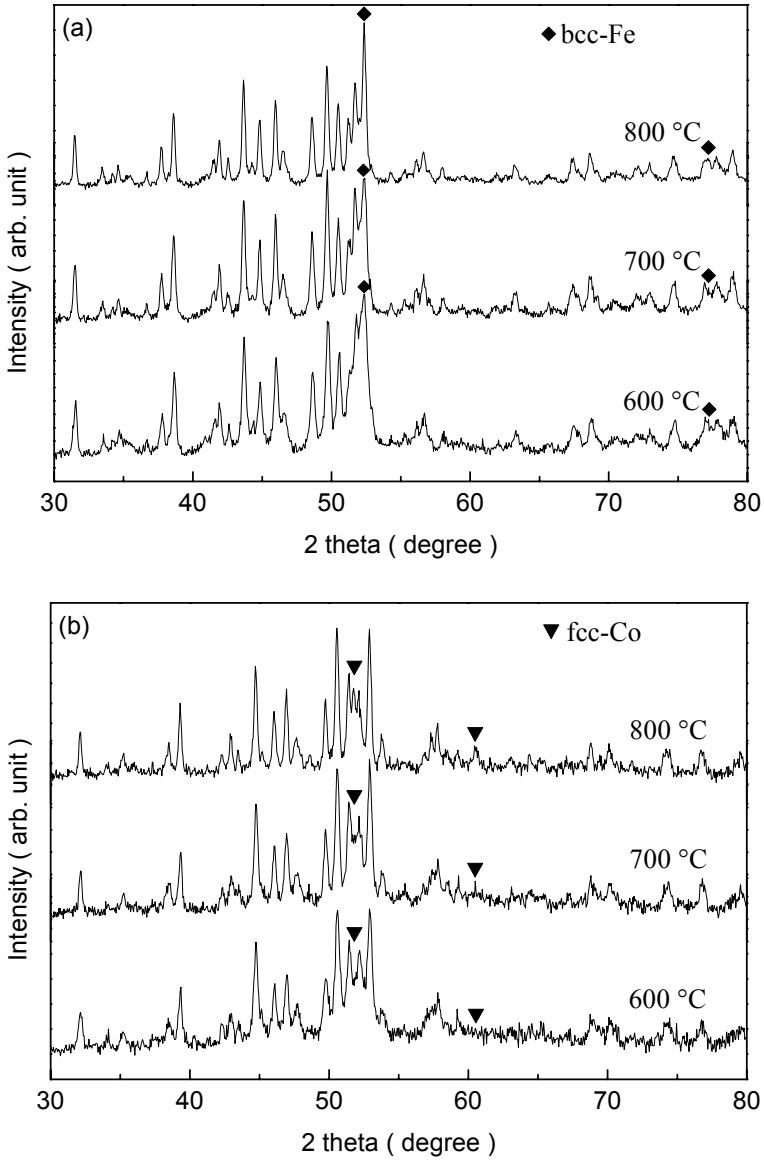

Fig. 9.11: XRD patterns of (a) $Nd_2Fe_{14}B$ and (b) $Nd_2Co_{14}B$ powders recombined by annealing in vacuum for 30 min at various temperatures. Reflections of bcc-Fe (◆)*, for the former alloy, and fcc-Co* (▼)*, for the latter one, are shown.*

9.2.5 Average grain size

The grain sizes of the recombined materials, determined from XRD patterns, are shown in Fig. 9.12. It can be seen that they are in the range of 40-50 nm for a 600°C

annealing – approximately in the same range as for mechanically alloyed materials but an order of magnitude smaller than those of conventionally HDDR processed alloys [123]. An increasing recombination temperature leads to grain growth consistent with the smaller half peak widths visible in Fig. 9.11. The slightly smaller grain sizes of around 40 nm for $Nd_2Co_{14}B$, compared to approximately 50 nm for the $Nd_2Fe_{14}B$ alloy when recombining at 600°C, could be attributed to an increased number of nucleation centers and/or changed grain growth kinetics of the $Nd_2Co_{14}B$ phase on desorption.

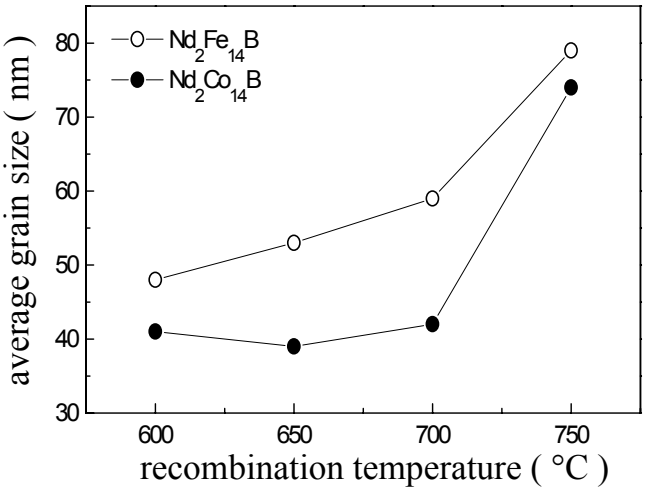

Fig. 9.12: Average grain sizes of recombined $Nd_2Fe_{14}B$ and $Nd_2Co_{14}B$ powders in dependence on the recombination temperature.

9.2.6 Remanence enhancement of recombined Nd(Fe,Co)B powders

Hysteresis loops of the $Nd_2Fe_{14}B$ and $Nd_2Co_{14}B$ powders recombined at different temperatures exhibit a good squareness and a magnetic single-phase behaviour. Figure 9.13 shows the initial magnetisation and demagnetisation curves of both samples after heat treatment at 600ºC. The remanences of the recombined $Nd_2Fe_{14}B$ and $Nd_2Co_{14}B$ powders in dependence on the recombination temperature are presented in Fig. 9.14.

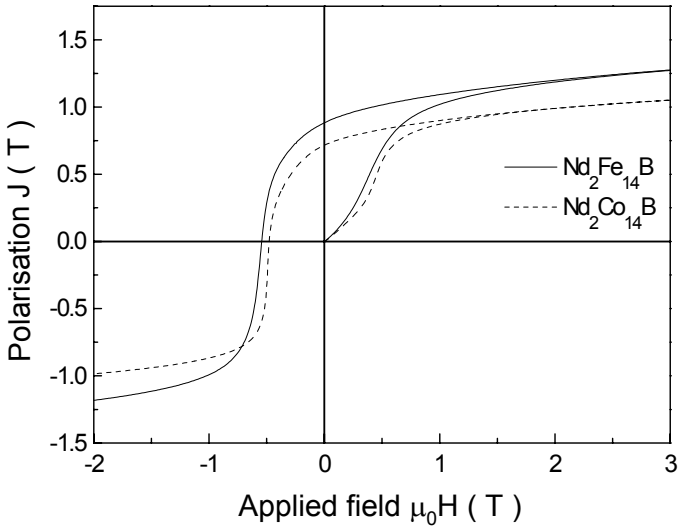

Fig. 9.13: Initial magnetisation curves and demagnetisation curves of reactively milled and recombined $Nd_2Fe_{14}B$ (straight line) and $Nd_2Co_{14}B$ (dashed line) powders after heat treatment at 600°C.

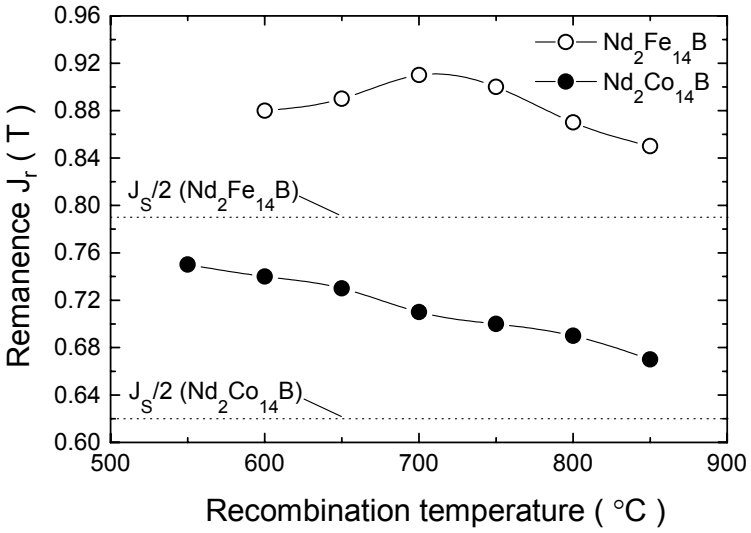

Fig. 9.14: Remanence of recombined $Nd_2Fe_{14}B$ and $Nd_2Co_{14}B$ powders in dependence on the recombination temperature.

The polarisation values at 8 T measured for these two alloys are 1.47 T in the case of the former material, and 1.14 T for the latter one. The 8 T polarisation is lower than the saturation polarisation J_s (1.58 T for $Nd_2Fe_{14}B$ and 1.24 T for $Nd_2Co_{14}B$ [81]) because of insufficient magnetic fields but, possibly, also because of a relatively high volume fraction of grain boundaries in the finely milled material. $Nd_2Fe_{14}B$ shows a maximum remanence

of J_r = 0.91 T after a 700°C annealing, whereas $Nd_2Co_{14}B$ has its maximum of J_r = 0.75 T at 550°C. Both values are significantly higher than the respective theoretical value $J_s / 2$ (indicated by dotted lines) assumed for an assembly of randomly oriented magnetically uniaxial single-domain particles. This observation is attributed to a microstructure controlled remanence enhancement caused by exchange-coupling (Section 3.1.1). A comparison of the J_r / J_s values for the recombined Co- and Fe-containing alloys shows that this effect is more effective for the $Nd_2Co_{14}B$ recombined alloy, possibly due to the slightly smaller grain size. The effect of remanence enhancement becomes more pronounced with decreasing recombination temperature in the case of the $Nd_2Co_{14}B$ alloy whereas a slight maximum is observed for the $Nd_2Fe_{14}B$ alloy. This maximum at 700°C can be explained by the superposition of two effects in the event of increasing recombination temperature: the higher amount of bcc-Fe (see Fig. 9.11a) leading to a higher saturation magnetisation (and, consequently, to a higher remanence) and, secondly, grain growth which has a negative effect on the remanence enhancement. In the case of $Nd_2Co_{14}B$, the increase in the intensity of the fcc-Co peak with increasing recombination temperature is very small (Fig. 9.11b) and the remanence depends mainly on grain size which increases with increasing recombination temperature.

9.3 Summary

The application of the “extreme” HDDR method of reactive milling in hydrogen and subsequent desorption allows, for the first time, the disproportionation and recombination and thus, effective grain refinement of thermodynamically more stable compounds such as $Nd_2(Fe_{1-x}Co_x)_{14}B$ with a high Co content. Using enhanced hydrogen pressure and temperature during milling, the disproportionation of the complete series ($0 \le x \le 1$) is possible; and even the disproportionation of $Nd_2Co_{14}B$, the most stable compound in the series of alloys investigated, into a very fine mixture of $NdH_{2+\delta}$ and fcc-Co can be accomplished. The desorption behaviour of the disproportionated $Nd_2(Fe_{1-x}Co_x)_{14}B$ powders ($0 \le x \le 1$) shows a shift of the onset temperature of the recombination reaction, T_s, to lower values with increasing Co content, from T_s = 554°C for $Nd_2Fe_{14}B$ to T_s = 460°C for $Nd_2Co_{14}B$, consistent with the respective thermodynamic stabilities.

Slightly smaller grain sizes of around 40 nm are obtained from XRD patterns for $Nd_2Co_{14}B$, compared to approximately 50 nm for the $Nd_2Fe_{14}B$ alloy when recombining at 600°C. Both alloys show enhanced remanences which is attributed to the effect of exchange-coupling between the nanoscaled grains, the effect being more pronounced for the $Nd_2Co_{14}B$ alloy.

10 Conclusions and future work

In the present work, isotropic nanocrystalline (Nd,Pr)(Fe,Co)B permanent magnets have been produced by using three different techniques: rapid quenching, high energy ball milling in argon and reactive milling in hydrogen. One task has been to use non-equilibrium processing routes to transfer excellent intrinsic magnetic properties into good extrinsic properties of nanocrystalline magnets. The resulting randomly oriented grain structure limits, in principle, the remanent polarisation, J_r, and the energy product, $(BH)_{max}$, to 0.5 and 0.25, respectively, of the values obtainable for ideal microstructures consisting of single domain grains with full crystallographic alignment. Remanence enhancement via exchange-coupling has been used in this study to obtain remanences substantially above the Stoner-Wohlfarth limit, $J_r = 0.5J_s$. As a second task, the intergrain interactions between the crystallites of the nanocomposite structures have been analysed systematically in terms of their dependence on temperature, composition and grain sizes.

Rare-earth rich magnets

Highly coercive $(Nd_{1-x}Pr_x)_2Fe_{14}B$-type magnets ($0 \leq x \leq 1$) were prepared using high energy ball milling and melt-spinning techniques. The compositions for the basic ternary alloys were: $Nd_{14.7}Fe_{77.3}B_{8.0}$ and $Pr_{14.7}Fe_{77.3}B_{8.0}$. The intensively milled powders consist of a mixture of nanocrystalline α-Fe and an amorphous phase. Melt-spun flakes are in a partly amorphous state with very small nanocrystallites of α-Fe. Thus, subsequent annealing is necessary in both cases to create the microstructure responsible for the high coercivities characteristic for these decoupled magnets: hard magnetic grains separated by a thin R-rich paramagnetic phase. Determination of the temperature necessary for complete crystallisation of the hard magnetic phase is very useful to select the adequate annealing temperature, in other words to avoid undesired grain growth effects. Optimum annealing temperatures for all the materials are in the range of 600 to 700 ºC. The combined addition of small amounts of Dy (1 at.%) and Zr (0.1 at.%) results in much higher coercivities than those corresponding to the additive-free alloys with, for example, a value of $\mu_0 H_c = 2.50$ T for milled and annealed $Nd_{14.8}Dy_{1.0}Fe_{77.3}B_{8.0}Zr_{0.1}$ compared to $\mu_0 H_c = 1.75$ T for the ternary $Nd_{14.7}Fe_{77.3}B_{8.0}$. This increase is attributed to the higher anisotropy field due to the addition

of Dy and the grain-growth-inhibiting effect of Zr. As a result, only a small variation in coercivity and remanence with increasing annealing temperature is observed. Grain sizes for the additive-containing alloys after annealing are in the range of 70-100 nm resulting, additionally, in a more homogeneous microstructure than that of the additive-free alloys. An important effect resulting from the substitution of Nd by Pr is the increased coercivity due to the higher anisotropy field associated with the $Pr_2Fe_{14}B$ phase, with the largest coercivity obtained for a melt-spun and annealed $Pr_{14.8}Dy_{1.0}Fe_{77.3}B_{8.0}Zr_{0.1}$ alloy ($\mu_0 H_c$ = 2.71 T).

Another important advantage of the Pr-containing alloys is the low deformation force necessary for texturing by hot deformation, with the lowest value obtained for the milled $Pr_{14.7}Fe_{77.3}B_{8.0}$ ternary alloy (about 5 MPa whereas about 15 MPa for the well-known melt-spun NdFeB-"MQP-A" are required). $Pr_{14.7}Fe_{77.3}B_{8.0}$ textured by die-upsetting exhibits magnetic properties as high as $\mu_0 H_c$ = 1.20 T, J_r = 1.27 T and $(BH)_{max}$ = 307 kJm^{-3}. These promising values and the absence of spin reorientation for $Pr_2Fe_{14}B$ (taking place at $T <$ 135K for $Nd_2Fe_{14}B$), make PrFeB-based magnets good candidates for low temperature applications, e.g. in conjunction with superconductors, where high performance is required.

Nearly single-phase magnets

The large anisotropy field of the $Pr_2Fe_{14}B$ phase can be very useful to enhance the remanence at the expense of the coercivity. A first possibility is the substitution of part of Pr by Nd which increases the remanence without decreasing excessively the coercivity, resulting in a higher value of $(BH)_{max}$. Since the best combination of magnetic properties was obtained for the milled and annealed $Pr_{11.25}Nd_{3.75}Dy_{1.0}Fe_{76.0}B_{8.1}Zr_{0.1}$ alloy ($(BH)_{max}$ = 92 kJm^{-3}), the Dy and Zr contents and the Pr:Nd ratio remained unchanged in the new alloy: $Pr_{9.0}Nd_{3.0}Dy_{1.0}Fe_{72.0}Co_{8.0}B_{6.9}Zr_{0.1}$. Reduction of the R content gives rise to significant remanence enhancement (J_r = 0.92 T) and high coercivity ($\mu_0 H_c$ = 1.25 T). A very fine and homogeneous microstructure with a mean grain size of 20 nm leads to an effective exchange-coupling, which explains the large remanence obtained. A small amount of an FeCo soft magnetic phase is detected in the milled and annealed powders but the magnetically single-phase behaviour observed during demagnetisation is indicative of

the coupling with the neighbouring hard magnetic grains. As a consequence, the hysteresis loop exhibits a good square shape resulting in a high energy product: $(BH)_{max}$ = 140 kJm^{-3}. The small amount of Co present in the sample has been shown to play an important role: increasing the saturation polarisation, as a grain refiner of the microstructure and increasing the Curie temperature ($T_C \approx 385$ºC).

Nanocomposite magnets

Intensive milling has been shown to be a very versatile technique to produce high-performance nanocomposite magnets by blending the $Pr_{9.0}Nd_{3.0}Dy_{1.0}Fe_{72.0}Co_{8.0}B_{6.9}Zr_{0.1}$ alloy with different fractions of soft magnetic α-Fe (x = 5 - 35 wt.% α-Fe). Enhanced remanences are found across the whole series with relative remanences ($\alpha' = J_r / J_s$) increasing from 0.66 for the starting alloy to 0.74 for 35wt.% α-Fe. A simple increase in the remanence, however, does not automatically lead to high energy densities as $\mu_0 H_c \geq J_r / 2$ has to be fulfilled additionally and the shape of the demagnetisation curve must not differ too much from the ideal squared shape. According to these requirements, the best combination of magnetic properties is obtained for the sample with x = 25wt.% α-Fe: J_r = 1.19 T, $\mu_0 H_c$ = 0.66 T and a very high $(BH)_{max}$ value of 178 kJm^{-3}, the high remanence i.e. $(BH)_{max}$ being due to the high saturation magnetisation of Fe and an effective exchange-coupling between the different grains. The very fine and homogeneous microstructure consists of hard and soft magnetic grains with a mean size of 20 and 15 nm, respectively. A diffusional redistribution of Co and Fe during the crystallisation process results in a lower Co content in the hard magnetic phase and the formation of the FeCo soft magnetic phase. This is due to the complete solubility of Co in the $R_2T_{14}B$ and α-Fe phases which results in a Curie temperature for the hard magnetic phase of about 365ºC. In terms of applications, the achieved energy product and Curie temperature of this isotropic nanocomposite powder make it an excellent candidate for bonded magnets with the additional advantage of a reduced rare-earth content, i.e. lower cost and improved corrosion resistance. The greatest potential market for these magnets is the automotive industry where, in addition to the mentioned advantages, the possibility of developing complex shapes combined with good magnetisibility and the good mechanical properties exhibited can be very useful. Several factors still need to be explored before the successful

production of bonded magnets using this powder: the reactivity of the very fine milled powder before bonding and friction between particles and resulting magnet density.

Reversal magnetisation processes

Analysis of recoil loops produced during demagnetisation by application of reverse fields to a previously saturated sample yields useful information about the process. These recoil loops have been measured at room temperature for, first, a decoupled magnet with the composition $Pr_{14.7}Fe_{77.3}B_{8.0}$ and, second, two different exchange-coupled materials: the nearly single-phase $Pr_{9.0}Nd_{3.0}Dy_{1.0}Fe_{72.0}Co_{8.0}B_{6.9}Zr_{0.1}$ alloy and the two-phase composite resulting of blending this alloy with 25wt.% α-Fe by milling. The recoil loops for the first alloy are completely closed whereas those of the exchange-coupled materials are slightly open for the nominally single-phase composition, due to the presence of some soft magnetic phase, and significantly more open for the nanocomposite $R_2T_{14}B/\alpha$-(FeCo) -type magnet. In addition, steeper recoil loops (more pronounced in the case of the nanocomposite material) are observed for these latter alloys. This behaviour is characteristic for two-phase magnets and it is due to the reversible rotation of the exchange-coupled soft magnetic phase for fields not large enough to reverse the magnetisation of the hard magnetic phase. Measurements at low temperature show a rectangularly shaped hysteresis loop for the single-phase PrNdDyFeCoBZr alloy whereas a shoulder in the demagnetisation curve for the composite material was found. This two-step demagnetisation process is a consequence of the temperature dependence of the exchange length: the increase of the anisotropy constant K_1 with decreasing temperature results in a reduction of the critical exchange length for an effective exchange-coupling, δ_w, given by $\delta_w = \pi(A/K_1)^{1/2}$. An analysis of the reversible and irreversible changes in the polarisation during the demagnetisation process indicates, by comparison with the room temperature measurement for an identically processed sample, that a larger fraction of Fe moments are contributing to the reversible change in polarisation for fields smaller than the switching field of the hard phase. This agrees with the first step observed at low reversed fields as a consequence of the independent reversal of the less effectively coupled soft magnetic grains, and the second step, at larger reversed fields, being due to reversal of the exchange-coupled grains. Low temperature measurements of the samples do not show any sign of

spin reorientation. A more detailed study of the inner loops has been carried out in order to obtain information about the intergrain interactions acting during the demagnetisation process. This has been done by plotting the quantity δJ which yields the deviation from the theoretical remanent polarisation for an applied reversed field given by Wohlfarth's relation [46]. Two kinds of interactions are mainly responsible for possible deviations: magnetostatic and exchange interactions. Different interpretations can be found in the literature concerning the sign of δJ. The evolution of the δJ values has been analysed when varying (i) the Fe-content, (ii) the annealing temperature, i.e. the grain size and (iii) the measurement temperature, i.e. variation of the exchange length. This systematic study has shown that negative deviations from $\delta J = 0$ can be interpreted as being indicative for the main role of the exchange interactions whereas positive deviations point to magnetostatic interactions to be predominant. The evolution of δJ at room temperature for three different types of alloys is shown in Fig. 10.1b illustrating this result. In the case of the $Pr_{14.7}Fe_{77.3}B_{8.0}$ alloy, δJ is exclusively positive which has been interpreted in terms of dominant magnetostatic interactions between the decoupled hard magnetic grains. The nominally single-phase alloy shows almost symmetrical positive and negative deviations from $\delta J = 0$ indicating that both types of interactions are of significance. An increase of the soft magnetic phase by the addition of 25wt.% α-Fe leads to a stronger exchange interaction, with exclusively negative δJ values.

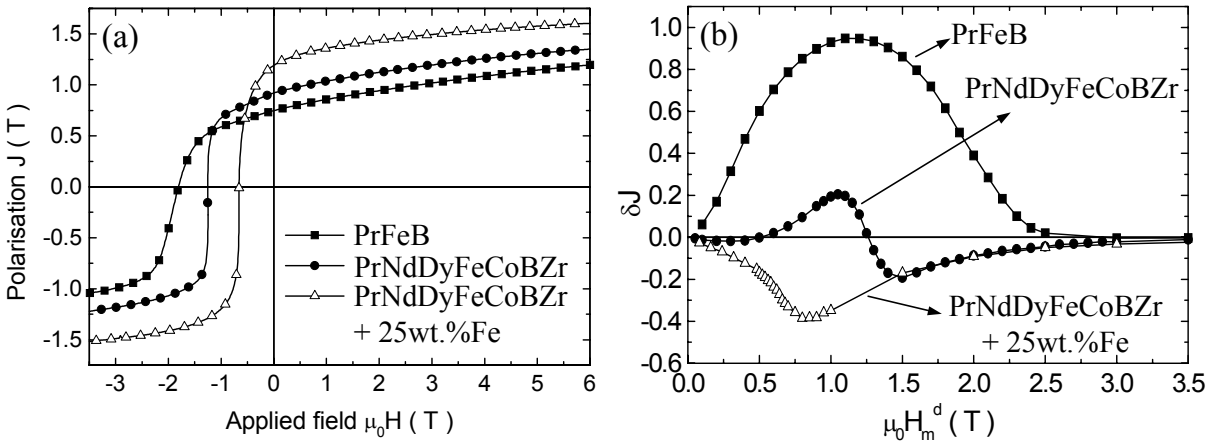

Fig. 10.1: Measurements performed on $Pr_{14.7}Fe_{77.3}B_{8.0}$, $Pr_{9.0}Nd_{3.0}Dy_{1.0}Fe_{72.0}Co_{8.0}B_{6.9}Zr_{0.1}$ and $Pr_{9.0}Nd_{3.0}Dy_{1.0}Fe_{72.0}Co_{8.0}B_{6.9}Zr_{0.1}$ + 25wt.% α-Fe after milling and annealing. (a) Demagnetisation curves; (b) δJ-plots as function of the reversed applied field.

However, a phenomenological analysis of these δJ-plots remains to be undertaken. Simple theoretical models could be very helpful to distinguish the different contributions due to the intergrain interactions taking place during the demagnetisation process. In this way, the study of model systems consisting of phases with strongly different intrinsic magnetic properties should yield additional information by, for example, studying the effect of change of the exchange lengths and grain growth processes on the corresponding δJ values.

Reactive milling in hydrogen

This technique is an alternative route to the standard high energy ball milling and rapid quenching techniques for the preparation of amorphous or nanocrystalline materials. The procedure consists of ball milling under enhanced hydrogen pressure and temperature to disproportionate the material (for example $Nd_2Fe_{14}B$) into a finely divided mixture ($NdH_{2+\delta}$, α-Fe and Fe_2B). Subsequent desorption leads to the recombination of the original hard magnetic phase, but now with a much refined grain size, in the same range as mechanically alloyed materials but an order of magnitude smaller than those of conventionally HDDR (Hydrogenation-Disproportionation-Desorption-Recombination) processed alloys. Magnetic characterisation of the reactively milled and recombined $Pr_{14.7}Fe_{77.3}B_{8.0}$ powders has shown, by comparison with the conventionally milled alloy, slightly higher remanences and lower coercivities due to the extreme conditions used in the former route.

The application of this technique has allowed for the first time the disproportionation and recombination and, thus, effective grain refinement of the thermodynamically very stable compounds $Nd_2(Fe_{1-x}Co_x)_{14}B$ with a high Co content. In fact, the disproportionation of the complete series ($0 \leq x \leq 1$) has been possible (including $Nd_2Co_{14}B$, the most stable compound in this series of alloys). $Nd_2Co_{14}B$ exhibits slightly smaller grain sizes of around 40 nm, compared to approximately 50 nm for the $Nd_2Fe_{14}B$ alloy when recombining at 600^{o}C. Both alloys show enhanced remanences which is attributed to the effect of exchange-coupling between the nanoscaled grains, the effect being more pronounced for the $Nd_2Co_{14}B$ alloy. It would be very interesting to undertake a careful study of the disproportionated state by using more sensitive techniques than X-ray diffraction or TEM

(Mössbauer spectroscopy, for example) because the reduced amount and small size of the $(Fe,Co)_2B$ phase in the very fine disproportionated mixture makes it extremely difficult to detect it by conventional methods.

Reactive milling is a novel method suitable for production of multiphase exchange-coupled magnet powders with its full potential still to be explored. Innovative techniques such as reactive milling should open new perspectives not only in the field of permanent magnets.

References

[1] S. Chikazumi, *"Physics of Ferromagnetism"*, Oxford Science Publications (1997).

[2] D.B.Cullity, *"Introduction to magnetic materials"*, Addison-Wesley Publishing Company (1972).

[3] J.M.D. Coey (Editor), "*Rare Earth Iron Permanent Magnets"*, Clarendon Press Oxford (1996).

[4] J.F. Herbst and J.J. Croat, *"Neodymium-iron-boron permanent magnets"*, J. Magn. Magn. Mater. **100** (1991) 57.

[5] O. Gutfleisch, *"Controlling the properties of high energy density permanent magnetic materials by different processing routes"*, J. Phys. D: Appl. Phys. **33** (2000) R157.

[6] A. Hubert and R. Schäfer, *"Magnetic Domains: The Analysis of Magnetic Microstructures"*, Springer, Berlin (1998).

[7] *"Encyclopedia of Materials: Science and Technology"*, Elsevier Science Ltd. (2001), O. Gutfleisch: *"Rare Earth Magnets: Materials"*, pp. 8022-8026.

[8] J.D. Livingston, in *"Soft and Hard Magnetic Materials with Applications"*, eds. J.A. Salsgiver et al, ASM, Metals Park Ohio (1986) p. 71.

[9] G.C. Hadjipanayis and W. Gong, *"Lorentz microscopy in melt-spun R-Fe-B alloys"*, J. Magn. Mag. Mater. **66** (1987) 390.

[10] L. Folks, R. Street, R.C. Woodward and K. Babcock, *"Magnetic force microscopy images of high-coercivity permanent magnets"*, J. Magn. Magn. Mater. **159** (1996) 109.

[11] D. Eckert, A. Kirchner, O. Gutfleisch, W. Grünberger, B. Gebel, K. Arnold, A. Handstein, M. Wolf and K.-H. Müller, *"Magnetization processes in different types of fine grained Nd-Fe-B magnets"*, Proc. 10^{th} Int. Symp. Magn. Anisotropy and Coercivity in RE-TM Alloys, Dresden, Germany (1998) p. 297.

[12] O. Gutfleisch, D. Eckert, R. Schäfer and K.-H. Müller, *"Magnetization processes in two different types of anisotropic, fully dense NdFeB hydrogenation, disproportionation, desorption and recombination magnets"*, J. Appl. Phys. **87** (2000) 6119.

[13] O. Gutfleisch, K. Khlopkov, D. Eckert, B. Wall, W. Rodewald, D. Hinz and K.-H. Müller, *"Determination of microtexture and magnetization processes in Nd-Fe-B magnets with maximized energy density"*, Proc. 17th Int. Workshop on RE Magnets and their Appl., Delaware, USA (2002) p. 566.

[14] E. Adler and P. Hamann, *"A contribution to the understanding of coercivity and its temperature dependence in sintered $SmCo_5$ and $Nd_2Fe_{14}B$ magnets"*, Proc. 4th Int. Symp. Magn. Anisotropy and Coercivity in RE-TM Alloys, Dayton (1985) pp. 747-760.

[15] H. Kronmüller, K.-D. Durst and M. Sagawa, *"Analysis of the magnetic hardening mechanism in RE-FeB permanent magnets"*, J. Magn. Magn. Mater. **74** (1988) 291.

[16] D. Goll, M. Seeger and H. Kronmüller, *"Magnetic and microstructural properties of nanocrystalline exchange coupled PrFeB permanent magnets"*, J. Magn. Magn. Mater. **185** (1998) 49.

[17] *"Encyclopedia of Materials: Science and Technology"*, Elsevier Science Ltd. (2001), O. Gutfleisch: *"Basic Principles of Hard Magnetic Materials"*, pp. 3719-3722.

[18] D. Givord and M.F. Rossignol in "*Rare Earth Iron Permanent Magnets"*, J.M.D. Coey (Editor), Clarendon Press Oxford (1996) pp. 218-285.

[19] R. Skomski and J.M.D. Coey, *"Permanent Magnetism"*, Institute of Physics Publishing Ltd. (1999).

[20] M. Sagawa, S. Fujimori, M. Togawa and Y. Matsuura, *"New material for permanent magnets on a base of Nd and Fe"*, J. Appl. Phys. **55** (1984) 2083.

[21] J. Wecker, M. Katter and L. Schultz, *"Mechanically alloyed Sm-Co materials"*, Appl. Phys. Lett. **69** (1991) 6058.

[22] K. Schnitzke, L. Schultz, J. Wecker and M. Katter, *"High coercivity in $Sm_2Fe_{17}N_x$ magnets"*, Appl. Phys. Lett. **57** (1990) 2853.

[23] C. Kuhrt, K. O'Donnell, M. Katter, J. Wecker, K. Schnitzke and L. Schultz, *"Pressure-assisted zinc bonding of microcrystalline $Sm_2Fe_{17}N_x$ powders"*, Appl. Phys. Lett. **60** (1992) 3316.

[24] K.-H. Müller, D. Eckert, A. Handstein and P. Nothnagel, *"Deviations from Wohlfarth's remanence relationship in NdFeB magnets"*, J. Magn. Magn. Mater. **104-107** (1992) 1173.

[25] D. Eckert, K.-H. Müller, M. Wolf, W. Rodewald and B. Wall, *"Ageing effects in sintered $(Nd,Dy)_{15}(Fe,Co,Mo,Al)_{77}B_8$ permanent magnets"*, IEEE Trans. Mag. **29** (1993) 2755.

[26] K.-H. Müller, L. Cao, N.M. Dempsey and P.A.P. Wendhausen, *"Sm_2Fe_{17} interstitial magnets"*, J. Appl. Phys. **79** (1996) 5045.

[27] D. Eckert, P.A.P. Wendhausen, B. Gebel, M. Wolf, K.-H. Müller, *"Comparison of magnetization processes in differently prepared $Sm_2Fe_{17}N_3$ permanent magnets"*, J. Magn. Magn. Mater. **157/158** (1996) 93.

[28] H. Kronmüller, K.D. Durst, W. Ervens and W. Fernengel, *"Micromagnetic analysis of precipitation hardened permanent magnets"*, IEEE Trans. Magn. **20** (1984) 1569.

[29] M. Katter, J. Weber, W. Assmus, P. Schrey and W. Rodewald, *"A new model for the coercivity mechanism of $Sm_2(Co,Fe,Cu,Zr)_{17}$ magnets"*, IEEE Trans. Magn. **32** (1996) 4815.

[30] E.C. Stoner and E.P. Wohlfarth, *"A mechanism of magnetic hysteresis in heterogeneous alloys"*, Philos. Trans. R. Soc. **240** (1948) 599.

[31] E.F. Kneller and R. Hawig, *"The exchange-spring magnet: a new material principle for permanent magnets"*, IEEE Trans. Magn. **27** (1991) 3588.

[32] T. Schrefl, H. Kronmüller and J. Fidler, *"Exchange hardening in nano-structured two-phase permanent magnets"*, J. Magn. Magn. Mater. **127** (1993) L273.

[33] T. Schrefl, J. Fidler and H. Kronmüller, *"Remanence and coercivity in isotropic nanocrystalline permanent magnets"*, Phys. Rev. B **49** (9) (1994) 6100.

[34] G. Rieger, M. Seeger, Li Sun, H. Kronmüller, *"Micromagnetic analysis applied to melt-spun NdFeB magnets with small additions of Ga and Mo"*, J. Magn. Magn. Mater. **151** (1995) 193.

[35] H. Kronmüller, R. Fischer, M. Seeger and A. Zern, *"Micromagnetism and microstructure of hard magnetic materials"*, J. Phys. D: Appl. Phys. **29** (1996) 2274.

[36] R. Fischer and H. Kronmüller, *"The role of the exchange interaction in nanocrystalline isotropic $Nd_2Fe_{14}B$-magnets"*, J. Magn. Magn. Mater. **191** (1999) 225.

[37] J.J. Croat, J.F. Herbst, R.W. Lee and F.E. Pinkerton, *"Pr-Fe and Nd-Fe: A new class of high performance permanent magnets"*, J. Appl. Phys. **55** (1984) 2078.

[38] R.W. McCallum, A.M. Kadin, G.B. Clemente and J.E. Keem, *"High performance isotropic permanent magnet based on Nd-Fe-B"*, J. Appl. Phys. **61** (1987) 3577.

[39] G.B. Clemente, K.E. Keem and J.P. Bradley, *"The microstructural and compositional influence upon HIREM behavior in $Nd_2Fe_{14}B$"*, J. Appl. Phys. **64** (1988) 5299.

[40] A. Manaf, M. Leonowicz, H.A. Davies and R.A. Buckley, *"Effect of grain size and microstructure on magnetic properties of rapidly solidified $Fe_{82.4}Nd_{13.1}B_{4.5}$ alloy"*, J. Appl. Phys. **70** (1991) 6366.

[41] A. Manaf, P.Z. Zhang, I. Ahmad, H.A. Davies and R.A. Buckley, "*Magnetic properties and microstructural characterisation of isotropic nanocrystalline Fe-Nd-B based alloys"*, IEEE Trans. Magn. **29** (1993) 2866.

[42] H. Fukunaga and K. Inoue, *"Effect of intergrain exchange interaction on magnetic properties in isotropic Nd-Fe-B magnets"*, Jpn. J. Appl. Phys. **31** (1992) 1347.

[43] R. Coehoorn, D.B. de Mooij, J.P.W.B. Duchateau and K.H.J. Buschow, *"Novel permanent magnetic materials made by rapid quenching"*, J. de Phys. **49** (1988) C8-669.

[44] D. Eckert, K.-H. Müller, A. Handstein, J. Schneider, R. Grössinger and R. Krewenka, *"Temperature dependence of the coercive force in $Nd_4Fe_{77}B_{19}$"*, IEEE Trans. Magn. **26** (1990) 1834.

[45] J. Schneider, D. Eckert, K.-H. Müller, A. Handstein, H. Mühlbach, H. Sassik and H.R. Kirchmayr, *"Magnetization processes in $Nd_4Fe_{77}B_{19}$ permanent magnetic materials"*, Mat. Lett. **9** (5,6) (1990) 201.

[46] E.P. Wohlfarth, *"Relations between different modes of acquisition of the remanent magnetization of ferromagnetic particles"*, J. Appl. Phys. **29** (1958) 595.

[47] G.W.D. Spratt, P.R. Bissell, R.W. Chantrell and E.P. Wohlfarth, *"Static and dynamic experimental studies on particulate recording media"*, J. Magn. Magn. Mater. **75** (1988) 309.

[48] L. Folks, R. Street and R. Woodward, *"Investigation of interaction mechanisms in melt-quenched NdFeB"*, J. Appl. Phys. **75** (1994) 6271.

[49] E.H. Feutrill, P.G. McCormick and R. Street, *"Magnetization behaviour in exchange-coupled $Sm_2Fe_{14}Ga_3C_2$/α-Fe"*, J. Phys. D: Appl. Phys. **29** (1996) 2320.

[50] I. Panagiotopoulos, L. Withanawasam and G.C. Hadjipanayis, *"Exchange spring behavior in nanocomposite hard magnetic materials"*, J. Magn. Magn. Mater. **152** (1996) 353.

[51] Z. Cheng, H. Kronmüller and B. Shen, *"Microstructure refinement and improvements of magnetic properties of two-phase exchange-coupled $Sm_2Fe_{15}Ga_2C_x$/α-Fe nanocomposites by additional Zr"*, Appl. Phys. Lett. **73** (11) (1998) 1586.

[52] J. Ding, Y. Li and P.T. Yong, *"A comparative study of melt-spun ribbons of $Nd_{12}Fe_{82}B_6$ and $Nd_{15}Fe_{77}B_8$"*, J. Phys. D: Appl. Phys. **31** (1998) 2745.

[53] S. Zhang, H. Zhang, B. Shen, T. Zhao, F.R. de Boer and K.H.J. Buschow, *"Investigation of magnetization reversal in Sm-Fe-Cu(Zr)-Ga-C nanocomposite magnets"*, J. Appl. Phys. **87** (3) (2000) 1410.

[54] H. Zhang, W. Zhang, A. Yan, Z. Sun, B. Shen, I. Tung and T. Chin, *"The hard magnetic properties of nanocomposite $Nd_{3.6}Pr_{5.4}Fe_{83}Co_3B_5$ ribbons prepared by melt spinning"*, Mat. Sc. and Eng. **A304-306** (2001) 997.

[55] P.G. McCormick, J. Ding, E.H. Feutrill and R. Street, *"Mechanically alloyed hard magnetic materials"*, J. Magn. Magn. Mater. **157/158** (1996) 7.

[56] S. Hirosawa, H. Kanekiyo and M. Uehara, *"High-coercivity iron-rich rare-earth permanent magnet material based on $(Fe, Co)_3B$-Nd-M (M=Al, Si, Cu, Ga, Ag, Au)"*, J. Appl. Phys. **73** (1993) 6488.

[57] D.H. Ping, K. Hono and S. Hirosawa, *"Partitioning of Ga and Co atoms in a $Fe_3B/Nd_2Fe_{14}B$ nanocomposite magnet"*, J. Appl. Phys. **83** (1998) 7769.

[58] M. Uehara, T.J. Konno, H. Kanekiyo, S. Hirosawa, K. Sumiyama and K. Suzuki, *"Effect of Cr doping on crystallization behavior of $Fe_3B/Nd_2Fe_{14}B$ nanocomposite permanent magnets"*, J. Magn. Magn. Mater. **177** (1998) 997.

[59] S. Hirosawa and H. Kanekiyo, *"Exchange-coupled permanent magnets based on α-$Fe/Nd_2Fe_{14}B$ nanocrystalline composite"*, Proc. 13th Int. Workshop on RE Magnets and their Applications, Birmingham, UK, **87** (1994) p. 87.

[60] J. Bauer, M. Seeger, A. Zern and H. Kronmüller, *"Nanocrystalline FeNdB permanent magnets with enhanced remanence"*, J. Appl. Phys. **80** (1996) 1667.

[61] A. Melsheimer, M. Seeger and H. Kronmüller, *"Influence of Co substitution in exchange coupled NdFeB nanocrystalline permanent magnets"*, J. Magn. Magn. Mater. **202** (1999) 458.

[62] P. Crespo, V. Neu and L. Schultz, *"Mechanically alloyed nanocomposite powders of $Nd_2Fe_{14}B$/α-Fe with additional elements"*, J. Phys. D: Appl. Phys. **30** (1997) 2298.

[63] V. Neu, L. Schultz and H.-D. Bauer, "*Grain size dependence of remanence enhancement and coercivity in nanocrystalline Nd-Fe-B powders"*, Nanostructured Materials **12** (1999) 769.

[64] O.V. Billoni, S.E. Urreta, L.M. Fabietti and H.R. Bertorello, *"Dependence of the coercivity on the grain size in a FeNdB + α-Fe nanocrystalline composite with enhanced remanence"*, J. Magn. Magn. Mater. **187** (1998) 371.

[65] X.K. Sun, J. Zhang, Y. Chu, W. Liu, B. Cui and Z. Zhang, *"Dependence of magnetic properties on grain size of α-Fe in nanocomposite $(Nd,Dy)(Fe,Co,Nb,B)_{5.5}$/α-Fe magnets"*, Appl. Phys. Lett. **74** (12) (1999) 1740.

[66] Q.F. Xiao, T. Zhao, Z.D. Zhang, E. Bruck, K.H.J. Buschow and F.R. de Boer, *"Effect of grain size and magnetocrystalline anisotropy on exchange coupling in nanocomposite two-phase Nd-Fe-B magnets"*, J. Magn. Magn. Mater. **223** (2001) 215.

[67] J. Fidler and P. Skalicky, *"Microstructure of precipitation hardened cobalt rare earth permanent magnets",* J. Magn. Magn. Mater. **27** (1982) 127.

[68] A.E. Ray, *"Metallurgical behavior of $Sm(Co,Fe,Cu,Zr)_z$ alloys"*, J. Appl. Phys. **55** (1984) 2094.

[69] O. Gutfleisch, M. Kubis, A. Handstein, K.-H. Müller and L. Schultz, *"Hydrogenation disproportionation desorption recombination in Sm–Co alloys by means of reactive milling"*, Appl. Phys. Lett. **73** (1998) 3001.

[70] Z. Chen, X. Meng-Burany, H. Okumura and G.C. Hadjipanayis, *"Magnetic properties and microstructure of mechanically milled $Sm_2(Co,M)_{17}$-based powders with M = Zr, Hf, Nb, V, Ti, Cr, Cu and Fe"*, J. Appl. Phys. **87** (2000) 3409.

[71] A. Yan, A. Bollero, O. Gutfleisch and K.-H. Müller, *"Microstructure and magnetization reversal in nanocomposite $SmCo_5/Sm_2Co_{17}$ magnets"*, J. Appl. Phys. **91** (2002) 2192.

[72] A. Yan, A. Bollero, O. Gutfleisch and K.-H. Müller, *"Microstructure and magnetic properties of two-phase exchange-coupled $SmCo_5/Sm_2(Co,M)_{17}$ (M = Fe, Zr, Cu) nanocomposites"*, J. Phys. D: Appl. Phys. **35** (2002) 835.

[73] J.F. Herbst and W.B. Yelon, *"Preferential site occupation and magnetic structure of $Nd_2(Co_xFe_{1-x})_{14}B$ systems"*, J. Appl. Phys. **60** (1986) 4224.

[74] K.G. Knoch, R. Reinsch and G. Petzow, *"The Nd-Fe-B phase diagram and the primary solidification of $Nd_2Fe_{14}B$"*. In: I.R. Harris et al. (eds.) Proc. 13th Int. Workshop on RE Magnets and their Applications, Birmingham (1994) pp. 503-10.

[75] B.M. Ma, E.B. Boltich, S.G. Sankar, W.E. Wallace, *"Effect of texture and spin reorientation on the magnetic properties of Nd-Fe-B magnets"*, Phys. Rev. B **40** (10) (1989) 7332.

[76] L.H. Lewis, V. Panchanathan, J.Y. Wang, *"Technical magnetic properties of melt-spun $(Nd_{1-x}Pr_x)Fe_{14}B$ at low temperature"*, J. Magn. Magn. Mater. **176** (1997) 288.

[77] A. Handstein, K.-H. Müller, D. Eckert and P. Nothnagel, *"The dip in the magnetisation curves of sintered Nd-Fe-B magnets with different degrees of texture"*, J. Magn. Magn. Mater. **101** (1991) 382.

[78] A. Fujita and I.R. Harris, *"Hydrogen absorption and desorption study of Nd-TM-B system"*, IEEE Trans. Magn. **30** (1994) 860.

[79] F. Bolzoni, F. Leccabue, O. Moze, L. Pareti and M. Solzi, *"3d and 4f magnetism in $Nd_2Fe_{14-x}Co_xB$ and $Y_2Fe_{14-x}Co_xB$ compounds"*, J. Appl. Phys. **61** (1987) 5369.

[80] K. Girgis, M. Kraft, U. Weis, P. Fischer and M. Sostarich, *"Crystal and magnetic structure of the permanent magnet materials $Nd_2Fe_{14-x}Co_xB$ (x = 0-14)"*, J. Less-Common Metals **162** (1990) 335.

[81] C.D. Fuerst, J.F. Herbst and E.A. Alson, *"Magnetic properties of $Nd_2(Co_xFe_{1-x})_{14}B$ alloys"*, J. Magn. Magn. Mater. **54-57** (1986) 567.

[82] A.C. Neiva, A.P. Tschiptschin, F.P. Missell, *"Phase diagram of the Pr-Fe-B system"*, J. Alloys Comp. **217** (1995) 273.

[83] S. Hirosawa, Y. Matsuura, H. Yamamoto, S. Fujimura, M. Sagawa and H. Yamauchi, *"Magnetization and magnetic anisotropy of $R_2Fe_{14}B$ measured on single crystals"*, J. Appl. Phys. **59** (1986) 873.

[84] E. Kneller, *"Ferromagnetism"*, Springer, Berlin (1962).

[85] Z. Wang, S. Zhou, Y. Qiao, M. Zhang and R. Wang, *"Phase transformations and magnetic properties of melt-spun $Pr_7Fe_{88}B_5$ ribbons during annealing"*, J. Alloys Comp. **299** (2000) 258.

[86] G. Mendoza-Suárez, H. A. Davies and J. I. Escalante-García, *"$_jH_c$, J_r and $(BH)_{max}$ relationship in PrFeB melt spun alloys"*, J. Magn. Magn. Mater. **218** (2000) 97.

[87] D. Goll, I. Kleinschroth and H. Kronmüller, *"High-performance nanocrystalline PrFeB-based bonded permanent magnets"*, Proc. 16th Int. Workshop on RE Magnets and their Appl., Sendai, Japan, ed. H. Kaneko (2000) p. 641.

[88] H.A. Davies, J.I. Betancourt R. and C.L. Harland, *"Nanophase Pr and Nd/Pr-based rare earth-iron-boron alloys"*, Proc. 16th Int. Workshop on RE Magnets and their Appl., Sendai, Japan, ed. H. Kaneko (2000) p. 485.

[89] N. Yoshikawa, H. Yamada, Y. Iwasaki, K. Nagata and Y. Kasai, *"Magnetic properties and multi-pole magnetizability of a huge radially oriented Nd-Fe-B ring magnet for EV driving motors"*, Proc. 13th Int. Workshop on Rare Earth Magnets and their Applications, Birmingham, UK (1994) p. 635.

[90] C.D. Fuerst, E. G. Brewer, R.K. Mishra, Yimei Zhu and D.O. Welch, *"Die-upset Pr-Fe-B-type magnets from melt-spun ribbons"*, J. Appl. Phys. **75** (1994) 4208.

[91] W. Grünberger, D. Hinz, D. Schläfer and L. Schultz, *"Microstructure, texture, and magnetic properties of backward extruded NdFeB ring magnets"*, J. Magn. Magn. Mater. **157/158** (1996) 41.

[92] A. Kirchner, W. Grünberger, O. Gutfleisch, V. Neu, K.-H. Müller and L. Schultz, *"A comparison of the magnetic properties and deformation behaviour of Nd-Fe-B magnets made from melt-spun, mechanically alloyed and HDDR powders"*, J. Phys. D: Appl. Phys. **31** (1998) 1660.

[93] N. Yoshikawa, T. Iriyama, H. Yamada, Y. Kasai and V. Panchanathan, *"Radially oriented high energy product Nd-Fe-B ring magnets"*, IEEE Trans. Magn. **35** (1999) 3268.

[94] J.S. Benjamin and M.S. Bamford, *"Dispersion Strengthened Aluminium made by mechanical alloying"*, Metall. Trans. **A8** (1977) 1301.

[95] X.L. Yeh, K. Samwer and W.L. Johnson, *"Formation of an amorphous metallic hydride by reaction of hydrogen with crystalline intermetallic compounds - A new method of synthesizing metallic glasses"*, Appl. Phys. Lett. **42** (1983) 242.

[96] R.B. Schwarz and W.L. Johnson, *"Formation of an amorphous alloy by solid-state reaction of the pure polycrystalline metals"*, Phys. Rev. Lett. **51** (1983) 415.

[97] L. Schultz, J. Wecker and E. Hellstern, *"Formation and properties of NdFeB prepared by mechanical alloying and solid-state reaction"*, J. Appl. Phys. **61** (1987) 3583.

[98] L. Schultz, *"Formation of amorphous metals by mechanical alloying"*, Materials Science and Engineering, **97** (1988) 15.

[99] L. Schultz, K. Schnitzke and J. Wecker, *"Mechanically alloyed isotropic and anisotropic Nd-Fe-B magnetic material"*, J. Appl. Phys. **64** (1988) 5302.

[100] J. Wecker, K. Schnitzke, H. Cerva and W. Grogger, *"Nanostructured Nd–Fe–B magnets with enhanced remanence"*, Appl. Phys. Lett. **67** (1995) 563.

[101] M. Kubis, L. Cao, K.-H. Müller and L. Schultz, *"Hydrogenation disproportionation desorption recombination on $Sm_2Fe_{17-x}Ga_x$ with high Ga content ($x \geq 1$) by means of reactive grinding"*, J. Phys. D: Appl. Phys. **30** (1997) L51.

[102] O. Gutfleisch, M. Kubis, A. Handstein, K.-H. Müller and L. Schultz, *"Hydrogenation disproportionation desorption recombination in Sm–Co alloys by means of reactive milling"*, Appl. Phys. Lett. **73** (1998) 3001.

[103] T. Takeshita and R. Nakayama, *"Magnetic properties and microstructure of the NdFeB magnet powder produced by hydrogen treatment"*, Proc. 10th Int. Workshop on Rare Earth Magnets and their Applications, Kyoto, Japan (1987) p. 551.

[104] P.J. McGuiness, X.J. Zhang, X.J. Yin and I.R. Harris, *"Hydrogenation, disproportionation, desorption (HDD): An effective processing route for NdFeB-type magnets"*, J. Less-Common Met. **158** (1990) 379.

[105] O. Gutfleisch and I.R. Harris, *"Fundamental and practical aspects of the hydrogenation, disproportionation, desorption and recombination process"*, J. Phys. D: Appl. Phys. **29** (1996) 2255.

[106] R.W. Lee, *"Hot-pressed neodymium-iron-boron magnets"*, Appl. Phys. Lett. **46** (1985) 790.

[107] L.V. Azároff, *"Elements of X-Ray Crystallography"*, McGraw-Hill Book Company (1968).

[108] G.K. Williamson and W.H. Hall, *"X-ray line broadening from filed Aluminium and Wolfram"*, Acta Metall. **1** (1953) 22.

[109] V. Neu, *"Austauschgekoppelte nanokristalline Nd-Fe-B-Magnetpulver durch mechanisches Legieren"*, Dissertation, University of Technology, Dresden, Germany (1998).

[110] C. You, X.K. Sun, W. Liu, B. Cui, X. Zhao and Z. Zhang, *"Effect of Co and W additions on the structure and magnetic properties of $Nd_2Fe_{14}B/\alpha$-Fe nanocomposite magnets"*, J. Phys. D: Appl. Phys. **33** (2000) 926.

[111] I.R. Harris, *"The use of hydrogen in the production of Nd-Fe-B –type magnets and in the assessment of Nd-Fe-B –type alloys and permanent magnets – an update"*, Proc. 12th Int. Workshop on RE magnets and their Appl., Canberra, Australia (1992) p. 347.

[112] N.M. Dempsey , P.A.P. Wendhausen, B. Gebel, K.-H. Müller and J.M.D. Coey, *"On the enhancement of the coercivity of HDDR-processed $Sm_2Fe_{17}N_3$"*, Proc. 14th Int. Workshop on RE Magnets and their Appl., Sao Paolo, Brasil (1996) p. 349.

[113] R.N. Faria, A.J. Williams, I.R. Harris, *"High anisotropy in Pr-Fe-Co-B-Zr HDDR powders"*, J. Alloys Comp. **287** (1999) L10.

[114] N.B. Cannesan, D.N. Brown, A.J. Williams and I.R. Harris, *"The production and characterisation of highly anisotropic PrFeCoB-type HDDR powders"*, Proc. 16th Int. Workshop on RE Magnets and their Appl., Sendai (2000) p.757.

[115] O. Gutfleisch, A. Teresiak, B. Gebel, K.-H. Müller, N.B. Cannesan, D.N. Brown and I.R. Harris, *"Metastable borides and the inducement of texture in $Pr_2Fe_{14}B$-type magnets produced by HDDR"*, IEEE Trans. Magn. **37** (2001) 2471.

[116] K.H.J. Buschow, P.C.P. Bouten and A.R. Miedema, *"Hydrides formed from intermetallic compounds of two transition metals: a special class of ternary alloys"*, Rep. Prog. Phys. **45** (1998) p. 958.

[117] O. Gutfleisch, *"Fundamental studies on Hydrogenation Disproportionation Desorption and Recombination (HDDR) processes in Nd-Fe-B-type alloys"*, Dissertation Birmingham, UK (1995).

[118] M. Kubis, O. Gutfleisch, K.-H. Müller, I.R. Harris and L. Schultz, *"Hydrogenation and disproportionation of $Sm_2Fe_{17-x}Ga_x$ at high hydrogen pressures"*, J. Appl. Phys. **83** (1998) 6905.

[119] A. Handstein, M. Kubis, O. Gutfleisch, B. Gebel and K.-H. Müller, *"HDDR of Sm–Co alloys using high hydrogen pressures"*, J. Magn. Magn. Mater. **192** (1999) 73.

[120] S. Sugimoto, O. Gutfleisch and I.R. Harris, *"Resistivity measurements on hydrogenation disproportionation desorption recombination phenomena in Nd-Fe-B alloys with Co, Ga and Zr additions"*, J. Alloys Comp. **260** (1997) 284.

[121] O. Gutfleisch, M. Matzinger, J. Fidler and I.R. Harris, *"Characterisation of solid-HDDR processed $Nd_{16}Fe_{76}B_8$ alloys by means of electron microscopy"*, J. Magn. Magn. Mater. **147** (1995) 320.

[122] D. Book and I. R. Harris, *"Hydrogen absorption/desorption and HDDR studies on $Nd_{16}Fe_{76}B_8$ and $Nd_{11.8}Fe_{82.3}B_{5.9}$"*, J. Alloys Comp. **221** (1995) 187.

[123] T. Takeshita and R. Nakayama, *"Magnetic properties and microstructure of the Nd-Fe-B magnet powder produced by HDD process"*, Proc. 12th Int. Workshop on RE Magnets and their Appl., Canberra (1992) p. 670.

List of publications:

Some parts of this work have been extracted from the different publications listed below. Additional information about several aspects treated along the different chapters can be found there:

1. A. Bollero, O. Gutfleisch, M. Kubis, K.-H. Müller and L. Schultz, *"Hydrogen disproportionation by reactive milling and recombination of $Nd_2(Fe,Co)_{14}B$ alloys"*, Acta Mater. **48** (2000) 4929.

2. O. Gutfleisch, A. Bollero, D. Eckert, B. Gebel, M. Kubis, K.-H. Müller and L. Schultz, *"Exchange coupled Sm_2Co_{17} magnets obtained by reactive milling and recombination"*, Proc. 16th Int. Workshop on RE Magnets and their Appl. (Eds. H. Kaneko, M. Homma and M. Okada), Sendai, Japan (2000) p. 883.

3. A. Bollero, B. Gebel, O. Gutfleisch, K.-H. Müller, L. Schultz, P.J. McGuiness, G. Drazic and S. Kobe, *"NdDyFeBZr high-coercivity powders prepared by intensive milling and the HDDR process"*, J. Alloys Comp. **315** (2001) 243.

4. A. Bollero, A. Kirchner, O. Gutfleisch, K.-H. Müller and L. Schultz, *"Highly coercive milled and melt-spun (Pr,Nd)FeB-type magnets and their hot workability"*, IEEE Trans. Magn. **37** (2001) 2483.

5. P.J. McGuiness, S. Kobe, I. Skulj, A. Bollero, O. Gutfleisch, E.J. Devlin and D. Niarchos, *"Coercivity variations with Pr- and Zr-substituted NdDyFeB-based HDDR powders"*, J. Magn. Magn. Mater. **237** (2001) 267.

6. J.B. Yang, K. Kamaraju, W.B. Yelon, W.J. James, Q. Cai and A. Bollero, *"Magnetic properties of the MnBi intermetallic compound"*, Appl. Phys. Lett. **79** (2001) 1846.

7. A. Yan, A. Bollero, O. Gutfleisch and K.-H. Müller, *"Microstructure and magnetization reversal in nanocomposite $SmCo_5/Sm_2Co_{17}$ magnets"*, J. Appl. Phys. **91** (2002) 2192.

8. O. Gutfleisch, A. Bollero, A. Handstein, D. Hinz, A. Kirchner, A. Yan, K.-H. Müller and L. Schultz, *"Nanocrystalline high performance permanent magnets"*, J. Magn. Magn. Mater. **242-245** (2002) 1277.

9. A. Yan, A. Bollero, K.-H. Müller and O. Gutfleisch, *"Influence of Fe, Zr and Cu on the microstructure and crystallographic texture of melt-spun 2:17 Sm-Co ribbons"*, J. Appl. Phys. **91** (2002) 8825.

10. A. Yan, A. Bollero, O. Gutfleisch and K.-H. Müller, *"Fast development of high coercivity in melt-spun $Sm(CoFe,Cu,Zr)_z$ magnets"*, Appl. Phys. Lett. **80** (2002) 1243.

11. A. Yan, A. Bollero, O. Gutfleisch and K.-H. Müller, *"Microstructure and magnetic properties of two-phase exchange-coupled $SmCo_5/Sm_2(Co,M)_{17}$ (M=Fe, Zr, Cu) nanocomposites"*, J. Phys. D: Appl. Phys. **35** (2002) 835.

12. A. Bollero, O. Gutfleisch, G. Drazic, K.-H. Müller and L. Schultz, *"High-performance nanocrystalline PrFeB-based magnets produced by intensive milling",* J. Appl. Phys. **91** (2002) 8159. *[Awarded at Int. Conf. on Magn. and Magn. Mater. (MMM), Washington, USA (2001)]*.

13. K.-H. Müller, D. Hinz, A. Handstein, A. Bollero, J. Lyubina, D. Eckert, G. Fuchs and O. Gutfleisch, *"Hot deformed nanocrystalline PrFeB magnets for superconducting bearings"*, Proc. 17th Int. Workshop on RE Magnets and their Appl. (Eds. G.C. Hadjipanayis and M.J. Bonder), Delaware, USA (2002) p. 395.

14. A. Bollero, A. Yan, O. Gutfleisch, K.-H. Müller and L. Schultz, *"Intergrain interactions in nanocrystalline isotropic PrFeB-based magnets"*, IEEE Trans. Magn. **39** (2003) 2944.

Acknowledgments

The realisation of this work would not have been possible without the help and the support of many people.

I want to thank Prof. Dr. L. Schultz for giving me the possibility of doing this work at the Institut für Metallische Werkstoffe, his continuous interest in my work and guidance through it.

Dr. K.-H. Müller and Dr. O. Gutfleisch have played a fundamental role in the realisation of this work. I have a very special thanks for both of them for the supervision of my work, their advice along these years and their disposition to help me at any moment.

I want to thank Dr. A. Yan for his advice, his explanations and a very nice work atmosphere.

I am very grateful to K. Pittruff and B. Gebel for expert technical assistance.

Thanks to Dr. M. Kubis for his detailed explanations and suggestions for improvements.

Thanks to Prof. Dr. I.R. Harris for accepting to be referee of my thesis, for stimulating discussions along these years and for making of every visit to Birmingham a nice experience. At this point I want to thank all the people from his group at the School of Metallurgy and Materials in Birmingham.

Thanks to Prof. Dr. C. Laubschat for his advice and for accepting to be referee of my thesis.

Very special thanks are due to Prof. Dr. S. Kobe for her unlimited support, fruitful discussions and for making me feel like at home since my very first visit to the Jozef Stefan Institute in Ljubljana. Thanks to her group for helpful discussions and for all the very special moments; in particular to Dr. P. McGuiness, Dr. G. Drazic, Dr. M. Komelj, T. Zuzek, I. Skulj, A. Porenta and Dr. M. Gec.

Thanks to Prof. Dr. F.H. Sánchez for his invitation to “Facultad de Ciencias Exactas” at Universidad Nacional de La Plata in Argentina. Thanks to Dr. C.E. Rodríguez Torres and Dr. F.D. Saccone for their cooperation and for interesting discussions.

Thanks to P. Crespo and M.J. Borrego for fruitful discussions and advice during their visits to the IFW Dresden.

Thanks are due to my colleagues at the IFW Dresden for stimulating discussions, for their cooperation and for expert technical assistance; in particular I am grateful to Dr. D. Eckert, Dr. A. Kirchner, Dr. D. Hinz, Dr. A. Handstein, Dr. M. Wolf, Dr. P. Verges, Dr. J.B. Yang, Dr. V. Neu, Dr. K. Dörr, Dr. P. Oleinik, P. Bartusch, M. Herrich, J. Lyubina, K. Khlopkov, Dr. M. Sahana, Dr. U. Rößler, Dr. J. Eckert, Dr. A. Gebert, F. Schurack, H. Kempe, L. Fernandez, S. Deledda, Dr. N. Ismail, P. Kerschl, Dr. S. Roth, Dr. M. Richter, Dr. N. Mattern, Dr. A. Güth, Dr. W. Gruner, K. Kersebrock, Dr. J. Acker, Dr. U. Hinz, Dr. R. Schäfer, S. Schinnerling, E. Morawitz and H. Schulze.

Thanks to A. Heinrich for her disposition to help always with a nice smile.

The financial support of the Deutsche Forschungsgemeinschaft (SFB 463), HITEMAG, NATO-Science for Peace and PROALA is also acknowledged.

And finally, very special thanks dedicated to all the persons who have encouraged and helped me in different ways (you know who you are… and I know how lucky I am…).